7/25/68

PROBE COMPENSATED NEAR-FIELD MEASUREMENTS ON A CYLINDER

A THESIS

Presented to

The Faculty of the Division of Graduate

Studies and Research

By

William Marshall Leach, Jr.

In Partial Fulfillment

of the Requirements for the Degree

Doctor of Philosophy

in the School of Electrical Engineering

Georgia Institute of Technology

August, 1972

PROBE COMPENSATED NEAR-FIELD MEASUREMENTS ON A CYLINDER

Approved:

_____

Demetrius T. Paris, Chairman

_____

Ronal W. Larson

_____

Donald G. Bodnar

Date approved by Chairman: __8-18-12__

## ACKNOWLEDGMENTS

I wish to thank my advisor, Dr. Demetrius T. Paris, Professor and Director of the School of Electrical Engineering, for his guidance during the course of this research. Without his guidance in choosing the problem, planning the experimental work, and preparation of the manuscript, this work would never have been possible.

To Dr. Ronal W. Larson and Dr. Donald G. Bodnar go my sincere thanks for their many helpful suggestions concerning the experimental work and preparation of the manuscript. To Dr. Edward B. Joy goes my appreciation for the use of the near-field probes and his measured far-field data on them.

I would like to express my appreciation to Mr. Robert M. Goodman, Chief of the Sensor Systems Division of the Georgia Tech Engineering Experiment Station, for providing me with the use of the measurement facilities of the Experiment Station. Also, I am indebted to Mr. J. Searcy Hollis of Scientific-Atlanta, Inc., for the loan of equipment. Without their aid, the experimental work would have been impossible.

TABLE OF CONTENTS

LIST OF ILLUSTRATIONS

SUMMARY

The prediction of the far-field radiation patterns of antennas from measurements made in the near field has been an area of considerable interest. This research concerns a new method for determining the far-field pattern of an antenna from probe compensated near-field measurements over the surface of a right circular cylinder enclosing the antenna. The method is derived by expanding the radiated fields in cylindrical wave expansions and using the Lorentz reciprocity theorem to solve for the field radiated by the antenna from the probe output voltage. It is shown rigorously that the antenna pattern can be determined independently of the characteristics of the measurement probe provided that certain calibration data for the probe are known. A method for determining these data from the measured far field of the probe is described.

Since the measurement of the near field of any antenna potentially requires the accumulation of a large amount of data, the problem of spatial sampling is of great practical importance. This problem is discussed for the cylindrical measurement surface and lower bounds are established for the axial and polar angle sample intervals on the cylinder. It is specifically assumed that the antenna is not a high-Q or supergain structure.

The theory is verified experimentally by calculating the far-field patterns of a test antenna from measured near-field data. The

near-field measurements on the test antenna are presented for four cases corresponding to different orientations and positions of the antenna inside the measurement cylinder and to different near-field probes. The far-field patterns of the test antenna are calculated for each case and compared to the measured far-field patterns of the antenna.

The computational process required to evaluate the far-field patterns is complex and requires numerical techniques. Specifically, the calculations are centered around an application of the Fast Fourier Transform algorithm to evaluate the necessary integrals and summations. Detailed descriptions of the methods used in the pattern calculations are given, and an example pattern from the literature is computed to verify them.

CHAPTER I

INTRODUCTION

## 1.1  Definition of the Problem

This research concerns the problem of the determination of the far-field pattern of an antenna from measurements made on the near field radiated by the antenna.  A new method is developed to determine the far-field pattern of an antenna from near-field measurements made with a probe over the surface of a right circular cylinder enclosing the antenna.  It is shown that the pattern can be determined independently of the characteristics of the measurement probe.  **Although the choice of the probe is arbitrary, certain a priori information must be known about it in order to compensate for its effect on the measurements.** The required probe information is specified and a method for determining it is described.

An important consideration in the experimental implementation of any near-field measurement scheme is that of spatial sampling.  This problem is discussed for the cylindrical measurement surface.  Sample spacings are developed for antennas which are not high-Q structures.

The method is verified experimentally by calculating far-field patterns of a test antenna from measured near-field data.  The far-field patterns are calculated from near-field data obtained with the test antenna in different orientations inside the measurement cylinder and with different near-field probes.  The calculated far-field patterns are

compared to the experimentally determined far-field patterns of the test antenna.

## 1.2  Origin and History of the Problem

The prediction of the far-field radiation patterns of antennas from measurements made in the near field has been an area of considerable interest (1-11). This is particularly true in the case of microwave antennas for which the distance to the far field exceeds the dimensions of available antenna test ranges. Another case of interest is the determination of far-field patterns from measurements made in the low-noise environment of anechoic chambers. The ability to predict far-field patterns from near-field measurements allows the use of smaller and less expensive anechoic chambers.

Early work in this area involved an application of the aperture field method described by Silver (12). More recent and promising techniques have involved modal expansions of the antenna fields. A technique involving the plane wave spectrum expansion described by Clemmow (13) has been used by Kerns (1) and Joy and Paris (2) to predict the far-field pattern from near-field data measured over the surface of a plane located in front of the antenna. The far field is expressed as a two-dimensional Fourier transform of the field over the measurement plane. A rigorous technique was used to compensate for the effects of the measurement probe.

A similar method has been described by Hamid (3) in which the two-dimensional autocorrelation function of the near field over a plane located in front of the antenna is determined. The far-field power

pattern is then computed as the two-dimensional Fourier transform of this autocorrelation function. No provision was made for compensating for the probe effects.

Although the plane-wave spectrum is invaluable for theoretical work, it does present some problems experimentally. First, the plane over which the field must be measured is of infinite extent. Any actual measurements must be restricted to a finite portion of this plane. Thus there is an uncertainty in any results due to the field over that part of the plane which is not measured. Second, the plane wave expansion is valid for only one hemisphere of space. This is a disadvantage when the radiation pattern is desired in all directions.

Brown and Jull (4) have described and experimentally verified a technique based on a two-dimensional cylindrical wave expansion in which the field is represented as a Fourier series in the polar angle $\phi$. Although this method can be used to obtain a full 360° pattern around the antenna, it is limited to two-dimensional problems for which there is no dependence on the z-coordinate. Thus any practical applications would be restricted to flared beam antennas having broad vertical patterns. In such cases, measurements would be made at a distance such that the vertical pattern is fully developed. A probe compensation scheme was also described and tested for which the plane wave spectrum response of the probe must be known.

Jull (5) has described an additional technique in which the far field is expanded as a series of derivatives of the near field. Again the expansion assumes no variation with the z-coordinate and has the

same restrictions mentioned above. A probe compensation technique was described using the approximate plane wave expansion for a particular probe.

Jensen (6) has described a method for obtaining the far field from the near field measured over a sphere enclosing the antenna. A probe compensation method was also described. However, neither was experimentally tested. Indeed, Jensen (6) implies that the method does not seem to be suitable for practical purposes unless an ideal probe is used.

James and Longdon (7) have described a method for obtaining the far-field spherical wave expansion of an arbitrary antenna from measurements of the radial component of the electric and magnetic fields over a sphere enclosing the antenna. A disadvantage of this method is the rapid rate at which the radial fields decrease with distance from the antenna. In addition, the method requires the use of two measurement probes, one for the electric field and one for the magnetic field. No probe compensation method was described.

The general problem of far-field prediction applies to acoustics as well as electromagnetics. The close connection between the two results from the fact that the sinusoidal steady state acoustic pressure field external to a transducer also satisfies the homogeneous Helmholtz equation (14). This problem has been of particular interest in predicting the far-field radiated noise of submarines (15). Another area has been in the calibration of sonar transducers from measurements made in the near field (16).

A problem of great importance in the measurement of electromagnetic fields is that of sampling. This problem can be broken into two parts: the sampling density problem and probe compensation. It has generally been assumed that sampling distances on the order of a wavelength are sufficient to characterize a field (17). Actually, the spatial rate of change of the fields over any surface is determined by the nature of the sources illuminating that surface and the distance separating the sources from the surface. It is well known that the near field of an antenna can vary rapidly with distance, especially in those cases where the fields are highly reactive. In contrast, the far field does not change appreciably over distances subtending an angle less than the half-power beamwidth.

The required sampling density for any electromagnetic field is also a function of the numerical integration method used to calculate the far field from the sampled near-field data. Brunstein, et al. (18), have compared the sampling densities required to calculate the radiation pattern of a particular aperture with a cylindrically symmetric illumination function using two different numerical integration schemes. Using a technique described by Ludwig (17), the required sampling density was 1.5 points per square wavelength, while a technique described by Rusch (19) required an equivalent 25 points per square wavelength. The Rusch method is actually a one-dimensional integral applied to surfaces possessing cylindrical symmetry. Thus the actual density was 5 points per linear wavelength.

6

In calculating the radiation patterns of multilayered radomes illuminated by a pyramidal horn, Paris (20) found that a sampling density of 2.25 points per square wavelength gave acceptable results. Joy and Paris (2) found that a sampling density of 9 points per square wavelength gave accurate results in the calculation of the far-field of a parabolic reflector from samples taken on a plane located 10 wavelengths in front of the reflector aperture. In this case, Fast Fourier Transform techniques were used to calculate the far field.

Regardless of the sampling density used, the accuracy of any calculated far field depends on the accuracy of the measured samples. Since the ideal probe is not physically realizable, any test antenna used to measure the near field will have an output proportional to a weighted average of the field over its effective aperture. Thus the ability to compensate for the effects of a non-ideal probe is an important consideration in any near-field measurement scheme.

The probe compensation problem has been solved by Kerns (1) when the measurement surface is a plane and the plane wave spectrum response of the probe is known. Joy and Paris (2) have demonstrated excellent agreement between calculated and measured patterns using this scheme. Brown and Jull (4) have solved the probe compensation problem when the probe is used to measure two-dimensional cylindrical fields on a circle containing the source. It was assumed that the probe response could be represented by a two-dimensional plane wave spectrum. Jensen (6) has solved the probe compensation problem when the measurement surface is a sphere enclosing the source. It was assumed that the probe response

could be represented by a spherical wave expansion. The method was not tested experimentally. In fact, the author stated that the method for obtaining an exact solution is unsuitable for practical purposes.

CHAPTER II

THEORETICAL BASIS

## 2.1  Introduction

In this chapter the mathematical background for the problem of
determining the far field of an antenna from probe compensated near-
field measurements on a cylinder containing the antenna is developed.
First, a derivation of the three-dimensional cylindrical wave spectrum
of a radiating field is presented.  It is shown that the cylindrical
wave spectrum of the field radiated by any antenna can be determined
uniquely from a knowledge of the tangential field on a cylinder com-
pletely enclosing the antenna.  The far-field approximation to the
cylindrical wave spectrum is then developed using the method of steepest
descent to evaluate the necessary integrals.

In cases of practical interest, the measurement of the near field
of an antenna must be done with a probe which has non-ideal characteris-
tics.  That is, the output of the probe is not proportional to a single
vector component of the measured field at a point but to a weighted
average of all vector components over some finite area.  The output of
an arbitrary probe, when it is used to measure the field of an arbitrary
antenna, is derived as a function of the cylindrical wave spectrum of
the field radiated by the antenna and the cylindrical wave spectrum of
the field radiated by the probe when it is used as a transmitter.  It
is then shown that the cylindrical wave spectrum of the antenna can be

obtained from the output of the probe when it is used to measure the tangential electric field on the surface of a cylinder enclosing the antenna. The results are then specialized to obtain the far field radiated by the antenna.

In general, the measurement of the near field of an antenna requires a potentially large amount of data. Thus the problem of spatial sampling is one of great practical importance. A spatial sampling criterion for a cylindrical measurement surface containing an antenna is developed. It is assumed that the antenna is not a high-Q or supergain structure.

## 2.2 The Cylindrical Wave Expansion of an Electromagnetic Field

In this section, a derivation of the cylindrical wave spectrum of the field radiated by an antenna is developed. A solution for the magnetic vector potential function is first found for a region of space containing no free-charge density. This solution is next used to obtain the corresponding solutions for the electric and magnetic field intensities. It is then shown that the cylindrical wave spectrum of the field radiated by any antenna can be obtained from a knowledge of the tangential electric (or magnetic) field intensity on the surface of a cylinder containing the antenna.

In any region of space containing no free-charge density, the sinusoidal steady state form of the vector magnetic potential function satisfies the differential equation

$$\nabla^2 \vec{A} + k^2 \vec{A} = 0 \qquad\qquad (2\text{-}1)$$

where $k^2 = \omega^2 \mu\epsilon - j\omega\mu\sigma$. A general solution to this equation can be obtained by using a technique described by Stratton (21) in which $\vec{A}$ is expressed as a linear combination of the three independent vectors

$$\vec{M} = \nabla \times \hat{a}\psi \qquad\qquad (2\text{-}2)$$

$$\vec{N} = \frac{1}{k} \nabla \times \vec{N} \qquad\qquad (2\text{-}3)$$

$$\vec{L} = \nabla\psi \qquad\qquad (2\text{-}4)$$

where $\hat{a}$ is any constant unit vector and $\psi$ is a scalar function which satisfies the differential equation

$$\nabla^2\psi + k^2\psi = 0 \qquad\qquad (2\text{-}5)$$

It follows trivially that $\vec{M}$, $\vec{N}$ and $\vec{L}$ satisfy Equation (2-1) subject to Equation (2-5). In addition, it follows that $\vec{M}$ is related to $\vec{N}$ and $\vec{L}$ by

$$\vec{M} = \vec{L} \times \hat{a} = \frac{1}{k} \nabla \times \vec{N} \qquad\qquad (2\text{-}6)$$

Since $\vec{M}$ and $\vec{N}$ are both defined as the curl of a vector, they are

solenoidal vector fields. Since $\vec{L}$ is defined as the gradient of a scalar, it is a conservative vector field.

In a given coordinate system, solutions for $\vec{M}$, $\vec{N}$ and $\vec{L}$ may be obtained by first solving Equation (2-5) in that system. In the present case, a solution is desired as a function of the cylindrical coordinates $(r,\phi,z)$ illustrated in Figure 1. By the method of separation of variables, it can be shown (22) that a particular solution to Equation (2-5) in cylindrical coordinates is

$$\psi_{nh}^{i}(r,\phi,z) = Z_{n}^{i}(\Lambda r)e^{jn\phi}e^{-jhz}, \qquad i=1,2,3,4 \qquad (2-7)$$

where n is any integer, h is any real number, $\Lambda$ is given by

$$\Lambda = \sqrt{k^2-h^2} \qquad (2-8)$$

and where $Z_{n}^{i}(\Lambda r)$ are the cylindrical Bessel functions

$$Z_{n}^{1}(\Lambda r) = J_{n}(\Lambda r) \qquad (2-9)$$

$$Z_{n}^{2}(\Lambda r) = Y_{n}(\Lambda r) \qquad (2-10)$$

$$Z_{n}^{3}(\Lambda r) = H_{n}^{(1)}(\Lambda r) = J_{n}(\Lambda r) + jY_{n}(\Lambda r) \qquad (2-11)$$

$$Z_{n}^{4}(\Lambda r) = H_{n}^{(2)}(\Lambda r) = J_{n}(\Lambda r) - jY_{n}(\Lambda r) \qquad (2-12)$$
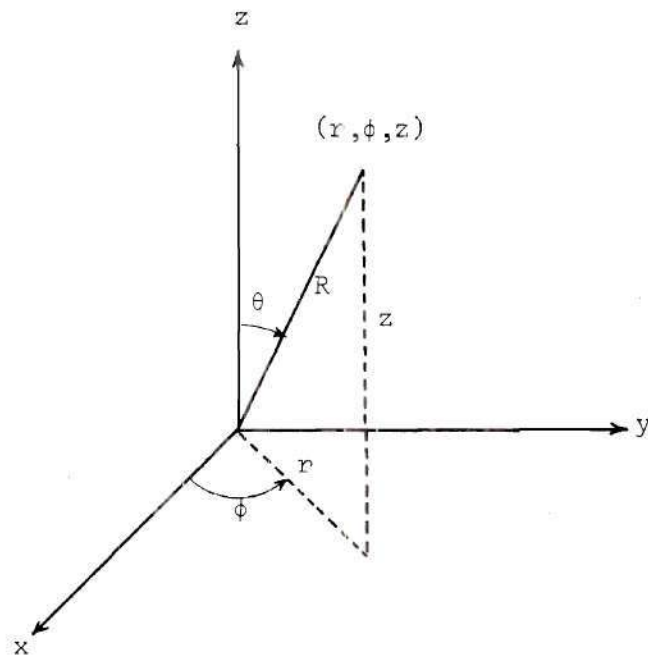
Figure 1. Coordinate System Definitions

In the present case, a solution for $\vec{A}$ is desired which is valid in the region external to a cylinder containing all sources. In order for $\vec{A}$ to satisfy the radiation condition for large r, it follows that the large argument asymptotic expansion of the circular cylinder function must represent surfaces of constant phase which propagate in the positive radial direction. The only one of these four functions which satisfies this condition is the Hankel function of the second kind $H_n^{(2)}(\Lambda r)$. The large argument asymptotic expansion for this function is (23)

$$H_n^{(2)}(\Lambda r) \sim j^{n+\frac{1}{2}} \sqrt{\frac{2}{\pi \Lambda r}} \, e^{-j\Lambda r} \qquad (2\text{-}13)$$

For $\Lambda$ real, it can be seen that this equation represents phase propagation in the positive r direction. With this choice for $Z_n^i(\Lambda r)$, the function $\psi$ becomes

$$\psi_{nh}^4(r,\phi,z) = H_n^{(2)}(\Lambda r) e^{jn\phi} e^{-jhz} \qquad (2\text{-}14)$$

Examination of Equation (2-14) reveals the form of the linear combination of the vectors $\vec{M}$, $\vec{N}$ and $\vec{L}$ for the general solution to Equation (2-1). There are two independent parameters, n and h, over which the linear combination must be formed. Since n is an integer, the combination must be in the form of a sum over all n. Since h is any real number, it follows that the combination must be in the form of an integral over all real h. Thus the general solution for $\vec{A}$ is

$$\vec{A}(r,\phi,z) = \frac{-1}{j\omega} \sum_{n=-\infty}^{\infty} \int_{-\infty}^{\infty} [a_n(h)\vec{M}_{nh}^4(r,\phi,z) + b_n(h)\vec{N}_{nh}^4(r,\phi,z) \qquad (2\text{-}15)$$

$$+ c_n(h)\vec{L}_{nh}^4(r,\phi,z)]dh$$

where $a_n(h)$, $b_n(h)$ and $c_n(h)$ are scalar amplitude weighting functions. The factor $\frac{-1}{j\omega}$ has been chosen to simplify the resulting expression for the electric field intensity $\vec{E}$.

Solutions for the electric and magnetic field intensities can be obtained from the solution for $\vec{A}$ with the familiar relations

$$\vec{H} = \frac{1}{\mu} \nabla \times \vec{A} \qquad (2\text{-}16)$$

$$\vec{E} = \frac{1}{j\omega\epsilon} \nabla \times \vec{H} \qquad (2\text{-}17)$$

where it has been assumed that the conductivity $\sigma$ is zero in the region of interest. With the aid of Equations (2-2) through (2-4) and Equation (2-6), it follows that $\vec{E}$ and $\vec{H}$ are given by

$$\vec{E} = \sum_{n=-\infty}^{\infty} \int_{-\infty}^{\infty} [a_n(h)\vec{M}_{nh}^4 + b_n(h)\vec{N}_{nh}^4]dh \qquad (2\text{-}18)$$

$$\vec{H} = \frac{-k}{j\omega\mu} \sum_{n=-\infty}^{\infty} \int_{-\infty}^{\infty} [a_n(h)\vec{N}_{nh}^4 + b_n(h)\vec{M}_{nh}^4]dh \qquad (2\text{-}19)$$

The absence of the vector $\vec{L}$ in the solutions for $\vec{E}$ and $\vec{H}$ also follows from the fact that $\vec{L}$ has non-zero divergence. Thus it cannot be used to represent $\vec{E}$ or $\vec{H}$ in a source-free region since $\nabla \cdot \vec{E} = \nabla \cdot \vec{H} = 0$.

Although the constant unit vector $\hat{a}$ in Equation (2-2) may be chosen arbitrarily, it is convenient to choose it so that $\vec{M}$ has no z-component. If Equation (2-2) is rewritten in the form

$$\vec{M} = \nabla\psi \times \hat{a} \tag{2-20}$$

it can be seen that the choice $\hat{a} = \hat{z}$ makes this true. It follows from Equations (2-2) and (2-3) that the solutions for $\vec{M}$ and $\vec{N}$ can be written

$$\vec{M}_{nh}^i = \vec{m}_{nh}^i e^{jn\phi} e^{-jhz} \tag{2-21}$$

$$\vec{N}_{nh}^i = \vec{n}_{nh}^i e^{jn\phi} e^{-jhz} \tag{2-22}$$

where

$$\vec{m}_{nh}^i = \hat{r}\,\frac{jn}{r}\,Z_n^i(\Lambda r) - \hat{\phi}\,\frac{\partial Z_n^i}{\partial r} \tag{2-23}$$

$$\vec{n}_{nh}^i = -\hat{r}\,\frac{jh}{k}\,\frac{\partial Z_n^i}{\partial r} + \hat{\phi}\,\frac{nh}{kr}\,Z_n^i(\Lambda r) + \hat{z}\,\frac{\Lambda^2}{k}\,Z_n^i(\Lambda r) \tag{2-24}$$

With the introduction of Equations (2-21) and (2-22) into Equation (2-18), it follows that the electric field intensity can be written

$$\vec{E} = \sum_{n=-\infty}^{\infty} e^{jn\phi} \int_{-\infty}^{\infty} [a_n(h)\vec{m}_{nh}^4 + b_n(h)\vec{n}_{nh}^4]e^{-jhz}\,dh \tag{2-25}$$

where $\vec{m}_{nh}^4$ represents a solution which is transverse electric to the z-direction or $(TE)_z$ and $\vec{n}_{nh}^4$ represents one which is transverse magnetic to the z-direction or $(TM)_z$. On any cylinder on which r is constant, each scalar component of this equation is in the form of a Fourier series in $\phi$ and a Fourier integral in z. Thus it follows that the inverse relationship

$$a_n(h)\vec{m}_{nh}^4 + b_n(h)\vec{n}_{nh}^4 = \frac{1}{4\pi^2} \int_{-\infty}^{\infty} \int_{-\pi}^{\pi} \vec{E}(r_1,\phi,z)e^{-jn\phi}e^{jhz}d\phi dz \qquad (2\text{-}26)$$

must exist, where $r_1$ is the radius of the cylinder.

It follows that Equation (2-26) can be solved for $a_n(h)$ and $b_n(h)$ if it is separated into its scalar components and the resulting equations solved simultaneously. However, only two components of $\vec{E}$ need be known since there are only two quantities to be determined. If the two components are chosen to be $E_\phi$ and $E_z$ on the cylinder, the resulting equations are

$$a_n(h)\left[- \frac{\partial H_n^{(2)}}{\partial r}\right] + b_n(h)\left[\frac{nh}{kr} H_n^{(2)}(\Lambda r)\right] = I_\phi \qquad (2\text{-}27)$$

$$b_n(h)\left[\frac{\Lambda^2}{k} H_n^{(2)}(\Lambda r)\right] = I_z \qquad (2\text{-}28)$$

where

$$I_\phi = \frac{1}{4\pi^2} \int_{-\infty}^{\infty} \int_{-\pi}^{\pi} E_\phi(r_1,\phi,z)e^{-jn\phi}e^{jhz}d\phi dz \qquad (2\text{-}29)$$

$$I_z = \frac{1}{4\pi^2} \int_{-\infty}^{\infty} \int_{-\pi}^{\pi} E_z(r_1,\phi,z)e^{-jn\phi}e^{jhz}d\phi dz \qquad (2\text{-}30)$$

These equations can be solved simultaneously to yield

$$a_n(h) = \frac{-I_\phi}{\dfrac{\partial}{\partial r_1}\left[H_n^{(2)}(\Lambda r_1)\right]} + \frac{nhI_z}{\Lambda^2 r_1 \dfrac{\partial}{\partial r_1}\left[H_n^{(2)}(\Lambda r_1)\right]} \qquad (2\text{-}31)$$

$$b_n(h) = \frac{I_z}{\dfrac{\Lambda^2}{k} H_n^{(2)}(\Lambda r_1)} \qquad (2\text{-}32)$$

Thus it follows that a knowledge of the tangential electric field intensity on the surface of a cylinder containing all sources is sufficient to determine the fields at all points external to the cylinder. A solution involving the tangential magnetic field on the cylinder follows similarly.

In order to use Equations (2-31) and (2-32), the tangential field on the cylinder must be either known a priori or measured with an ideal probe. A new method for determining the functions $a_n(h)$ and $b_n(h)$ from measurements on the cylinder with an arbitrary probe is developed in Section 2.4. The method assumes only that the cylindrical wave expansion of the field radiated by the probe, when it is used as a transmitter, is known.

## 2.3   The Far-Field Approximation to
## the Cylindrical Wave Expansion

In the previous section, a general expression for the electric field intensity external to a closed surface containing all sources was developed.  In general, the evaluation of this expression is a formidable task.  However, a considerable simplification results if the field is to be evaluated in the far-field region of the source.  In this section, the far-field approximation to the cylindrical wave expansion given by Equation (2-25) is developed.  First, the Hankel functions which appear in the cylindrical wave vectors $\vec{m}_{nh}^{4}$ and $\vec{n}_{nh}^{4}$ are replaced by their large argument asymptotic expansions.  The integral in Equation (2-25) is  then be evaluated using the method of steepest descent.  The far field is then shown to be a spherical transverse electromagnetic field.

For large r, the cylindrical wave vectors $\vec{m}_{nh}^{4}$ and $\vec{n}_{nh}^{4}$ which are defined in Equations (2-23) and (2-24), can be simplified considerably if the Hankel function $H_n^{(2)}(\Lambda r)$ and its partial derivative with respect to r are replaced by their large argument asymptotic expansions.  The large argument asymptotic expansion for $H_n^{(2)}(\Lambda r)$ has been given in Equation (2-13).  The corresponding expansion for $\frac{\partial H_n^{(2)}}{\partial r}$ can be obtained by taking the partial derivative of this equation with respect to r to yield

$$\frac{\partial H_n^{(2)}}{\partial r} \sim j^{n-\frac{1}{2}} \sqrt{\frac{2\Lambda}{\pi r}} \; e^{-j\Lambda r} \qquad (2\text{-}33)$$

where the term involving $r^{-3/2}$ has been neglected for large $r$. The resulting expressions for the cylindrical wave vectors $\vec{m}^4_{nh}$ and $\vec{n}^4_{nh}$ are

$$\vec{m}^4_{nh} = -\hat{\phi} j^{n-\frac{1}{2}} \sqrt{\frac{2\Lambda}{\pi r}} e^{-j\Lambda r} \tag{2-34}$$

$$\vec{n}^4_{nh} = -(\hat{r}h-\hat{z}\Lambda) \frac{j^{n+\frac{1}{2}}}{k} \sqrt{\frac{2\Lambda}{\pi r}} e^{-j\Lambda r} \tag{2-35}$$

Substitution of these expressions into the equation for the general solution for $\vec{E}$ yields

$$\vec{E} = j^{\frac{1}{2}} \sqrt{\frac{2}{\pi r}} \sum_{n=-\infty}^{\infty} j^n e^{jn\phi} \int_{-\infty}^{\infty} \Lambda^{\frac{1}{2}} [\hat{\phi} j a_n(h) \tag{2-36}$$

$$- \frac{1}{k} (\hat{r}h-\hat{z}\Lambda) b_n(h)] e^{-j\Lambda r} e^{-jhz} dh$$

where $\Lambda = \sqrt{k^2-h^2}$. This equation can be simplified by making the change in variables

$$h = k\sin\alpha \tag{2-37}$$

and by converting the far-field point to spherical coordinates with the transformations

$$r = R\sin\theta \tag{2-38}$$

$$z = R\cos\theta \tag{2-39}$$

The result is

$$\vec{E} = j^{1/2}k^{3/2} \sqrt{\frac{2}{\pi R \sin\theta}} \sum_{n=-\infty}^{\infty} j^n e^{jn\phi} \int_C [\hat{\phi} j a_n(k\sin\alpha) \tag{2-40}$$

$$- (\hat{r}\sin\alpha - \hat{z}\cos\alpha)b_n(k\sin\alpha)]\cos^{3/2}\alpha \; e^{-jkR\sin(\alpha+\theta)}d\alpha$$

where C is the contour illustrated in Figure 2.

The integral in the above expression is evaluated in Appendix A using the method of steepest descent. The resulting expression for the electric field intensity is shown to be

$$\vec{E} = \frac{-2k\sin\theta}{R} e^{-jkR} \sum_{n=-\infty}^{\infty} j^n e^{jn\phi}[\hat{\phi}a_n(k\cos\theta) \tag{2-41}$$

$$- j(\hat{r}\cos\theta - \hat{z}\sin\theta)b_n(k\cos\theta)]$$

Since $\hat{\theta} = \hat{r}\cos\theta - \hat{z}\sin\theta$, this equation can be separated into the spherical components

$$E_R = 0 \tag{2-42}$$

$$E_\theta = \frac{-j2\sin\theta}{R} e^{-jkR} \sum_{n=-\infty}^{\infty} j^n b_n(k\cos\theta)e^{jn\phi} \tag{2-43}$$

$$E_\phi = \frac{-2\sin\theta}{R} e^{-jkR} \sum_{n=-\infty}^{\infty} j^n a_n(k\cos\theta)e^{jn\phi} \tag{2-44}$$

Thus the far-field electric field intensity is transverse to the radial direction, as would be expected.
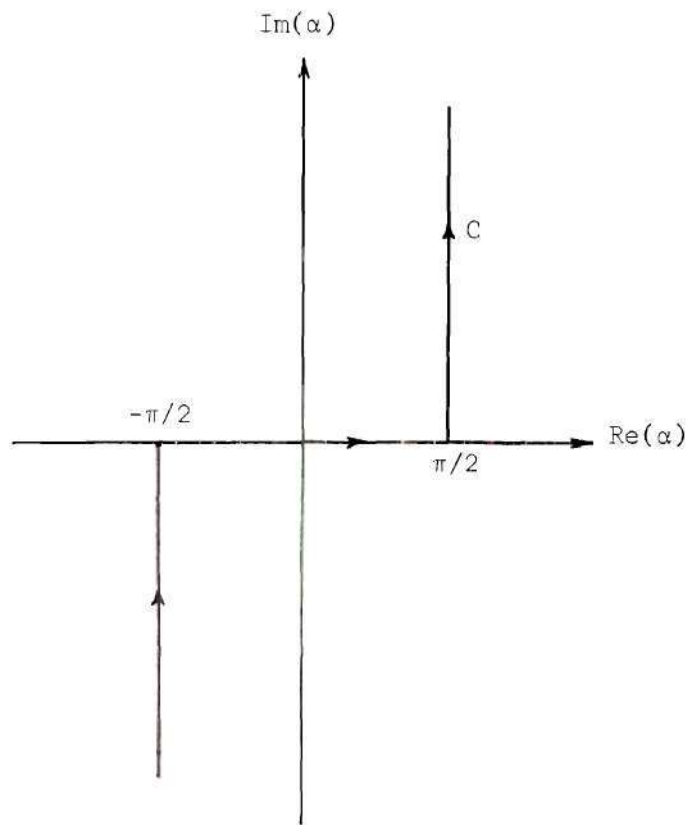
Figure 2.  The Contour of Integration C

Comparison of Equations (2-18) and (2-19) reveals that the far-field magnetic field intensity can be obtained from the solution for the electric field intensity by simply interchanging the amplitude weighting functions $a_n(h)$ and $b_n(h)$ and by including the multiplicative factor $-k/j\omega\mu$. The resulting expressions are

$$H_R = 0 \qquad\qquad (2\text{-}45)$$

$$H_\theta = -\frac{E_\phi}{\eta} \qquad\qquad (2\text{-}46)$$

$$H_\phi = \frac{E_\theta}{\eta} \qquad\qquad (2\text{-}47)$$

where $\eta = \sqrt{\mu/\epsilon}$. Thus the far-field magnetic field intensity is also transverse to the radial direction and is related to the solution for $\vec{E}$ by the vector equation

$$\vec{H} = \frac{\hat{R} \times \vec{E}}{\eta} \qquad\qquad (2\text{-}48)$$

Since both $\vec{E}$ and $\vec{H}$ have no radial components and are mutually perpendicular, the far field comprises a spherical transverse electromagnetic field.

Examination of the foregoing solutions shows that the far field is determined only by those values of $a_n(h)$ and $b_n(h)$ for which $-k \leq h \leq k$ since $|k\cos\theta| \leq k$. Thus it can be concluded that the part of the near field for which $|h| > k$ represents evanescent waves in the

vicinity of the antenna. These waves represent reactive energy storage which in no way influences the far-field structure except to the extent that they are necessary to support a particular current distribution on the antenna. In Section 2.5 a spatial sampling criterion is developed for the near field on the surface of a cylinder enclosing the antenna. In that section, it will be assumed that the reactive energy stored outside the cylinder is negligible. This assumption will be shown to be true for any antenna which is not a high-Q or supergain structure.

### 2.4 The Determination of the Far Field of an Antenna from Probe Compensated Near-Field Measurements on a Cylinder Containing the Antenna

In this section a new method will be developed to obtain the far field of an antenna from probe compensated near-field measurements over the surface of a cylinder containing the antenna. It will be shown that the far field of the antenna can be calculated independently of the receiving properties of the probe. The only information which will be assumed about the probe is a knowledge of the cylindrical wave expansion of its radiated field, when used as a radiator. It will then be shown that the required information can be obtained knowing only the far field radiated by the probe over a sphere containing it.

In Figure 3, let the surface $\Sigma_a$ be a cylinder of radius $r_a$ that contains an arbitrary test antenna connected to signal generator A. It has been shown that in the region $r \geq r_a$ the field radiated by this antenna can be expressed as
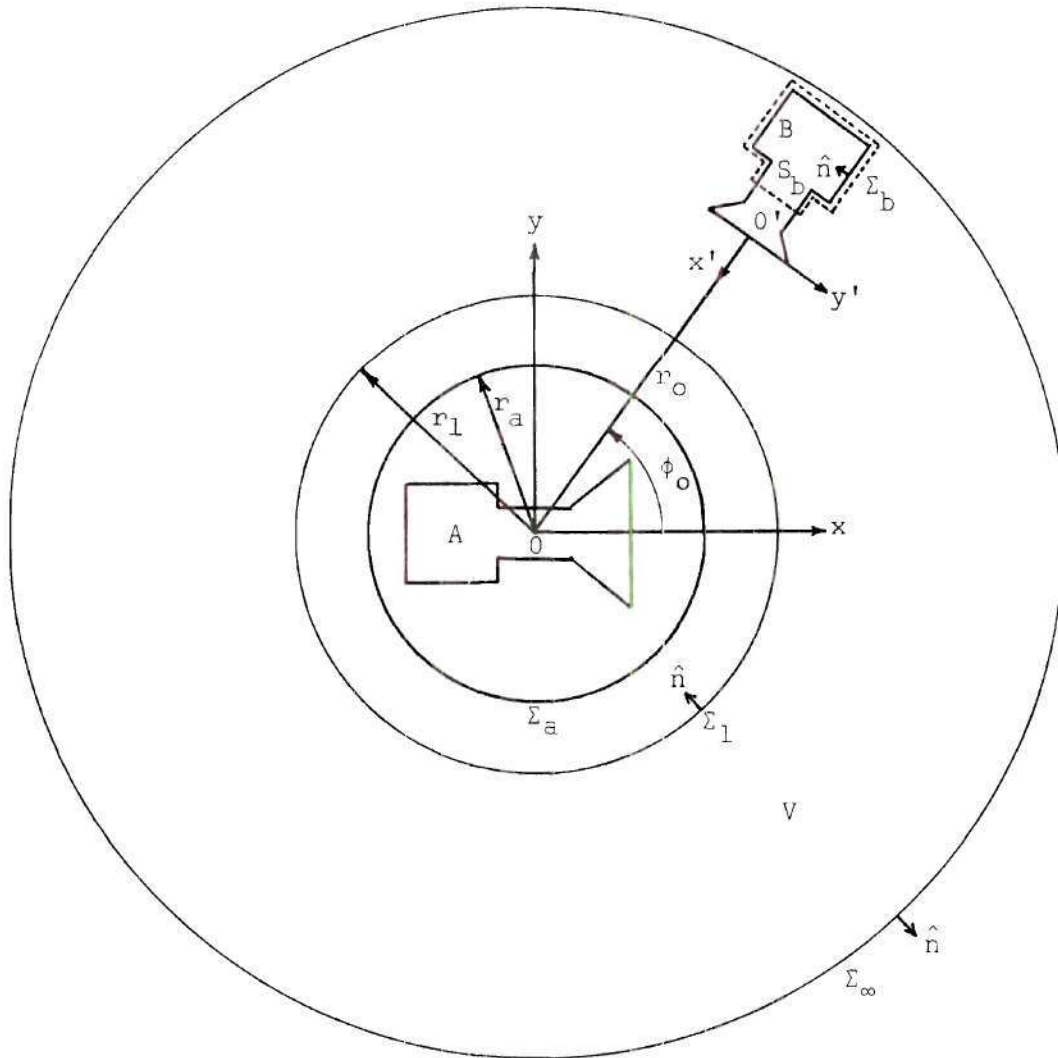
Figure 3.   Geometry for the Probe Compensation Derivation

$$\vec{E}_a(r,\phi,z) = \sum_{n=-\infty}^{\infty} \int_{-\infty}^{\infty} [a_n(h)\vec{M}_{nh}^4(r,\phi,z) \qquad (2\text{-}49)$$

$$+ \, b_n(h)\vec{N}_{nh}^4(r,\phi,z)]dh$$

$$\vec{H}_a(r,\phi,z) = \frac{-k}{j\omega\mu} \sum_{n=-\infty}^{\infty} \int_{-\infty}^{\infty} [b_n(h)\vec{M}_{nh}^4(r,\phi,z) \qquad (2\text{-}50)$$

$$+ \, a_n(h)\vec{N}_{nh}^4(r,\phi,z)]dh$$

Let this field be incident on a probe antenna whose reference origin 0'
is located at the point $(r_o,\phi_o,z_o)$, as shown in Figure 3. Let the probe
be connected via a waveguide feeder to signal generator B. The field
radiated by the probe when generator B is activated can be expressed as

$$\vec{E}_b(r',\phi',z') = \sum_{m=-\infty}^{\infty} \int_{-\infty}^{\infty} [c_m(\eta)\vec{M}_{m\eta}^4(r',\phi',z') \qquad (2\text{-}51)$$

$$+ \, d_m(\eta)\vec{N}_{m\eta}^4(r',\phi',z')]d\eta$$

$$\vec{H}_b(r',\phi',z') = \frac{-k}{j\omega\mu} \sum_{m=-\infty}^{\infty} \int_{-\infty}^{\infty} [d_m(\eta)\vec{M}_{m\eta}^4(r',\phi',z') \qquad (2\text{-}52)$$

$$+ \, c_m(\eta)\vec{N}_{m\eta}^4(r',\phi',z')]d\eta$$

where $(r',\phi',z')$ are measured with respect to 0'.

Denote the field scattered by the test antenna when generator B
is activated by $\vec{E}_{as}$ and $\vec{H}_{as}$. These can be written in the form

$$\vec{E}_{as}(r,\phi,z) = \sum_{m=-\infty}^{\infty} \int_{-\infty}^{\infty} [a_{ms}(\eta)\vec{M}_{m\eta}^4(r,\phi,z) \tag{2-53}$$

$$+ b_{ms}(\eta)\vec{N}_{m\eta}^4(r,\phi,z)]d\eta$$

$$\vec{H}_{as}(r,\phi,z) = \frac{-k}{j\omega\mu} \sum_{m=-\infty}^{\infty} \int_{-\infty}^{\infty} [b_{ms}(\eta)\vec{M}_{m\eta}^4(r,\phi,z) \tag{2-54}$$

$$+ a_{ms}(\eta)\vec{N}_{m\eta}^4(r,\phi,z)]d\eta$$

Similarly, the field scattered by the probe when generator A is activated can be written

$$\vec{E}_{bs}(r',\phi',z') = \sum_{n=-\infty}^{\infty} \int_{-\infty}^{\infty} [c_{ns}(h)\vec{M}_{nh}^4(r',\phi',z') \tag{2-55}$$

$$+ d_{ns}(h)\vec{N}_{nh}^4(r',\phi',z')]dh$$

$$\vec{H}_{bs}(r',\phi',z') = \frac{-k}{j\omega\mu} \sum_{n=-\infty}^{\infty} \int_{-\infty}^{\infty} [d_{ns}(h)\vec{M}_{nh}^4(r',\phi',z') \tag{2-56}$$

$$+ c_{ns}(h)\vec{N}_{nh}^4(r',\phi',z')]dh$$

In the following analysis, it will be assumed that there are no multiply scattered fields between the antenna and the probe so that the total scattered field is given by Equations (2-53) through (2-56).

It is desired to solve for the voltage induced across the terminals of generator B when only generator A is activated. After

solving for this voltage, it will be shown that the far field of the test antenna can be calculated from this voltage when its amplitude and phase are known as functions of $\phi_o$ and $z_o$ over the cylinder of radius $r_o$. It will be assumed that the cylindrical wave expansion of the field radiated by the probe when generator B is activated is known. A numerical method is developed in Section 3.3 for obtaining this information from the measured far field of the probe antenna. Also, without loss of generality, it will be assumed that generator B is matched to the waveguide feeder for the probe antenna.

In Figure 3 let V be the volume bounded by the surfaces $\Sigma_1$, $\Sigma_b$, and $\Sigma_\infty$, where $\Sigma_1$ is the cylinder of radius $r_1$, $\Sigma_b$ is the surface lying just outside the shield enclosing generator B and cutting the waveguide feeder for the probe at $S_b$, and $\Sigma_\infty$ is the sphere of infinite radius. Since there are no source currents in V by assumption, it follows from the Lorentz reciprocity theorem (24) that

$$\oint_{\Sigma_1+\Sigma_2+\Sigma_\infty} [(\vec{E}_a+\vec{E}_{bs})\times(\vec{H}_b+\vec{H}_{as}) - (\vec{E}_b+\vec{E}_{as})\times(\vec{H}_a+\vec{H}_{bs})]\cdot\hat{n}\,da = 0 \qquad (2\text{-}57)$$

where all multiply scattered terms have been neglected. The Lorentz theorem is the basis for all calculations of the output of a receiving antenna in the presence of a transmitting antenna (12). The integrand of this expression vanishes identically over the shield enclosing generator B and over $\Sigma_\infty$ (24). Also, $\vec{E}_{bs} = 0$ and $\vec{H}_{bs} = 0$ over $S_b$ by virtue of their definition. Thus Equation (2-57) yields

$$\oint_{\Sigma_1} (\vec{E}_a \times \vec{H}_b - \vec{E}_b \times \vec{H}_a) \cdot (-\hat{r}) da + \oint_{\Sigma_1} (\vec{E}_a \times \vec{H}_{as} - \vec{E}_{as} \times \vec{H}_a) \cdot (-\hat{r}) da \qquad (2\text{-}58)$$

$$+ \oint_{\Sigma_1} (\vec{E}_{bs} \times \vec{H}_b - \vec{E}_b \times \vec{H}_{bs}) \cdot (-\hat{r}) da + \oint_{\Sigma_1} (\vec{E}_{bs} \times \vec{H}_{as} - \vec{E}_{as} \times \vec{H}_{bs}) \cdot (-\hat{r}) da$$

$$+ \int_{S_b} [\vec{E}_a \times (\vec{H}_b + \vec{H}_{as}) - (\vec{E}_b + \vec{E}_{as}) \times \vec{H}_a] \cdot (-\hat{x}') da = 0$$

The integrand of the fourth integral in this expression involves products of the scattered fields. If it is assumed that the scattered fields are small compared to the incident fields, this term can be neglected. In the integral over $S_b$, it will be assumed that the contribution of the scattered terms $\vec{E}_{as}$ and $\vec{H}_{as}$ is negligible, so that in this integral $\vec{E}_b + \vec{E}_{as} \cong \vec{E}_b$ and $\vec{H}_b + \vec{H}_{as} \cong \vec{H}_b$. With these assumptions, Equation (2-58) reduces to

$$\oint_{\Sigma_1} (\vec{E}_a \times \vec{H}_b - \vec{E}_b \times \vec{H}_a) \cdot (-\hat{r}) da + \oint_{\Sigma_1} (\vec{E}_a \times \vec{H}_{as} - \vec{E}_{as} \times \vec{H}_a) \cdot (-\hat{r}) da \qquad (2\text{-}59)$$

$$+ \oint_{\Sigma_1} (\vec{E}_{bs} \times \vec{H}_b - \vec{E}_b \times \vec{H}_{bs}) \cdot (-\hat{r}) da + \int_{S_b} (\vec{E}_a \times \vec{H}_b - \vec{E}_b \times \vec{H}_a) \cdot (-\hat{x}') da$$

$$= 0$$

Let the four integrals in the above expression be denoted by $I_1$, $I_2$, $I_3$, and $I_4$, respectively. To evaluate $I_1$, it will be assumed initially that the fields are of the form

$$\vec{E}_a(r,\phi,z) = a_n(h) \vec{M}_{nh}^4(r,\phi,z) + b_n(h) \vec{N}_{nh}^4(r,\phi,z) \qquad (2\text{-}60)$$

$$\vec{H}_a(r,\phi,z) = \frac{-k}{j\omega\mu} [b_n(h)\vec{M}^4_{nh}(r,\phi,z) + a_n(h)\vec{N}^4_{nh}(r,\phi,z)] \qquad (2\text{-}61)$$

$$\vec{E}_b(r',\phi',z') = c_m(\eta)\vec{M}^4_{m\eta}(r',\phi',z') + d_m(\eta)\vec{N}^4_{m\eta}(r',\phi',z') \qquad (2\text{-}62)$$

$$\vec{H}_b(r',\phi',z') = \frac{-k}{j\omega\mu} [d_m(\eta)\vec{M}^4_{m\eta}(r',\phi',z') \qquad (2\text{-}63)$$

$$+ c_m(\eta)\vec{N}^4_{m\eta}(r',\phi',z')]$$

After $I_1$ is evaluated for these fields, the result must be summed in m and n and integrated in $\eta$ and h to obtain the final value of the integral.

With the vector translation theorems developed in Appendix B, the origin for $\vec{E}_b$ and $\vec{H}_b$ is first changed from 0' to 0. The result is

$$\vec{E}_b(r,\phi,z) = \sum_{\ell=-\infty}^{\infty} (-1)^\ell H^{(2)}_{m+\ell}(\lambda r_o)e^{j\ell\phi_o} e^{jnz_o} \qquad (2\text{-}64)$$

$$\times [c_m(\eta)\vec{M}^1_{-\ell\eta}(r,\phi,z) + d_m(\eta)\vec{N}^1_{-\ell\eta}(r,\phi,z)]$$

$$\vec{H}_b(r,\phi,z) = \frac{-k}{j\omega\mu} \sum_{\ell=-\infty}^{\infty} (-1)^\ell H^{(2)}_{m+\ell}(\lambda r_o)e^{j\ell\phi_o} e^{jnz_o} \qquad (2\text{-}65)$$

$$\times [d_m(\eta)\vec{M}^1_{-\ell\eta}(r,\phi,z) + c_m(\eta)\vec{N}^1_{-\ell\eta}(r,\phi,z)]$$

where $\lambda = \sqrt{k^2-\eta^2}$ . With the substitution of these expressions and the ones for $\vec{E}_a$ and $\vec{H}_a$ into the integrand for $I_1$, this integral becomes

$$I_1 = \frac{k}{j\omega\mu} \sum_{\ell=-\infty}^{\infty} (-1)^{\ell} H_{m+\ell}^{(2)}(\lambda r_o) e^{j\ell\phi_o} e^{j\eta z_o} \int_{-\infty}^{\infty} \int_{-\pi}^{\pi} \left[ \left( a_n(h)d_m(\eta) \right. \right. \tag{2-66}$$

$$+ \left. b_n(h)c_m(\eta) \right) \left( \vec{M}_{nh}^4(r,\phi,z) \times \vec{M}_{-\ell\eta}^1(r,\phi,z) + \vec{N}_{nh}^4(r,\phi,z) \times \vec{N}_{-\ell\eta}^1(r,\phi,z) \right)$$

$$+ \left( a_n(h)c_m(\eta) + b_n(h)d_m(\eta) \right) \left( \vec{M}_{nh}^4(r,\phi,z) \times \vec{N}_{-\ell\eta}^1(r,\phi,z) \right.$$

$$+ \left. \left. \vec{N}_{nh}^4(r,\phi,z) \times \vec{M}_{-\ell\eta}^1(r,\phi,z) \right) \right] \cdot \hat{r} r_1 \, d\phi \, dz$$

From the orthogonality properties of the cylindrical wave vectors developed in Appendix C, it follows that the terms involving the products $\vec{M}_{nh}^4 \times \vec{N}_{-\ell h}^1 \cdot \hat{r}$ and $\vec{N}_{nh}^4 \times \vec{M}_{-\ell h}^1 \cdot \hat{r}$ have zero contribution to the above integral. The remaining terms can be evaluated with the aid of Equations (C-3) and (C-4). The result is

$$I_1 = \frac{-k}{j\omega\mu} \sum_{\ell=-\infty}^{\infty} (-1)^{\ell} H_{m+\ell}^{(2)}(\lambda r_o) e^{j\ell\phi_o} e^{j\eta z_o} \left( a_n(h)c_m(\eta) \right. \tag{2-67}$$

$$+ \left. b_n(h)d_m(\eta) \right) \left\{ \frac{4\pi^2\Lambda^3}{k} \delta_{n\ell} \, \delta(\eta+h) \, \left[ -J_{-n}'(\Lambda r_1) H_n^{(2)}(\Lambda r_1) \right. \right.$$

$$+ \left. \left. J_{-n}(\Lambda r_1) H_n^{(2)'}(\Lambda r_1) \right] \right\}$$

The term in the brackets can be simplified with the aid of the identity

$$J_{-n}'(\Lambda r_1) H_n^{(2)}(\Lambda r_1) - J_{-n}(\Lambda r_1) H_n^{(2)'}(\Lambda r_1) = \frac{(-1)^n j 2\Lambda^2}{\pi k r_1} \tag{2-68}$$

Thus $I_1$ reduces to

$$I_1 = \frac{8\pi\Lambda^2}{\omega\mu} H_{n+m}^{(2)}(\Lambda r_o) e^{jn\phi_o} e^{j\eta z_o} \delta(\eta+h)\left(a_n(h)c_m(\eta)+b_n(h)d_m(\eta)\right) \quad (2\text{-}69)$$

which is independent of $r_1$. When this expression is summed over all $m$ and $n$ and integrated over all $h$ and $\eta$, the result is

$$I_1 = \frac{8\pi\Lambda^2}{\omega\mu} \sum_{n=-\infty}^{\infty} e^{jn\phi_o} \int_{-\infty}^{\infty} \left[a_n(h) \sum_{m=-\infty}^{\infty} c_m(-h)H_{n+m}^{(2)}(\Lambda r_o) \right. \quad (2\text{-}70)$$

$$\left. + b_n(h) \sum_{m=-\infty}^{\infty} d_m(-h)H_{n+m}^{(2)}(\Lambda r_o)\right] e^{-jhz_o} dh$$

where the sampling property of the impulse function $\delta(\eta+h)$ has been used to eliminate the integral in $\eta$.

The integrals $I_2$ and $I_3$ in Equation (2-59) can be shown to vanish identically. First, that $I_2 \equiv 0$ can be shown as follows: substitution of the cylindrical wave expansions for $\vec{E}_a$, $\vec{H}_a$, $\vec{E}_{as}$, and $\vec{H}_{as}$ results in the expression

$$I_2 = \frac{k}{j\omega\mu} \int_{-\infty}^{\infty} \int_{-\pi}^{\pi} \left[\left(a_n(h)b_{ms}(\eta)+a_{ms}(\eta)b_n(h)\right) \right. \quad (2\text{-}71)$$

$$\times \left(\vec{M}_{nh}^4(r,\phi,z)\times\vec{M}_{m\eta}^4(r,\phi,z) + \vec{N}_{nh}^4(r,\phi,z)\times\vec{N}_{m\eta}^4(r,\phi,z)\right)$$

$$+ \left(a_n(h)a_{ms}(\eta)+b_n(h)b_{ms}(\eta)\right)\left(\vec{M}_{nh}^4(r,\phi,z)\times\vec{N}_{m\eta}^4(r,\phi,z)\right.$$

$$\left.\left. + \vec{N}_{nh}^4(r,\phi,z)\times\vec{M}_{m\eta}^4(r,\phi,z)\right)\right]\cdot\hat{r}r_1 d\phi dz$$

where the final result is to be summed over m and n and integrated in $\eta$ and h. From the vector orthogonality properties developed in Appendix C, it follows as in the expression for $I_1$ that the terms involving the products $\vec{M}^4_{nh} \times \vec{M}^4_{m\eta} \cdot \hat{r}$ and $\vec{N}^4_{nh} \times \vec{N}^4_{m\eta} \cdot \hat{r}$ have zero contribution to $I_2$. Examination of Equations (C-3) and (C-4) shows that the contribution of the term $\vec{M}^4_{nh} \times \vec{N}^4_{m\eta} \cdot \hat{r}$ is exactly cancelled by that of the term $\vec{N}^4_{nh} \times \vec{M}^4_{m\eta} \cdot \hat{r}$. Thus it follows that $I_2$ is identically zero.

To show that $I_3$ is zero, the origin for the vector functions appearing in its integrand is first changed from 0' to 0 with the aid of the vector translation theorems developed in Appendix B. The resulting expressions for $\vec{E}_b$ and $\vec{H}_b$ have been given in Equations (2-64) and (2-65). Those for $\vec{E}_{bs}$ and $\vec{H}_{bs}$ are

$$\vec{E}_{bs}(r,\phi,z) = \sum_{i=-\infty}^{\infty} H^{(2)}_{n+i}(\Lambda r_o) e^{ji\phi_o} e^{jhz_o} \left[ c_{ns}(h)\vec{M}^1_{-ih}(r,\phi,z) \right. \tag{2-72}$$

$$\left. + d_{ns}(h)\vec{N}^1_{-ih}(r,\phi,z) \right]$$

$$\vec{H}_{bs}(r,\phi,z) = \frac{-k}{j\omega\mu} \sum_{i=-\infty}^{\infty} H^{(2)}_{n+i}(\Lambda r_o) e^{ji\phi_o} e^{jhz_o} \tag{2-73}$$

$$\times \left[ d_{ns}(h)\vec{M}^1_{-ih}(r,\phi,z) + c_{ns}(h)\vec{N}^1_{-ih}(r,\phi,z) \right]$$

When these expressions and those for $\vec{E}_b$ and $\vec{H}_b$ are substituted into the integrand of $I_3$, the result is

$$I_3 = \frac{k}{j\omega\mu} \sum_{i=-\infty}^{\infty} \sum_{\ell=-\infty}^{\infty} (-1)^{i+\ell} H_{m+i}^{(2)}(\Lambda r_o) H_{n+\ell}^{(2)}(\Lambda r_o) e^{j(i+\ell)\phi_o} e^{j(h+\eta)z_o} \qquad (2\text{-}74)$$

$$\times \int_{-\infty}^{\infty} \int_{-\pi}^{\pi} \left[ \left( c_m(\eta) d_{ns}(h) + d_m(\eta) c_{ns}(h) \right) \left( \vec{M}_{-i\eta}^1(r,\phi,z) \times \vec{M}_{-\ell h}^1(r,\phi,z) \right. \right.$$

$$\left. + \vec{N}_{-i\eta}^1(r,\phi,z) \times \vec{N}_{-\ell h}^1(r,\phi,z) \right) + \left( c_m(\eta) c_{ns}(h) + d_m(\eta) d_{ns}(h) \right)$$

$$\times \left( \vec{M}_{-i\eta}^1(r,\phi,z) \times \vec{N}_{-\ell h}^1(r,\phi,z) \right.$$

$$\left. \left. + \vec{N}_{-i\eta}^1(r,\phi,z) \times \vec{M}_{-\ell h}^1(r,\phi,z) \right) \right] \cdot \hat{r} r_1 \, d\phi \, dz$$

As in the case for $I_2$, it follows from the vector orthogonality properties developed in Appendix C that the terms involving the products $\vec{M}_{-i\eta}^1 \times \vec{M}_{-\ell h}^1 \cdot \hat{r}$ and $\vec{N}_{-i\eta}^1 \times \vec{N}_{-\ell h}^1 \cdot \hat{r}$ have zero contribution to the integral for $I_3$. Also, it follows from Equations (C-3) and (C-4) that the contribution of the term $\vec{M}_{-i\eta}^1 \times \vec{N}_{-\ell h}^1 \cdot \hat{r}$ is exactly cancelled by that of the term $\vec{N}_{-i\eta}^1 \times \vec{M}_{-\ell h}^1 \cdot \hat{r}$. Thus $I_3$ is identically zero.

The integral for $I_4$ will be evaluated assuming that the waveguide feeder for the probe antenna will support only the dominant $TE_{10}$ mode. (This is not a restrictive assumption, for the same result will be obtained assuming any other mode or combination of modes. Only the final constant of proportionality will differ.) The assumed transverse fields in the waveguide are of the form

$$E_{az'}(x',y',z') = K\cos\frac{\pi y'}{a} e^{j\beta x'} \qquad (2\text{-}75)$$

$$H_{ay'}(x',y',z') = \frac{K}{Z_w} \cos \frac{\pi y'}{a} e^{j\beta x'} \tag{2-76}$$

$$E_{bz'}(x',y',z') = \cos \frac{\pi y'}{a} e^{-j\beta x'} \tag{2-77}$$

$$H_{by'}(x',y',z') = \frac{1}{Z_w} \cos \frac{\pi y'}{a} e^{-j\beta x'} \tag{2-78}$$

where $\beta$ is the propagation constant in the waveguide, $a$ is the width of the waveguide, and $Z_w$ is the wave impedance. The fields have been normalized so that the electric field at the center of the waveguide has unit magnitude when generator B alone is activated.

When these expressions are substituted into the integrand of $I_4$, the result is

$$I_4 = -\frac{K}{Z_w} \int_{-\frac{b}{2}}^{\frac{b}{2}} \int_{-\frac{a}{2}}^{\frac{a}{2}} 2\cos^2 \frac{\pi y'}{a} dx' dy' \tag{2-79}$$

$$= -\frac{abK}{Z_w}$$

Since the voltage induced across the output impedance of generator B when only generator A is activated is proportional to K, the expression for $I_4$ will be written

$$I_4 = -C \frac{ab}{Z_w} v(r_o, \phi_o, z_o) \tag{2-80}$$

where C is the constant of proportionality and $v(r_o, \phi_o, z_o)$ is the voltage induced.

It follows from the previous results that Equation (2-57) reduces to

$$C \frac{ab}{Z_w} v(r_o, \phi_o, z_o) = \frac{8\pi\Lambda^2}{\omega\mu} \sum_{n=-\infty}^{\infty} e^{jn\phi_o} \int_{-\infty}^{\infty} \left[ a_n(h) \sum_{n=-\infty}^{\infty} c_m(-h) H_{n+m}^{(2)}(\Lambda r_o) \right.$$ (2-81)

$$\left. + b_n(h) \sum_{n=-\infty}^{\infty} d_m(-h) H_{n+m}^{(2)}(\Lambda r_o) \right] e^{-jhz_o} dh$$

The voltage induced across the probe load will be normalized by choosing the constant of proportionality $C = 32\pi^3 Z_w k^2 / \omega\mu ab$. With this choice the normalized voltage becomes

$$v(r_o, \phi_o, z_o) = \frac{\Lambda^2}{4\pi^2 k^2} \sum_{n=-\infty}^{\infty} e^{jn\phi_o} \int_{-\infty}^{\infty} \left[ a_n(h) \sum_{m=-\infty}^{\infty} c_m(-h) H_{n+m}^{(2)}(\Lambda r_o) \right.$$ (2-82)

$$\left. + b_n(h) \sum_{m=-\infty}^{\infty} d_m(-h) H_{n+m}^{(2)}(\Lambda r_o) \right] e^{-jhz_o} dh$$

Examination of this equation reveals that $v(r_o, \phi_o, z_o)$ is in the form of a Fourier series in $\phi_o$ and a Fourier integral in $z_o$. Thus it follows that the equation has an inverse which is given by

$$a_n(h) \sum_{m=-\infty}^{\infty} c_m(-h) H_{n+m}^{(2)}(\Lambda r_o) + b_n(h) \sum_{m=-\infty}^{\infty} d_m(-h) H_{n+m}^{(2)}(\Lambda r_o)$$ (2-83)

$$= \frac{k^2}{\Lambda^2} \int_{-\infty}^{\infty} \int_{-\pi}^{\pi} v(r_o, \phi_o, z_o) e^{-jn\phi_o} e^{jhz_o} d\phi_o dz_o$$

This expression is the desired result. It relates the cylindrical wave

amplitude weighting functions $a_n(h)$ and $b_n(h)$ of an arbitrary antenna to the two-dimensional Fourier transform of the output voltage $v(r_o, \phi_o, z_o)$ **of a probe when the measurement surface is a cylinder of radius $r_o$.**

If the cylindrical wave amplitude weighting functions for the probe antenna are known, it can be seen that the above expression can be solved for $a_n(h)$ and $b_n(h)$ provided two independent measurements of $v(r_o, \phi_o, z_o)$ are made. Let $v'(r_o, \phi_o, z_o)$ represent the voltage output of the probe antenna when it is rotated 90° about its longitudinal axis. If the rotated probe cylindrical wave amplitude weighting functions are denoted by $c'_m(\eta)$ and $d'_m(\eta)$, the above equation becomes

$$a_n(h) \sum_{m=-\infty}^{\infty} c'_m(-h) H_{n+m}^{(2)}(\Lambda r_o) + b_n(h) \sum_{m=-\infty}^{\infty} d'_m(-h) H_{n+m}^{(2)}(\Lambda r_o) \qquad (2\text{-}84)$$

$$= \frac{k^2}{\Lambda^2} \int_{-\infty}^{\infty} \int_{-\pi}^{\pi} v'(r_o, \phi_o, z_o) e^{-jn\phi_o} e^{jhz_o} d\phi_o dz_o$$

When this equation and Equation (2-83) are solved simultaneously, it is found that the functions $a_n(h)$ and $b_n(h)$ are given by

$$a_n(h) = \frac{k^2}{\Lambda^2 \Delta_n(h)} \left[ I_n(h) \sum_{m=-\infty}^{\infty} d'_m(-h) H_{n+m}^{(2)}(\Lambda r_o) \right. \qquad (2\text{-}85)$$

$$\left. - I'_n(h) \sum_{m=-\infty}^{\infty} d_m(-h) H_{n+m}^{(2)}(\Lambda r_o) \right]$$

$$b_n(h) = \frac{k^2}{\Lambda^2 \Delta_n(h)} \left[ I'_n(h) \sum_{m=-\infty}^{\infty} c_m(-h) H_{n+m}^{(2)}(\Lambda r_o) \right. \qquad (2\text{-}86)$$

$$- I_n(h) \sum_{m=-\infty}^{\infty} c_m'(-h) H_{n+m}^{(2)}(\Lambda r_o) \Bigg]$$

where

$$I_n(h) = \int_{-\infty}^{\infty} \int_{-\pi}^{\pi} v(r_o, \phi_o, z_o) e^{-jn\phi_o} e^{jhz_o} d\phi_o dz_o \qquad (2\text{-}87)$$

$$I_n'(h) = \int_{-\infty}^{\infty} \int_{-\pi}^{\pi} v'(r_o, \phi_o, z_o) e^{-jn\phi_o} e^{jhz_o} d\phi_o dz_o \qquad (2\text{-}88)$$

$$\Delta_n(h) = \left[ \sum_{m=-\infty}^{\infty} c_m(-h) H_{n+m}^{(2)}(\Lambda r_o) \right] \left[ \sum_{m=-\infty}^{\infty} d_m'(-h) H_{n+m}^{(2)}(\Lambda r_o) \right] \qquad (2\text{-}89)$$

$$- \left[ \sum_{m=-\infty}^{\infty} c_m'(-h) H_{n+m}^{(2)}(\Lambda r_o) \right] \left[ \sum_{m=-\infty}^{\infty} d_m(-h) H_{n+m}^{(2)}(\Lambda r_o) \right]$$

Equations (2-85) through (2-89) form the basis of the method for the determination of the far field of an arbitrary antenna from measurements made with a probe on a cylinder containing the antenna. By using these equations to determine the cylindrical wave amplitude weighting functions $a_n(h)$ and $b_n(h)$, the far field of the antenna can be determined from Equations (2-43) and (2-44). Since the far field is determined from only those values of $a_n(h)$ and $b_n(h)$ for which $-k \leq h \leq k$, it follows that the cylindrical wave amplitude weighting functions of the probe need be known only for arguments inside this interval. Thus the specification of the far field radiated by the probe is sufficient to calculate the probe compensated far field of the test antenna. In the next

chapter a numerical method is described for obtaining the cylindrical wave amplitude weighting functions for the probe antenna from its measured far field over a sphere containing the probe. Also, a numerical solution based on the Fast Fourier Transform algorithm is developed for the probe compensated far field of the test antenna.

## 2.5  Spatial Sampling on the Cylinder

Since the measurement of the near field of any antenna over some surface enclosing the antenna potentially requires the accumulation of a large amount of data, the problem of determining an optimum spatial sampling rate is one of great practical importance. Sampling rates which are too high result in the acquisition of more data than are necessary to characterize a given near field, while rates that are too low result in data which may be meaningless. In this section, the a priori determination of a reasonable sampling rate on a cylinder enclosing the antenna is discussed. Specifically, high-Q antennas, such as supergain antennas, will be excluded from the discussion since no a priori upper bound on the required sampling rate for such antennas can be specified. The exclusion of this class of antennas is not restrictive in most cases since they are rarely if ever encountered in practice.

To establish a sampling criterion for the near field on a cylinder enclosing an antenna, the variation of the field with the coordinates on the cylinder can be studied by examination of the cylindrical wave expansions developed in Section 2.2. It was shown that each component of the field on a cylinder can be written in the form of a Fourier series in the azimuth angle $\phi$ and a Fourier integral in the axial

distance z. Thus it follows that the results of the sampling theory of Fourier transform analysis can be used to establish a sample spacing criterion on the cylinder if upper bounds on the angular harmonic n and the wavenumber h can be determined. An examination of the antenna quality factor, or Q, is one means of establishing these bounds.

The Q of an antenna is an important parameter which can be related to the effect of the antenna size on gain, bandwidth, and efficiency. A high Q means that a large amount of reactive energy is stored in the near field of the antenna. This implies large currents on the antenna structure, high ohmic losses, a narrow bandwidth, and extreme frequency sensitivity. Although it is difficult in general to relate the antenna Q to the degree to which it is a supergain structure, it has been shown that a supergain antenna is necessarily a high-Q antenna (25). Thus the exclusion of high-Q antennas from the discussion will also exclude supergain antennas.

The Q of an antenna which has been tuned to resonance by the addition of a reactive element is defined as (26)

$$Q = \frac{2\omega \max\{W^m, W^e\}}{P} \qquad (2\text{-}90)$$

where $W^m$ and $W^e$ are the time average magnetic and electric energies stored in the near field of the antenna and P is the total power radiated by the antenna. If the Q of a single cylindrical wave with mode indices n and h is defined as

$$Q_{nh} = \frac{2\omega \max\{W_{nh}^m, W_{nh}^e\}}{P_{nh}} \qquad (2\text{-}91)$$

it follows from Equation (2-90) that the Q of an antenna which radiates a spectrum of cylindrical waves is given by the linear combination

$$Q = \frac{\sum\limits_{n=-\infty}^{\infty} \int\limits_{-\infty}^{\infty} |C_{nh}|^2 P_{nh} Q_{nh}\, dh}{\sum\limits_{n=-\infty}^{\infty} \int\limits_{-\infty}^{\infty} |C_{nh}|^2 P_{nh}\, dh} \qquad (2\text{-}92)$$

where $C_{nh}$ is the complex amplitude of the cylindrical wave with mode indices n and h. This equation is simply a weighted average of the $Q_{nh}$ over all n and h, where the weighting factors are $|C_{nh}|^2 P_{nh}$.

Collin and Rothschild (26) have evaluated $P_{nh}$ and $Q_{nh}$ for a single cylindrical wave radiated by an ideal, loss-free antenna of radius $a$. The term "ideal, loss-free antenna of radius $a$" was originally defined by Chu (27) as one having no energy storage for R < a, where R is the spherical radial distance from the center of the smallest sphere of radius $a$ completely enclosing the antenna. In the present case, it is interpreted as an antenna for which there is no energy storage for r < a, where $a$ is the radius of the smallest cylinder completely enclosing the antenna. The Q for this ideal antenna must be less than or equal to that for any other loss-free antenna fitting into the cylinder r = a, since any field for r < a can only add to the energy storage.

The expressions for $P_{nh}$ and $Q_{nh}$ for $(TE)_z$ and $(TM)_z$ cylindrical waves are identical and are given by (26)

$$P_{nh} = \frac{2(k^2-h^2)}{\omega\mu} \qquad (2-93)$$

$$Q_{nh} = \frac{\pi k^2}{4(k^2-h^2)} \left\{ \frac{4\Lambda a}{\pi} + [(n^2+1-\Lambda^2 a^2)(J_n^2+Y_n^2)] \right. \qquad (2-94)$$

$$\left. - [(n+1)J_n-\Lambda a J_{n+1}]^2 - [(n+1)Y_n-\Lambda a Y_{n+1}]^2 \right\}$$

where $h < k$ and the argument of the Bessel functions is $\Lambda a = (k^2-h^2)^{\frac{1}{2}}a$. For $h \geq k$, $P_{nh} = 0$ and $Q_{nh}$ is undefined.

Collin and Rothschild (26) have shown that the quantity $\left(\frac{k^2-h^2}{h^2}\right) Q_{nh} = \frac{\pi}{\omega\epsilon} P_{nh}Q_{nh}$ increases very rapidly when n becomes larger than $\Lambda a$. Since this term, aside from the factor $\frac{\pi}{\omega\epsilon}$, appears in the numerator of the general expression for Q in Equation (2-92), it follows that Q can become large if $C_{nh}$ is not small for $n > \Lambda a$. Since $\Lambda \leq k$ for real h, it follows that the highest significant angular harmonic in the cylindrical wave expansion of the fields of an antenna which is not a high-Q structure is N = ka. If $a$ is taken to be the radius of the smallest sphere completely enclosing the antenna, this result agrees with the conclusions reached by Chu (27) and Harrington (25) in studying the physical limitations of antennas using spherical wave expansions. In general, however, the radius of the smallest cylinder completely enclosing an antenna is less than or equal to the radius of the smallest sphere, the two being equal if the antenna is oriented so that its longest dimension is perpendicular to the axis of the cylinder.

A sample spacing criterion for the azimuth angle $\phi$ on a cylinder enclosing an antenna can be obtained by applying the Nyquist sampling

criterion of Fourier transform theory to the above result. If N is the maximum angular harmonic in the cylindrical wave expansion of a given field, then it follows that the maximum angular separation between adjacent samples is

$$\Delta\phi = \frac{\pi}{N} \qquad (2\text{-}95)$$

In this case N must be chosen as the smallest integer greater than ka, where $a$ is the radius of the smallest cylinder completely enclosing the antenna.

The above limit on N has been verified by Ludwig (28) for a particular antenna. He has shown that over 99.9 per cent of the total power radiated by a circular aperture horn is contained in spherical waves with angular harmonics $|n| \leq ka$, where $a$ is the radius of the smallest sphere containing the aperture. Since $a$ is a function of the location of the origin of the sphere with respect to the center of the aperture, he was able to elegantly demonstrate the variation of the maximum significant angular harmonic with the radius of the sphere by varying the position of the origin. Since both cylindrical wave and spherical wave expansions are in the form of a Fourier series in the azimuth angle $\phi$, it follows that his results are directly applicable to cylindrical wave expansions for this particular antenna for which the radius of the smallest cylinder completely enclosing the antenna is the same as the radius of the smallest sphere.

A z-sample spacing criterion follows in a similar manner. Collin and Rothschild (26) have shown that the term $P_{nh}Q_{nh}$ in Equation (2-92) increases rapidly for $|n| \geq (k^2-h^2)^{\frac{1}{2}}a$. Thus it follows that $|C_{nh}|$ must be small for $h^2 > k^2 - \frac{n^2}{a^2}$. This implies that the highest significant wavenumber in the cylindrical wave expansion of the field of an antenna which is not a high-Q structure is $|h| \leq k$. It follows that the maximum z-sample spacing on the cylinder is given by the Nyquist spacing

$$\Delta z = \frac{\pi}{k} \qquad\qquad (2\text{-}96)$$

$$= \frac{\lambda}{2}$$

It is interesting to compare the two sample spacing criteria which have been developed. If the measurement cylinder is the smallest cylinder completely enclosing the antenna, then it follows that the arc length on the cylinder separating adjacent sample points when sampling in the azimuth direction is

$$\Delta s = a\Delta\phi \qquad\qquad (2\text{-}97)$$

$$= \frac{\pi}{k}$$

$$= \frac{\lambda}{2}$$

This is the same as the z-sample spacing with the exception that $\Delta s > \Delta z$

when sampling on a cylinder of radius greater than $a$.

Although the sample spacing criteria defined by Equations (2-95) and (2-96) are useful, they are in no way absolute, for it is impossible to predict a priori an exact cutoff harmonic for n and an exact cutoff wavenumber for h in the cylindrical wave expansion of the fields radiated by a given antenna.  In practice, more conservative sample spacings have been used.  For example, Collin and Zucker (29) state that the maximum order angular harmonic in the cylindrical wave expansion of the field radiated by an aperture on a cylinder is approximately 2ka, where $a$ is the radius of the cylinder.  This would lead to a sample spacing in the $\phi$ direction of one-half that specified by Equation (2-95).  Joy and Paris (2) have obtained excellent results in the calculation of the far-field patterns of reflector antennas using a sample spacing of $\lambda/3$ on a plane located in front of the antenna.  This spacing effectively allows for a 50 per cent error in the $\lambda/2$ criterion.  In the actual measurement of the near field of an antenna, therefore, the sample spacings specified by Equations (2-95) and (2-96) should be used as guidelines in determining the sample spacing between measurement points.  In most instances, the sample spacings chosen can be easily verified experimentally on the near-field antenna range.

CHAPTER III

NUMERICAL CONSIDERATIONS

### 3.1  Introduction

The numerical approach taken to solve for the far field of the test antenna used in the experimental phase of the research is described in this chapter.  The numerical work centers around the application of the Fast Fourier Transform (or FFT) algorithm to evaluate the necessary integrals and to sum the final Fourier series for the far field of the antenna.  The use of the FFT for far-field calculations requires careful choice of sample rates in order for the calculated field to lie in the visible region of space.  A technique of near-field data processing has been developed which makes it possible to control the region of visible space in which the calculated field lies.

To compensate for the effects of the measurement probe in the far-field calculations, it is necessary to know the cylindrical wave amplitude weighting functions in the cylindrical wave expansion of the field radiated by the probe when it is used as a transmitter.  A numerical method is described for determining these functions from the measured far field of the probe over the surface of a sphere containing it.

The chapter is concluded with a test of the computer algorithms. A far-field pattern of an aperture on a conducting cylinder is calculated and shown to be identical to results found in the literature.

### 3.2 Method of Evaluating the Far
### Field from Measured Data

In Section 2.3 it was shown that over the surface of a sphere of radius R, the far-field electric field intensity radiated by an antenna can be written in the form

$$E_\theta(\theta,\phi) = j\sin\theta \sum_{n=-\infty}^{\infty} j^n b_n(k\cos\theta)e^{jn\phi} \qquad (3-1)$$

$$E_\phi(\theta,\phi) = \sin\theta \sum_{n=-\infty}^{\infty} j^n a_n(k\cos\theta)e^{jn\phi} \qquad (3-2)$$

where the constant factor $-2k^{-jkR}/R$ has been suppressed in each equation. In these equations $a_n(h)$ and $b_n(h)$, where $h = k\cos\theta$, are the amplitude weighting functions of the cylindrical wave vectors $\vec{M}$ and $\vec{N}$, respectively, in the cylindrical wave expansion of the field radiated by the antenna. In Section 2.4 an analytical method was developed to solve for these weighting functions from the voltage output of a probe when it is used to measure the near field of the antenna over the surface of a cylinder enclosing the antenna. In this section a numerical solution for $a_n(h)$ and $b_n(h)$ is developed which is based on this method. The numerical evaluation of Equations (3-1) and (3-2) for the far field of the antenna is then described.

Aside from the factors involving the amplitude weighting functions of the probe when it is used as a transmitter, it was shown in Section 2.4 that the solution for $a_n(h)$ and $b_n(h)$ requires the evaluation of the integrals

$$I_n(h) = \int_{-\infty}^{\infty} \int_{-\pi}^{\pi} v(r_o,\phi_o,z_o)e^{-jn\phi_o}e^{jhz_o} d\phi_o dz_o \qquad (3\text{-}3)$$

$$I_n'(h) = \int_{-\infty}^{\infty} \int_{-\pi}^{\pi} v'(r_o,\phi_o,z_o)e^{-jn\phi_o}e^{jhz_o} d\phi_o dz_o \qquad (3\text{-}4)$$

where $v(r_o,\phi_o,z_o)$ and $v'(r_o,\phi_o,z_o)$ represent the output voltage of the probe on the measurement cylinder of radius $r_o$. The primed function is used to denote the probe output after it is rotated 90° about its longitudinal axis.

Let the measurement cylinder be divided into a lattice of points with coordinates $(r_o,n\Delta\phi,m\Delta z)$ where $0 \le n \le N-1$, $0 \le m \le M-1$, and M and N are positive integers. To exactly evaluate Equations (3-3) and (3-4) from the output voltages of the probe at these points, two conditions must be satisfied. First, v and v' must be zero when z < 0 or z > (M-1)$\Delta z$. Second, v and v' must have no angular harmonic n greater than $\pi/\Delta\phi$ and must be wavenumber limited in h to a maximum wavenumber less than or equal to $\pi/\Delta z$. The first condition cannot be met with any radiating structure. However, if the test antenna is aligned in the cylinder so that it does not radiate appreciably in the ±z direction, it can be met approximately if M is chosen large enough. The second condition can be met if the test antenna is not a high-Q structure and the sample intervals $\Delta\phi$ and $\Delta z$ are chosen in accordance with the sampling criteria discussed in Section 2.5. Assuming these conditions are met, the integrals for $I_n(h)$ and $I_n'(h)$ can be evaluated most efficiently with a two-dimensional Fast Fourier Transform (or FFT) algorithm (30).

The FFT is an algorithm in which the computations are performed
"in place," i.e., the two-dimensional input data arrays $v(r_o, n\Delta\phi, m\Delta z)$
and $v'(r_o, n\Delta\phi, m\Delta z)$ are replaced by the output arrays $I_n(m\Delta h)$ and $I'_n(m\Delta h)$
after the calculations are completed. As described by Cochran (30) the
output values of the integers m and n are

$$-\frac{M}{2} \le m \le \frac{M}{2} - 1 \tag{3-5}$$

$$-\frac{N}{2} \le n \le \frac{N}{2} - 1 \tag{3-6}$$

and $\Delta h$ is given by

$$\Delta h = \frac{2\pi}{M\Delta z} \tag{3-7}$$

Since the far-field expressions for $E_\theta(\theta,\phi)$ and $E_\phi(\theta,\phi)$ are evaluated at
$h = k\cos\theta$, the values of $\theta$ corresponding to $h = m\Delta h$ are given by

$$\theta_m = \cos^{-1}\left(\frac{m\lambda}{M\Delta z}\right) \tag{3-8}$$

Since it is impossible to measure the near field over a complete
cylinder enclosing an antenna, the present method for determining the
far field of the test antenna is most suitable when applied to antennas
which radiate predominantly in the annular region about $\theta = \frac{\pi}{2}$ defined by
$\theta_c < \theta \le \pi - \theta_c$. In order for all $\theta_m$ defined by Equation (3-8) to lie
in this interval, it follows that $\Delta z$ must satisfy

$$\Delta z = \frac{\lambda}{2\cos\theta_c} \tag{3-9}$$

However, for $\theta_c \neq 0$, this condition violates the z-sample spacing criterion discussed in Section 2.5. One solution to this problem is to choose $\Delta z$ smaller than that specified by Equation (3-9) and to ignore the calculations for $\theta \leq \theta_c$ and $\theta > \pi - \theta_c$. This is not a very efficient solution since it reduces the resolution of the calculated fields for $\theta_c < \theta \leq \pi - \theta_c$. The decrease in resolution can be overcome by augmenting the near-field data arrays with zeroes, thereby increasing M. Although this is an acceptable solution, it is inefficient for it increases computer storage requirements, increases computation time, and does not make full use of the FFT computations.

An alternate solution to the above problem is to first "smooth" the near-field data in such a way that it can be resampled by numerical interpolation with the sample spacing specified by Equation (3-9). The "smoothing" operation can be accomplished efficiently with the FFT algorithm. First, the near-field data arrays are transformed in z so that on output the wavenumber spacing is that specified by Equation (3-7). Second, all elements in the transformed arrays are set equal to zero for all m such that

$$|m| > \frac{M\Delta z}{\lambda} \cos\theta_c \tag{3-10}$$

Finally, the data arrays are inverse transformed to create the "smoothed" arrays. This operation is equivalent to that of filtering the data with

an ideal "low-pass filter" with a cutoff wavenumber given by

$$h_c = \frac{2\pi}{\lambda} \cos\theta_c \tag{3-11}$$

After the "smoothing" operation, the near-field data arrays are wavenumber limited in z such that the Nyquist sample spacing is that given by Equation (3-9). Thus the arrays can be resampled in z using numerical interpolation with the sample spacing specified by Equation (3-9). In order to preserve "in place" calculations, the interpolated arrays can directly replace the original arrays during the computations. Since the interpolation process will extract fewer than M samples in z, it is necessary to set equal to zero some of the elements of the original arrays after the interpolation. It can be shown that these zeros will not affect the accuracy of the subsequent FFT operations. Instead, the resolution will be improved on output since all M values of $\theta_m$ will lie in the interval $\theta_c < \theta \leq \pi - \theta_c$.

After the evaluation of $I_n(m\Delta h)$ and $I_n'(m\Delta h)$, the cylindrical wave amplitude weighting functions $a_n(m\Delta h)$ and $b_n(m\Delta h)$ can be solved for using Equations (2-85) and (2-86). The evaluation of the coefficients in these equations which are determined by the probe will be discussed in Section 3.3. Since $a_n(m\Delta h)$ and $b_n(m\Delta h)$ are both linear combinations of $I_n(m\Delta h)$ and $I_n'(m\Delta h)$, the computations can again be performed "in place." Thus on output, the original data arrays will contain the set of cylindrical wave amplitude weighting functions from which the far field of the test antenna can be evaluated.

The calculation of the far-field electric field intensity radiated by the test antenna can be achieved by performing the summations indicated by Equations (3-1) and (3-2). Again, this can be done most efficiently with the FFT algorithm. However, each $a_n(m\Delta h)$ and $b_n(m\Delta h)$ must be multiplied by the factors $j^n\sin\theta_m$ and $j^{n+1}\sin\theta_m$, respectively, before the FFT can be used to perform the summations. Since the calculations are performed "in place" the output arrays will be the far-field components $E_\theta(\theta_m,\phi_n)$ and $E_\phi(\theta_m,\phi_n)$ where

$$\phi_n = \frac{2n\pi}{N}, \qquad 0 \le n \le N-1 \qquad (3-12)$$

$$\theta_m = \cos^{-1}\left[\frac{m\cos\theta_c}{(M/2)}\right], \qquad -\frac{M}{2} \le m \le \frac{M}{2} - 1 \qquad (3-13)$$

The complete calculations are summarized in the flow-diagram of Figure 4.

### 3.3  Evaluation of the Probe Compensation Coefficients

To evaluate Equations (2-85) and (2-86) for the amplitude weighting functions in the cylindrical wave expansion of the far field radiated by the test antenna, it is necessary to know the amplitude weighting functions in the expansion of the field radiated by the probe. Since it is necessary to know these functions only for wavenumbers such that $|h| \le k$, it is possible to obtain them from a knowledge of the far field radiated by the probe when it is connected to a signal source. In this section, a numerical procedure is developed for obtaining the necessary probe information from the measured far field of the probe.

```
┌─────────────────────────┐        ┌─────────────────────────┐
│   Obtain Probe Far-Field│        │    Enter Near-Field     │
│   E_θ(θ',φ') and        │        │   E_φ(r_o,φ_o,z_o) and  │
│      E_φ(θ',φ')         │        │     E_z(r_o,φ_o,z_o)    │
└───────────┬─────────────┘        └────────────┬────────────┘
            │                                    │
            ▼                                    ▼
┌─────────────────────────┐        ┌─────────────────────────┐
│   Compute and Store     │        │   "Low Pass Filter" in  │
│  Probe Cylindrical Wave │        │  z and Resample with the│
│     Coefficients        │        │    Spacing Given by     │
│ (Solve Eq. (3-19), etc.)│        │    Equation (3-9)       │
└───────────┬─────────────┘        └────────────┬────────────┘
            │                                    │
            ▼                                    ▼
┌─────────────────────────┐        ┌─────────────────────────┐
│  Enter Probe Coefficients│       │ Two-Dimensional FFT to  │
│   c_n(mΔh), d_n(mΔh),   │        │  Solve for I_n(mΔh)     │
│  c'_n(mΔh), and d'_n(mΔh)│       │ and I'_n(mΔh) Given by  │
│                         │        │Equations (3-3) and (3-4)│
└───────────┬─────────────┘        └────────────┬────────────┘
            │                                    ▼
            │                      ┌─────────────────────────┐
            ├──────────────────────►  Solve Equations (2-85) │
            │                      │    and (2-86) for       │
            │                      │      a_n(mΔh) and       │
        ┌───┴──────────────────────►      b_n(mΔh)          │
        │                          └────────────┬────────────┘
┌───────┴─────────────────┐                     ▼
│   Evaluate Hankel       │        ┌─────────────────────────┐
│ Functions H_{n+m}^(2)(Λr_o)│     │   One-Dimensional FFT   │
│ in Equations (2-85)     │        │    to Sum Equations     │
│    and (2-86)           │        │      (3-1) and (3-2)    │
└─────────────────────────┘        └────────────┬────────────┘
                                                 ▼
                                   ┌─────────────────────────┐
                                   │    Output Far-Field     │
                                   │   E_φ(θ_m,φ_n) and      │
                                   │     E_θ(θ_m,φ_n)        │
                                   └─────────────────────────┘
```
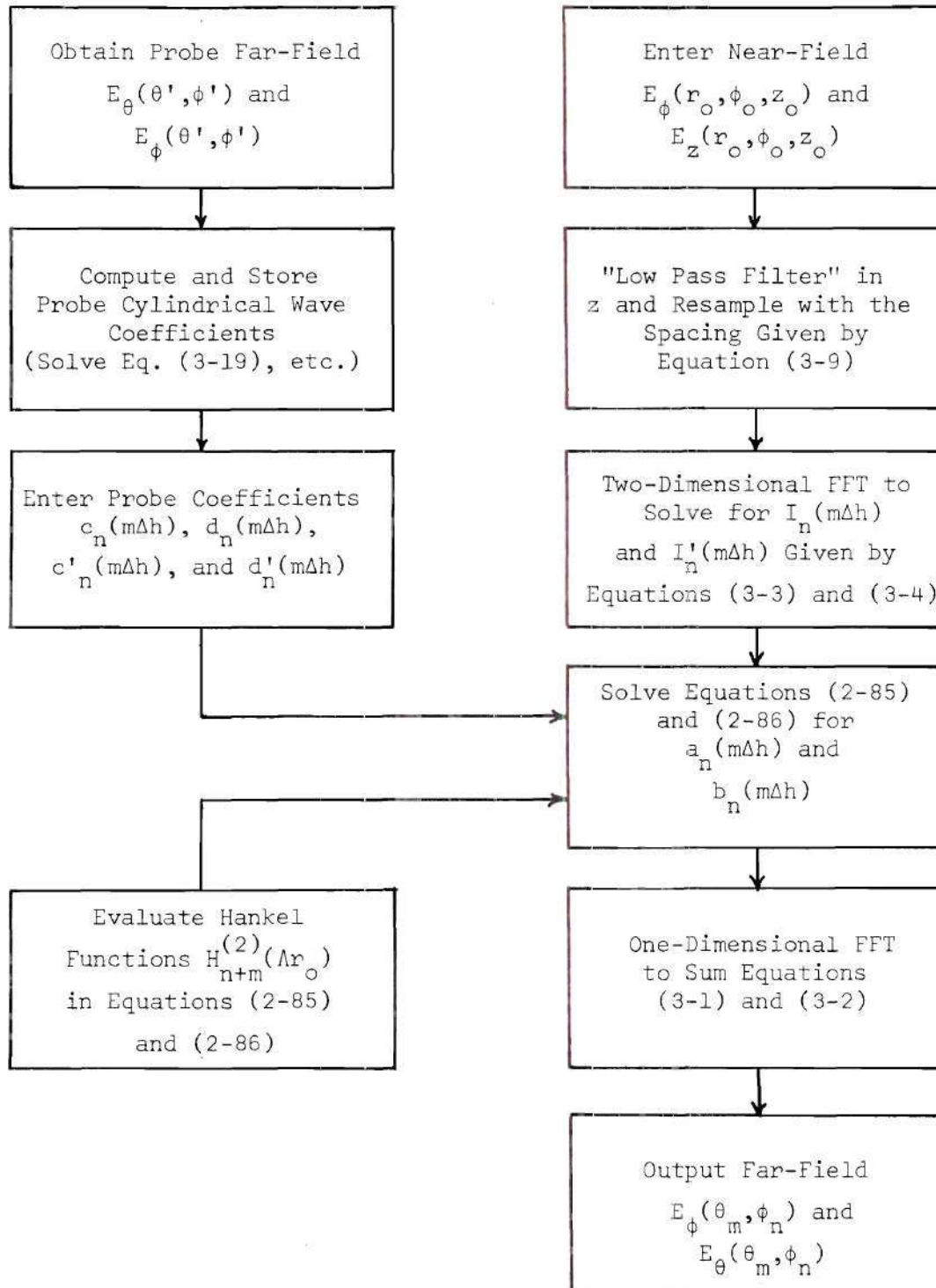
Figure 4.   Flow-Diagram for the Far Field Evaluation

Two near-field probes were used in the experimental phase of the research, one an open-end WR-90 waveguide and the other a WR-90 waveguide terminating in a pyramidal horn with a 5.7° E-plane half-angle flare and a 15.7° H-plane half angle flare. The aperture dimensions of the two probes were 1" × 0.5" and 1.88" × 0.81", respectively. The two probes had been calibrated at 9.68 GHz for use with the near-field range at Georgia Tech (2). The calibration data consisted of the measured amplitude and phase of the far-field components $E_\theta(\theta,\phi)$ and $E_\phi(\theta,\phi)$ of the probes over a sector of a sphere defined by $30° \leq \theta \leq 150°$ and $-60° \leq \phi \leq 60°$. The step sizes in the far-field data were $\Delta\theta = 5°$ and $\Delta\phi = 1°$.

Since it is necessary to resolve the measured probe data into Fourier series in the azimuth angle $\phi$, some upper limit on the maximum angular harmonic for each probe must be established. This can be done by using the criterion established by Harrington (25) that the maximum angular harmonic is $N = ka$, where in this case $a$ is the radius of the smallest sphere completely enclosing the aperture of the probe. At 9.68 GHz, it follows that the smallest integer greater than ka for each probe is $N = 3$ for the open-end waveguide and $N = 6$ for the small horn.

Let the probe antenna be oriented as shown in Figure 5. The far-field electric field intensity radiated by the probe can be expressed as

$$E_\theta(\theta,\phi) = j\sin\theta \sum_{n=-N}^{N} j^n d_n(k\cos\theta)e^{jn\phi} \qquad (3-14)$$

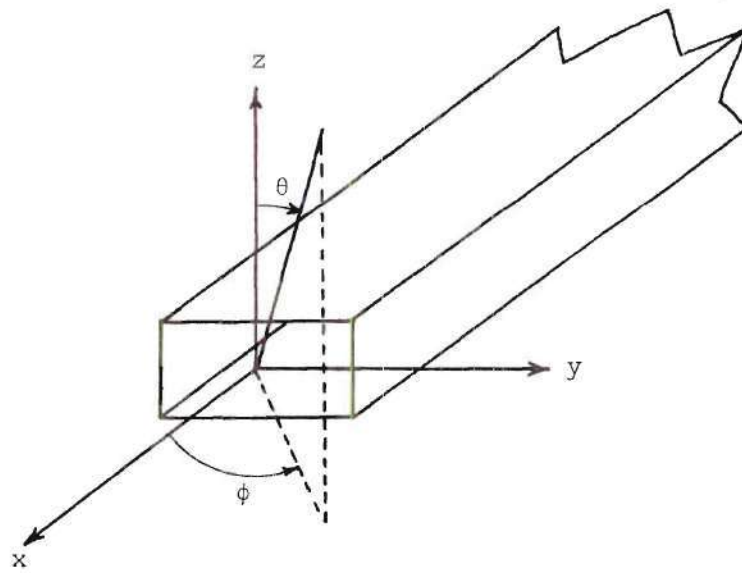$$E_\phi(\theta,\phi) = \sin\theta \sum_{n=-N}^{N} j^n c_n(k\cos\theta)e^{jn\phi} \qquad (3-15)$$

Figure 5. Coordinate System for the Probe Antenna

where $c_n(h)$ and $d_n(h)$, with $h = k\cos\theta$, are the amplitude weighting functions for the cylindrical wave vectors $\vec{M}$ and $\vec{N}$, respectively, in the expansion of the field radiated by the probe. If the probe is rotated 90° in the right-hand sense about the x-axis, the far-field electric field intensity radiated by the rotated probe can be expressed as

$$E_\theta'(\theta,\phi) = j\sin\theta \sum_{n=-N}^{N} j^n d_n'(k\cos\theta)e^{jn\phi} \tag{3-16}$$

$$E_\phi'(\theta,\phi) = \sin\theta \sum_{n=-N}^{N} j^n c_n'(k\cos\theta)e^{jn\phi} \tag{3-17}$$

where $c_n'(h)$ and $d_n'(h)$ are defined similarly. In order to compensate for the effects of the probe in calculating the far field of the test antenna, it is necessary to know $c_n(h)$, $d_n(h)$, $c_n'(h)$, and $d_n'(h)$ with the argument $h = -k\cos\theta_m$ where $\theta_m$ is the elevation angle for the far field of the test antenna and is defined in Equation (3-13).

Since Equations (3-14) through (3-17) are in the form of a Fourier series in $\phi$, the amplitude weighting functions for a particular value of $\theta$ can be obtained by numerically evaluating the Fourier inversion integral from the measured fields. For example, the solution for $d_n(k\cos\theta)$ is

$$d_n(k\cos\theta) = \frac{1}{2\pi j^{n+1}\sin\theta} \int_{-\pi}^{\pi} E_\theta(\theta,\phi)e^{-jn\phi} \, d\phi \tag{3-18}$$

This solution, however, cannot be used since the measured far field of

the probe is known only for $-60° \leq \phi \leq 60°$. The approach which has been taken for this research was to perform a least squares curve fit of Equations (3-14) through (3-17) to the measured probe data.

For example, it can be shown that Equation (3-14) approximates the measured $E_\theta(\theta, \phi)$ in the least squares sense if the $d_n(k\cos\theta)$ satisfy the system of equations

$$\sum_{n=-N}^{N} d_n(k\cos\theta) \frac{\sin(m-n)\phi_1}{(m-n)\phi_1} = \frac{1}{2j^{m+1}\sin\theta} \int_{-\phi_1}^{\phi_1} E_\theta(\theta, \phi)e^{-jm\phi} \, d\phi \qquad (3-19)$$

where $-N \leq m \leq N$. The $d_n(k\cos\theta)$ for the test probes were obtained by solving this system of equations with the Gauss-Jordan method for solving simultaneous equations. The integral on the right of Equation (3-19) was evaluated from the measured data by using the trapezoidal rule for numerical integration with a step size of $1°$ and $\phi_1 = 60°$. The solutions for $d_n(k\cos\theta)$ were obtained for $-N \leq n \leq N$ and $30° \leq \theta \leq 150°$ with a step size in $\theta$ of $5°$.

Solutions for $c_n(k\cos\theta)$, $d_n'(k\cos\theta)$, and $c_n'(k\cos\theta)$ were obtained for each probe in the same way. However, for the case of the rotated probe functions, it was necessary to solve for $E_\theta'(\theta, \phi)$ and $E_\phi'(\theta, \phi)$ from the measured $E_\theta(\theta, \phi)$ and $E_\phi(\theta, \phi)$. The necessary transformations are

$$E_\theta'(\theta, \phi) = \frac{E_\theta(\xi, \zeta)\cos\theta \, \sin\phi - E_\phi(\xi, \zeta)\cos\phi}{\sqrt{1 - \sin^2\theta \, \sin^2\phi}} \qquad (3-20)$$

$$E_\phi'(\theta, \phi) = \frac{E_\theta(\xi, \zeta)\cos\phi + E_\phi(\xi, \zeta)\cos\theta \, \sin\phi}{\sqrt{1 - \sin^2\theta \, \sin^2\phi}} \qquad (3-21)$$

where

$$\tan\xi = \frac{\sqrt{1 - \sin^2\theta \, \sin^2\phi}}{-\sin\theta \, \sin\phi} \qquad (3\text{-}22)$$

$$\tan\zeta = \frac{\cos\theta}{\sin\theta \, \cos\phi} \qquad (3\text{-}23)$$

In using these equations, $E_\theta(\xi,\zeta)$ and $E_\phi(\xi,\zeta)$ were obtained by numerical interpolation of the measured values.

The amplitude weighting functions for the probe enter into the solutions for $a_n(h)$ and $b_n(h)$ given by Equations (2-85) and (2-86) in the form of summations over the angular harmonics of the probe. The coefficients in the summations are the Hankel functions $H_{n+m}^{(2)}(\Lambda r_o)$ where $\Lambda = \sqrt{k^2 - h^2}$ and m is the angular harmonic of the probe. In the calculation of the far field of the test antenna, it is necessary to evaluate $a_n(h)$ and $b_n(h)$ at $h = k\cos\theta$. Thus, in this case, the argument of the Hankel function is $\Lambda r_o = k r_o \sin\theta$. In the computational phase of the research, these functions were evaluated by using a modification of a method described by Goldstein and Thaler (31-32).

### 3.4  Test of the Computer Algorithms

To test the computer programs which were written to calculate the far field of the test antenna, the far-field pattern of an antenna for which the radiation pattern is known has been calculated. The antenna chosen for the calculations was a narrow circumferential slot on a conducting cylinder. Although there are various methods of synthesizing

aperture distributions for a prescribed far-field azimuth pattern, the slot excitation was chosen to reproduce a result of Bailin (33) who has given extensive data, both tabulated and in curves, for half-wavelength circumferential and axial slots on conducting cylinders with radii ka = 8 and ka = 12.

The geometry of the slot on the cylinder is shown in Figure 6. The assumed electric field intensity in the aperture of the slot was

$$E_\phi(a,\phi,z) = 0 \tag{3-24}$$

$$E_z(a,\phi,z) = A \cos\left(\frac{\pi\phi}{2\phi_o}\right) \tag{3-25}$$

For the calculations, ka was chosen to be 12, one of the values used by Bailin (33). Since no probe compensation could be used with an assumed field distribution on the cylinder, the solutions for the amplitude weighting functions given by Equations (2-31) and (2-32) were used in the computations. Except for the probe compensation coefficients, the flow diagram for the computations in this case is identical to that of Figure 4.

The results of the calculations are shown in Figure 7 where the far-field azimuth pattern of both $E_\theta$ and $E_\phi$ at an elevation angle of $\theta = 30°$ are displayed. These patterns are identical to those calculated by Bailin.
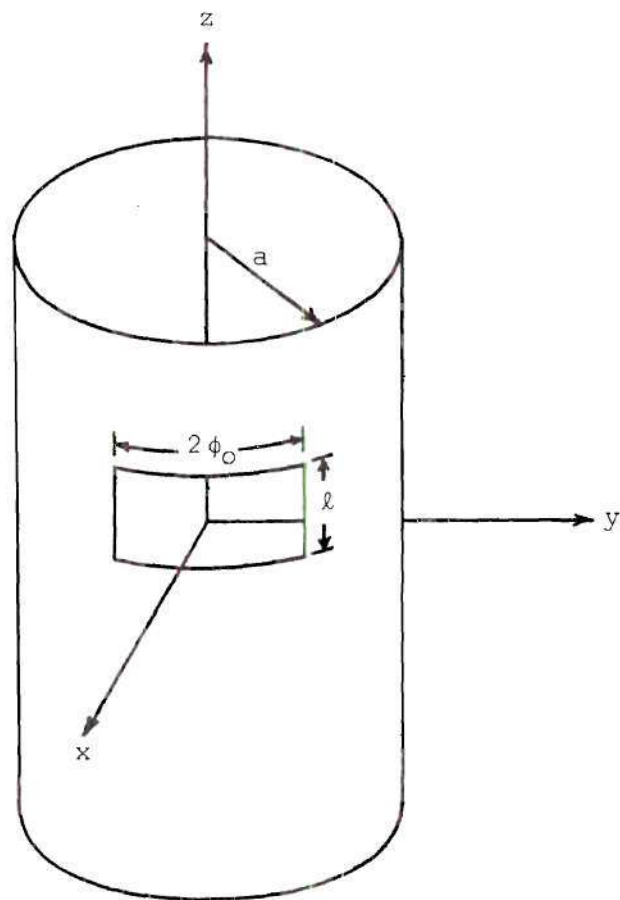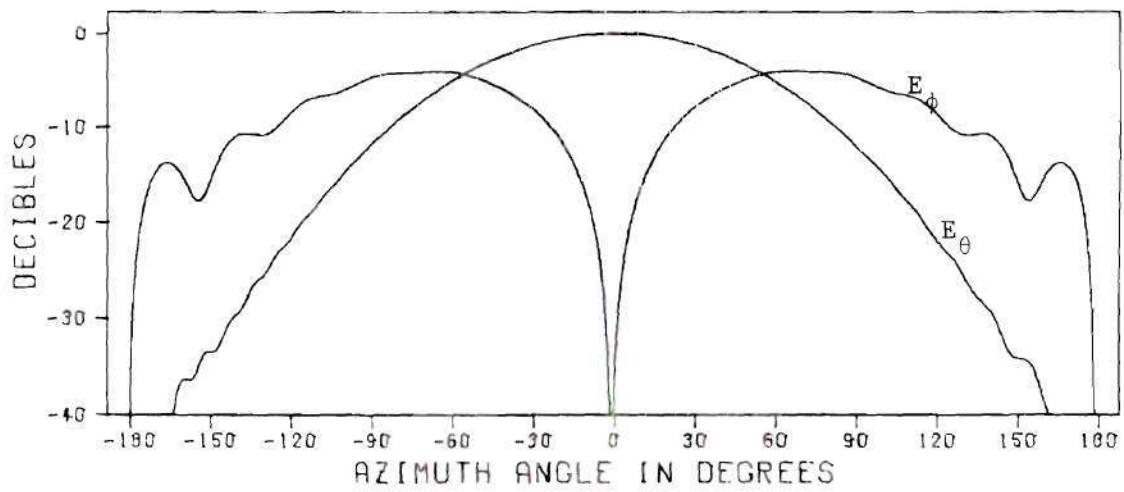
Figure 6.  Geometry of the Slotted Cylinder

Figure 7.   Azimuth Pattern of the Slotted Cylinder
            at an Elevation Angle of 30°

## CHAPTER IV

## INSTRUMENTATION AND EQUIPMENT

### 4.1  Introduction

The object of this chapter is to describe the equipment used in the experimental phase of the research.  The experimental work was performed at the Systems and Techniques Department of the Engineering Experiment Station at Georgia Tech.  The test antenna chosen for the research was a ten-element slotted waveguide array which was fabricated in the machine shop facilities there.  The antenna was designed to radiate a Chebyschev pattern in the far field with side-lobe levels of -20 dB.  Its design is discussed in detail in Section 4.2.

The near-field measurements and the far-field measurements were performed on the near-field range and the phase center range, respectively, at the Systems and Techniques Department.  These facilities are discussed in Section 4.3 and Section 4.4.

### 4.2  The Test Antenna

The design of the antenna that was used in the experimental phase of the research is described in this section.  The choice of the test antenna was based on several considerations.  These were ease of construction, suitability for a cylindrical near-field measurement surface, and predictability of the far-field pattern.  The antenna which was chosen was a ten-element slotted waveguide array.  It was designed to

radiate a broadside Chebyschev pattern at 9.375 GHz with sidelobe levels
of -20 dB. The design of the antenna will be described in two parts.
First, the Chebyschev array synthesis will be discussed. Second, the
design of the slotted waveguide will be discussed. The Cheybschev array
synthesis procedure is described in detail by Collin and Zucker (34).
Thus the following discussion will serve only to document the most
important steps in the design.

Consider a linear array of 2N identical radiators aligned sym-
metrically along the z-axis as shown in Figure 8. Let the complex exci-
tation coefficient for each element in the array be denoted by $a_n$ where
$-N \leq n \leq -1$ or $1 \leq n \leq N$, and let d be the distance between any two
adjacent elements in the array. If the array is excited symmetrically
about z = 0, i.e. $a_{-n} = a_n$, and if all the $a_n$ are real, it follows that
the array factor can be written in the form

$$f(\gamma) = 2 \sum_{i=1}^{N} a_n \cos\left[(2n-1)\frac{\gamma}{2}\right] \qquad (4-1)$$

where

$$\gamma = kd\cos\theta \qquad (4-2)$$

The Chebyschev array excitation coefficients are obtained by
equating Equation (4-1) to the Chebyschev polynomial $T_{2N-1}(b\cos\gamma/2)$ and
solving for the $a_n$, where b > 1 is a parameter. The parameter b is
related to the reciprocal of the sidelobe level R by the equation

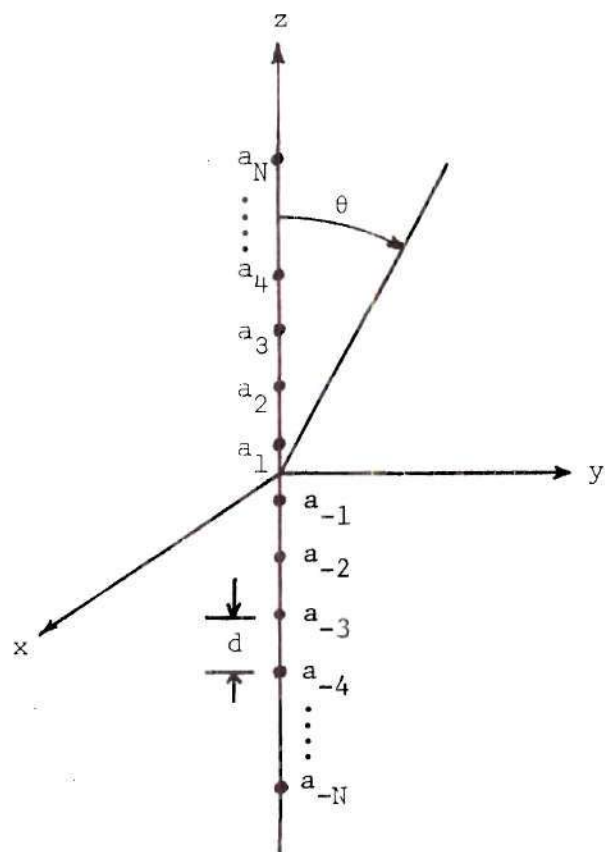Figure 8.  Geometry for the Array Factor

$$b = \cosh\left[\frac{\cosh^{-1}R}{2N - 1}\right] \tag{4-3}$$

For the test antenna, a sidelobe level of -20 dB corresponds to a value of 10 for R. Thus for a ten-element array, i.e. N = 5, the solution for b is

$$b = 1.056 \tag{4-4}$$

The foregoing procedure for obtaining a solution has been carried out for the case of the test antenna. The solutions for the $a_n$ were found to be

$$a_1 = \tfrac{1}{2}[9\,b - 90\,b^3 + 270\,b^5 - 315\,b^7 + 126\,b^9] \tag{4-5}$$

$$= 1.271$$

$$a_2 = \tfrac{1}{2}[-30\,b^3 + 135\,b^5 - 189\,b^7 + 84\,b^9] \tag{4-6}$$

$$= 1.171$$

$$a_3 = \tfrac{1}{2}[27\,b^5 - 63\,b^7 + 36\,b^9] \tag{4-7}$$

$$= 0.988$$

$$a_4 = \tfrac{1}{2}[-9\,b^7 + 9\,b^9] \tag{4-8}$$

$$= 0.755$$

$$a_5 = \tfrac{1}{2} b^9 \tag{4-9}$$

$$= 0.815$$

Since it was assumed that all elements are excited in phase, a ten-element array excited symmetrically according to these coefficients will radiate a broadside Chebyschev pattern with -20 dB sidelobe levels.

The particular slotted waveguide array which was selected for the experimental work was a resonant rectangular waveguide array with longitudinal slots cut in the broad wall of the guide. The resonant array can be designed only for broadside operation and uses a spacing between adjacent slots of $\lambda_g/2$, where $\lambda_g$ is the guide wavelength. The guide is terminated in a short circuit a distance of $\lambda_g/4$ from the last slot or an odd multiple of this distance. The geometry of the array is shown in Figure 9. Adjacent slots in the array are offset on opposite sides of the centerline in order for the slots to be excited in phase for the slot spacing of $\lambda_g/2$.

The equivalent circuit of the resonant array is shown in Figure 9. If each slot is cut to its resonant length, its equivalent circuit is a shunt conductance in the waveguide equivalent circuit. The short circuit termination in the waveguide transforms into an open circuit at the position of the last slot. Since the slots are spaced $\lambda_g/2$ apart, the equivalent circuit reduces to a single normalized shunt conductance $g_e$ given by

$$g_e = 2 \sum_{i=1}^{5} g_i \tag{4-10}$$
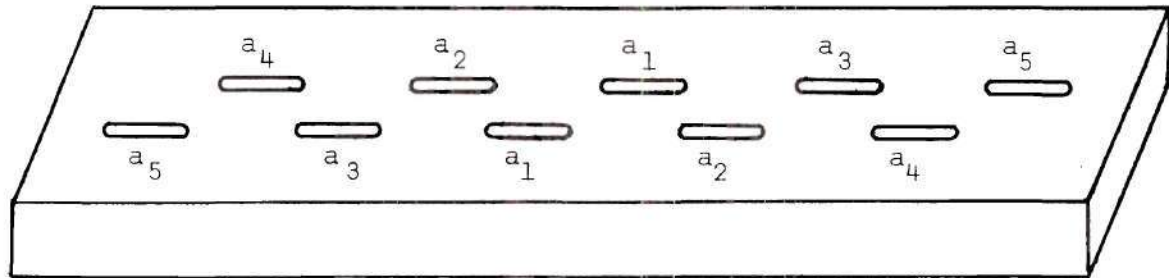
(a)
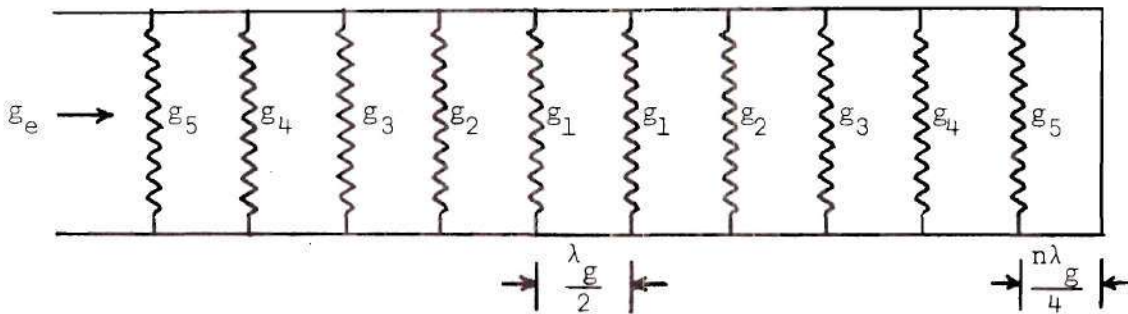


(b)

Figure 9.  The Resonant Array and Its Equivalent Circuit

where $g_i$ is the normalized conductance of the $i th$ slot from the center of the array.

The slot conductances are related to the slot excitation coefficients by

$$g_i = K a_i^2 \qquad (4\text{-}11)$$

where K is a normalization constant. In order for the slot array to be matched to the input guide, K is chosen so that $g_e = 1$. In this case, the normalized slot conductances $g_i$ are given by

$$g_i = \frac{a_i^2}{2 \sum_{i=1}^{5} a_i^2} \qquad (4\text{-}12)$$

The theoretical variation of the conductance of a resonant slot with offset distance x is given by

$$g = g_o \sin^2 \frac{\pi x}{a} \qquad (4\text{-}13)$$

where $a$ is the internal width of the waveguide. Jasik (35) gives extensive graphical data for the normalized slot conductance g as a function of the offset distance x at the frequency 9.375 GHz. A curve-fitting technique was used to fit Equation (4-13) to these data over the range of the slot conductances calculated from Equation (4-12). The resulting equation for the offset distance x as a function of slot conductance g was found to be

$$x_i = \frac{a}{\pi} \sin^{-1} \left[ \frac{g_i}{1.191} \right]^{\frac{1}{2}} \qquad (4\text{-}14)$$

The slotted waveguide array was designed by using Equation (4-14) to obtain the required offset distance for each slot from the conductances $g_i$ given by Equation (4-12). Once the offset distances were determined, the resonant slot lengths $L_i$ were obtained for the offset distances $x_i$ from the graphical data given by Jasik (35).

The array of slots was cut in the broadwall of a 17.2-inch length of WR-90 waveguide with a numerically controlled milling machine to an accuracy of 0.001 inch. The generator end of the array was terminated in a waveguide flange connected to a Type N coaxial-to-waveguide connector. The load end was terminated with an adjustable short which was set for a minimum input VSWR at a frequency of 9.68 GHz, the frequency at which the measurements were made. The antenna design is summarized in Figure 10.

### 4.3 The Near-Field Measurement System

The near-field measurements for the experimental phase of the research were made on the indoor near-field antenna range at Georgia Tech. Since this facility was designed for near-field measurements on a plane in front of a test antenna, the range had to be modified for the cylindrical measurement surface. This modification consisted of the installation of a rotating platform in front of the planar measurement surface on which the test antenna was mounted. The modified near-field range and the associated data acquisition equipment are described in this section.
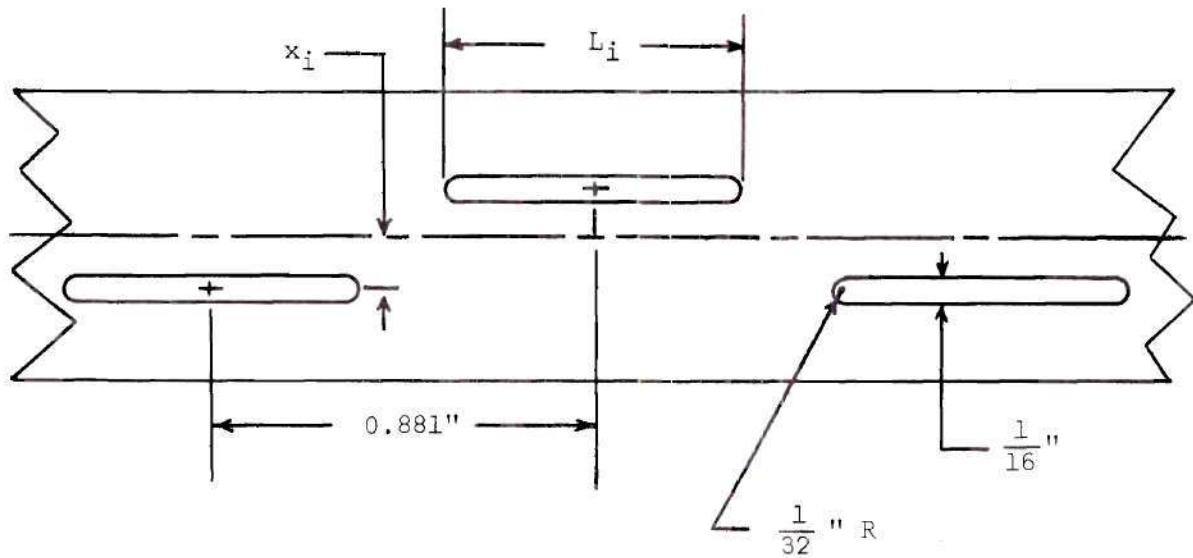
| i | $a_i$ | $g_i$ | $x_i$ (in.) | $L_i$ (in.) |
|---|-------|-------|-------------|-------------|
| 1 | 1.271 | 0.155 | 0.106 | 0.489 |
| 2 | 1.171 | 0.132 | 0.097 | 0.488 |
| 3 | 0.988 | 0.094 | 0.082 | 0.487 |
| 4 | 0.755 | 0.055 | 0.062 | 0.485 |
| 5 | 0.815 | 0.064 | 0.067 | 0.485 |

Figure 10.  Summary of the Slot Array Design

A diagram of the near-field measurement system is shown in Figure 11. The RF signal applied to the test antenna was generated by a Varian X-13 klystron operating at a frequency of 9.68 GHz. The klystron was powered by a NARDA Model 438 klystron power supply. Its output was phase-locked to a crystal frequency reference with a FEL Model 133-AK klystron frequency synchronizer. The synchronizer was specified to maintain a klystron frequency stability of one part in $10^6$ for long-term operation. A Microlab/FXB Model X4105 absorption frequency meter connected to a Hewlett Packard Model 413C power meter was used to initially adjust the klystron to operate at 9.68 GHz. The power meter was subsequently used to monitor the klystron output level during the course of the measurements.

The test antenna was mounted on a wooden support which was securely bolted to the rotating platform of a Scientific-Atlanta Model 5103-1-L antenna positioner. The output signal from the klystron was coupled to the test antenna through a RF rotary joint in the base of the antenna positioner with RG 214U coaxial cable. The cable was securely taped to the floor and to the antenna mount to prevent phase errors from cable movement.

The antenna positioner was mounted on top of the linear motion platform of a Scientific-Atlanta Model K243 near-zone positioning system. The axis of rotation of the rotating platform on the antenna positioner defined the vertical axis of the measurement cylinder. The radius of the measurement cylinder could be adjusted by varying the position of the linear motion platform with respect to the probe.
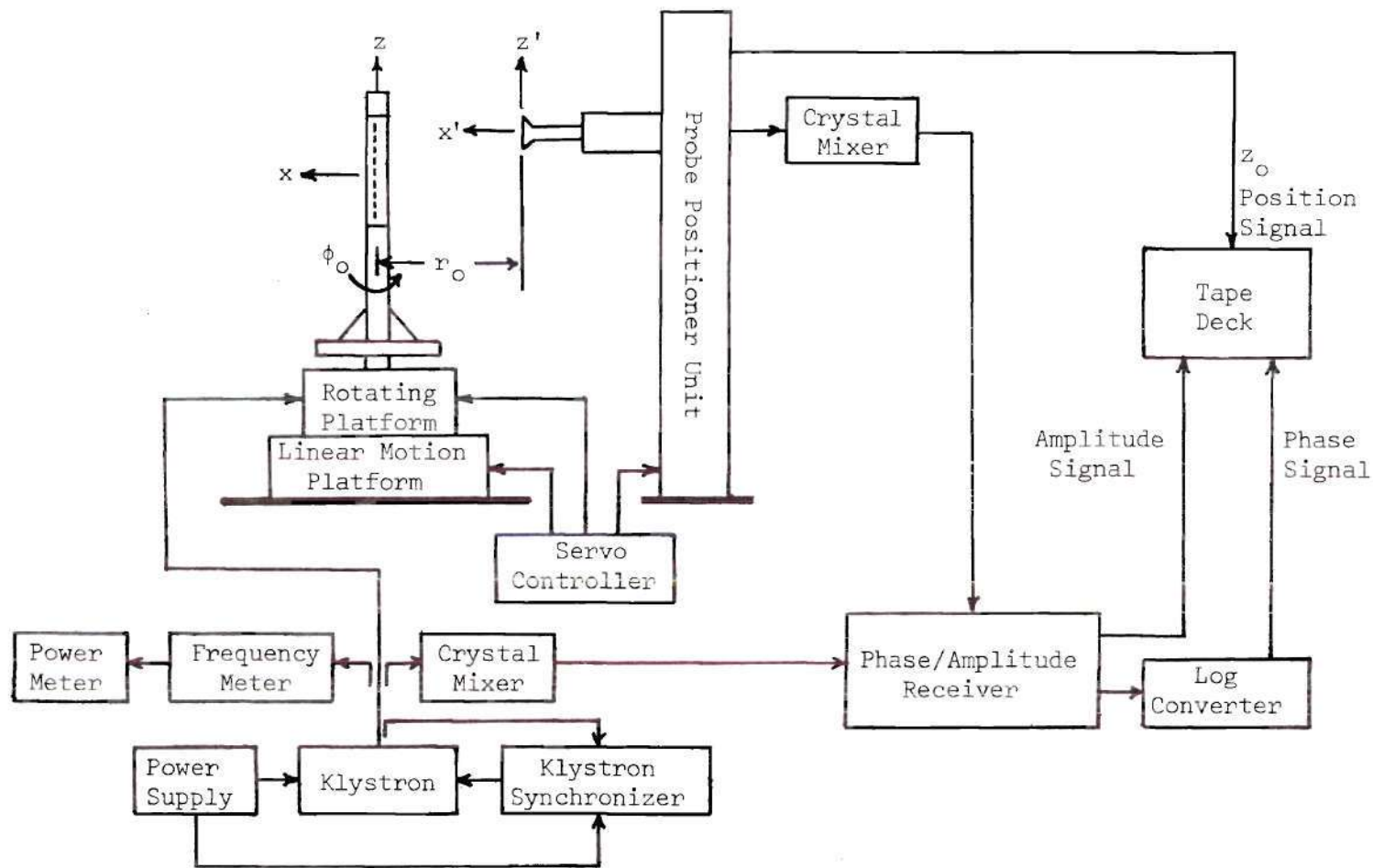
Figure 11.  Diagram of the Near-Field Measurement System

The probe antenna was mounted on the rotary probe carriage of the near-zone positioning system. The probe carriage position was servo-controlled and could be remotely positioned to any point on a 100 by 100 inch vertical plane. A mechanical scissor unit connected the probe carriage to a stationary point on the frame on the near-zone positioning system with RG-214U coaxial cable and three rotary joints. This arrangement permitted the positioning of the probe to any point on the 100 by 100 inch plane without changing the amplitude or phase properties of the signal path. The probe carriage, the linear motion platform, and the test antenna positioner were remotely controlled with a Scientific-Atlanta Series 4100 positioner control unit.

The rotary probe carriage permitted rotating the probe about its longitudinal axis so that two independent measurements could be made on the measurement cylinder. The output of the probe was connected through a RF rotary joint at the rear of the probe carriage to permit rotating the probe without flexing the signal cable.

The probe was initially positioned on the measurement cylinder by adjusting its horizontal position until the longitudinal axis of the probe intersected the vertical axis of rotation of the rotating plat-form. The vertical motion capability of the probe was then used to position it vertically on the cylinder. The azimuth position of the probe on the cylinder was controlled by rotating the test antenna by rotating the platform on which it was mounted.

The metal frame of the near-zone positioning system and the wall directly behind the frame were covered with microwave absorbing material.

In addition, absorbing material was placed over the klystron and its associated hardware to minimize stray radiation. Although the supply of additional absorbing material was limited, all metalic objects in the vicinity of the near-field range which could not be moved were covered with absorber.

The output signal from the probe was connected to the signal input of a Scientific-Atlanta Model 1750 phase amplitude receiver through RG 214U coaxial cable. The cable was securely taped along its length to prevent flexing. The phase reference signal for the receiver was obtained from the output of a directional coupler which was connected in series with the klystron output. This signal was connected to the receiver through securely taped RG 58 C/U coaxial cable.

Above 4.1 GHz, the Scientific-Atlanta Model 1750 receiver employs externally mounted harmonic crystal mixers to heterodyne the input signals to a 45 MHz first intermediate frequency. The local oscillator for the crystal mixers operates in the 2.0-4.1 GHz band. It is advantageous to mount the crystal mixers as close as possible to the signal sources so that the highest frequency signal transmitted through the RF signal cable and rotary joints is the local oscillator signal. The crystal mixer for the signal output from the probe was mounted directly to the waveguide to Type N coaxial connector which terminated the probe waveguide feeder. This mixer was a Scientific-Atlanta Model 14 A-2 coaxial mixer. The crystal mixer for the reference channel of the receiver was mounted at the output of the directional coupler from which the reference signal was obtained. This mixer was a Scientific-Atlanta Model 13-8.2 waveguide mixer with a BNC output connector.

The near-field data were recorded on a seven-channel Honeywell Model 5600 tape recorder. The data consisted of four signals: the probe amplitude signal, the probe phase signal, a probe position signal, and a voice annotation signal. In order to have a response to d.c., the first three signals were recorded utilizing the FM electronics in the tape deck. The voice annotation signal was recorded through the analog electronics in the tape deck.

The probe amplitude signal at the output of the Scientific-Atlanta receiver was a 1000 Hz linear a.c. signal with a dynamic range of 60 dB. This signal was rectified and converted to a logarithmic d.c. analog signal with a Scientific-Atlanta Model 1831 synchronous rectifier and logarithmic converter before it was recorded on the tape deck. The logarithmic compression allowed recording the amplitude signal at levels well above the noise level of the tape deck which was 41 dB below the reference level of one volt r.m.s. The probe phase signal at the output of the receiver was a d.c. analog signal which was recorded directly on the tape.

The near-field measurements were taken by holding the azimuth angle $\phi_o$ of the test antenna constant while moving the probe at constant velocity up the measurement cylinder and simultaneously recording the receiver outputs. The azimuth angle was then incremented and the process repeated until the complete cylinder had been covered. In order to know the $z_o$ position of the probe on the measurement cylinder when the recorded data were read from the tape, it was necessary to record a probe position signal. This signal was a one-volt d.c. signal obtained from

a microswitch mounted on the rear of the probe carriage and connected in series with a d.c. voltage source. The microswitch was mounted so that it was activated only when the probe carriage was moving vertically past a 52.1-inch narrow aluminum plate which was mounted on the rear of the probe positioner frame. The length of the plate was chosen to be 128 one-third wavelengths at 9.68 GHz. The plate was positioned so that the microswitch roller was at its center when the probe was centered vertically on the antenna.

## 4.4   The Far-Field Measurement System

The far-field patterns of the test antenna were measured on the indoor phase-center range at Georgia Tech. The phase-center range consists of a rotating boom on which a receiving antenna can be mounted and rotated on a circle of radius 12 feet or less around a stationary transmitting antenna. A RF rotary joint in the rotating platform on which the boom is mounted permits accurate determination of the phase and amplitude of the received signal as the boom is rotated. A diagram of this facility is shown in Figure 12.

The test antenna was mounted on top of a linear motion platform which was mounted on a stationary frame above the rotating platform of a Scientific-Atlanta Model 5103-1-L antenna positioner. The linear motion platform could be adjusted with two degrees of freedom in the horizontal plane so as to make the phase center of the test antenna coincide with the vertical axis of rotation of the rotating platform beneath. A horizontal boom of approximately 12 feet in length was bolted at one end to the rotating platform of the antenna positioner.

To Klystron Output

Test Antenna

Styrofoam Support

Linear Motion Platform

Receiving Horn

Rotating Boom

Rotating Platform

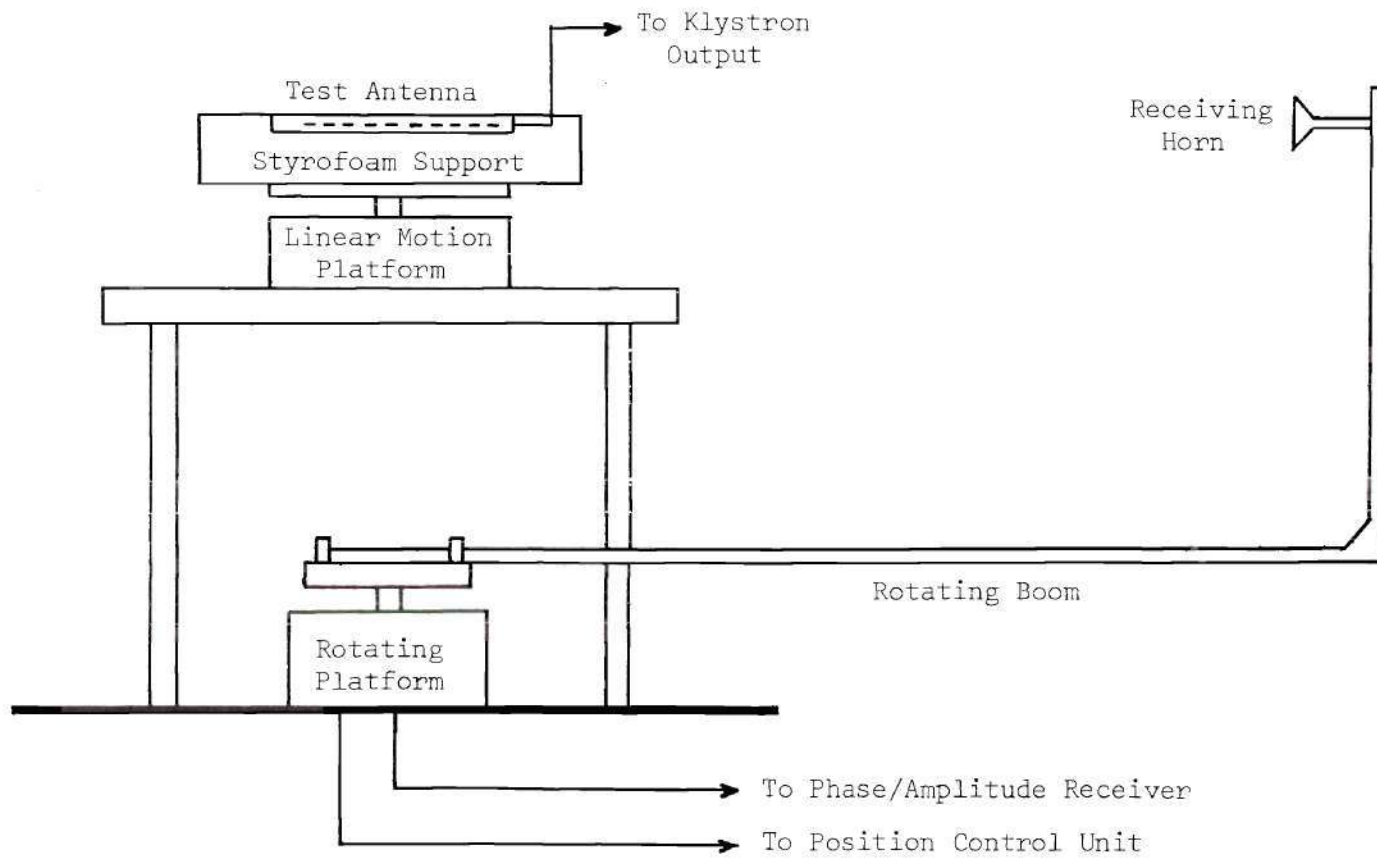To Phase/Amplitude Receiver

To Position Control Unit

Figure 12.  Diagram of the Phase Center Range

At the end of the boom, a NARDA Model 640 standard gain horn, which was used as a receiving antenna, was mounted on a vertical beam to the same height as the test antenna. The output flange of the receiving horn was terminated in a Scientific-Atlanta Model 13-8.2 waveguide crystal mixer with a BNC output connector. The output of the mixer was connected to the RF rotary joint in the base of the antenna positioner with RG 58 C/U coaxial cable. The cable was taped along its length to the boom to prevent flexing.

The klystron, its associated equipment, and the phase/amplitude receiver described in Section 4.4 were used with the phase center range to measure the far-field patterns of the test antenna. The output signal from the klystron was connected to the test antenna with RG 214U coaxial cable. The output of the RF rotary joint in the base of the antenna positioner was connected to the input of the receiver with the same cable. The far-field patterns were recorded on a Scientific-Atlanta Series 1540 antenna pattern recorder as the receiving antenna was rotated on the boom around the test antenna. The boom position was remotely controlled with a Scientific-Atlanta Series 4100 positioner control unit.

# CHAPTER V

## THE EXPERIMENTAL RESULTS

### 5.1  Introduction

The work performed for the experimental part of the research is described in this chapter.  The near field of the test antenna was measured for four different cases.  In the first case, the antenna was centered vertically in the measurement cylinder and the near field was measured with the open-end waveguide probe.  In the second case, the antenna was translated a distance of $\lambda/2$ from the center of the cylinder and the near field was again measured with the open-end waveguide probe. In the third case, the small horn probe was used to measure the near field with the antenna centered vertically in the cylinder.  In the fourth case, the antenna was centered horizontally in the cylinder and the near-field was measured with the open-end waveguide probe.  Since the elevation pattern of the test antenna in the latter case was so broad, the near field was measured only on a circle around the antenna. Amplitude and phase plots of the measured near-field data are presented for each of the four cases in Section 5.2.

The principal plane elevation and azimuth far-field patterns of the test antenna were measured for comparison with the patterns calculated from the near-field data.  The measured far-field patterns are presented in Section 5.3.

The far-field patterns of the test antenna were calculated for each of the four near-field measurement cases. The calculated patterns are presented in Section 5.4 where they are compared to the measured far-field patterns.

## 5.2   The Near-Field Measurements--Four Cases

The near field of the test antenna was measured on a cylinder of radius 12 inches containing the antenna. Before the measurements were made, the near-zone positioning system was aligned to ensure that the axis of the cylinder was vertical, that the probe moved on a vertical line up the cylinder, and that the perpendicular distance from the center of the probe aperture to the axis of the cylinder was 12 inches. The alignment procedure was repeated before each of the four near-field measurement cases.

To vertically align the axis of the measurement cylinder, a precision level was placed on the rotating platform in Figure 11 on which the test antenna was to be mounted. The platform was then slowly rotated while observing the bubble in the precision level. The adjustable feet under the linear motion platform on which the rotating platform was mounted were then adjusted to minimize the deviation of the bubble as the platform was rotated. With this procedure, it was possible to align the vertical axis of the cylinder so that it did not deviate by more than 40 seconds of arc as the platform was rotated. This deviation was caused by the bearings in the rotating platform and could not be eliminated.

In order to align the probe positioning system so that the probe moved in a vertical line up the measurement cylinder, a plumb bob was suspended from the end of the probe so that it hung over the crossed lines of a sheet of graph paper. The adjustable feet in the base of the probe positioning system were then adjusted until the plumb bob hung over the same position on the graph paper when the probe was positioned vertically to both the top and bottom of the measurement cylinder.

The radius of the measurement cylinder was set to 12 inches by first clamping a jig to the top of the probe that extended 12 inches out from its aperture. The probe was then positioned vertically to the center of the measurement cylinder, and a plumb bob was suspended from the end of the jig. The plumb bob hung over the crossed lines of a sheet of graph paper attached to the top of the rotating platform on which the test antenna was to be mounted. The horizontal position of the probe and the linear motion platform in Figure 11 on which the rotating platform was mounted were then adjusted until the plumb bob hung over the same point on the graph paper when the rotating platform was rotated through a full revolution.

The first three measurements were taken with the antenna mounted vertically in the measurement cylinder. The cylinder was divided into 32 vertical scans of the probe, each separated by 11.25° in the azimuth angle $\phi_o$. For each measurement, the horizontal component of the electric field intensity was first measured over the complete cylinder. The probe was then rotated 90° about its longitudinal axis and the process was repeated for the vertical component of the electric field intensity

on the cylinder. For each vertical scan, the probe was first positioned vertically to a point below the lower end of the measurement cylinder. The tape deck on which the data were recorded and the probe servo-motor were then started simultaneously, and the data were recorded as the probe moved up the measurement cylinder at a constant velocity. At the end of the scan, the tape deck was stopped and the probe was returned to its lower position before the next scan. Each vertical scan took approximately 30-35 seconds.

The fourth measurement was made with the antenna mounted horizontally in the measurement cylinder. In this case, the elevation pattern of the antenna was so broad that there was little change in amplitude of the probe output as it was moved vertically on the measurement cylinder. The near field of the antenna in this case was measured only on a circle around the antenna. Both the vertical and horizontal components of the near-field electric field intensity were measured on the circle.

The analog near-field data for each of the first three measurement cases occupied a full reel of 10-inch magnetic tape recorded at $7\frac{1}{2}$ inches per second. The fourth measurement required only a small fraction of one reel. These data were converted to digital form on a Radiation Inc. Model 5020 analog to digital converter. Calibration signals for the conversion were recorded at the beginning of each tape for both the amplitude channel and the phase channel. To reduce the playback time during the data conversion, the playback tape deck was operated at a speed of 15 inches per second. After the data conversion was

completed, the digital tapes were processed to obtain 128 equally-spaced samples from each vertical scan of the first three measurement cases. For the fourth measurement, the data were processed to obtain 1024 equally-spaced samples around the measurement circle.

The near-field data for the first three measurement cases are displayed in Figures 13 through 18. The data for the first two cases were measured with the open-end waveguide probe. In the first of these, the antenna was mounted vertically at approximately the center of the measurement cylinder. In the second, the antenna was translated horizontally a distance of approximately $\lambda/2$ from the position of the first measurement. The third measurement was made with the small horn probe. The antenna was mounted vertically at approximately the center of the measurement cylinder as in measurement case one.

The base coordinates in the three-dimensional plots of Figures 13 through 18 are the azimuth angle $\phi_o$ and height $z_o$ on the measurement cylinder, where $-180° \le \phi_o < +180°$ and $-26.05'' \le z_o \le 26.05''$. In these figures, the amplitude plots are normalized so that they are in the range of 0 to -40 dB. The phase plots are for a phase angle between -180° and +180°. A comparison of the amplitude plot for measurement case three to those of cases one and two reveals the effect of the more directive small horn probe on the measured data. The measured near-field amplitude tapers off much more rapidly toward the ends of the measurement cylinder than the amplitude measured with the open-end waveguide probe.
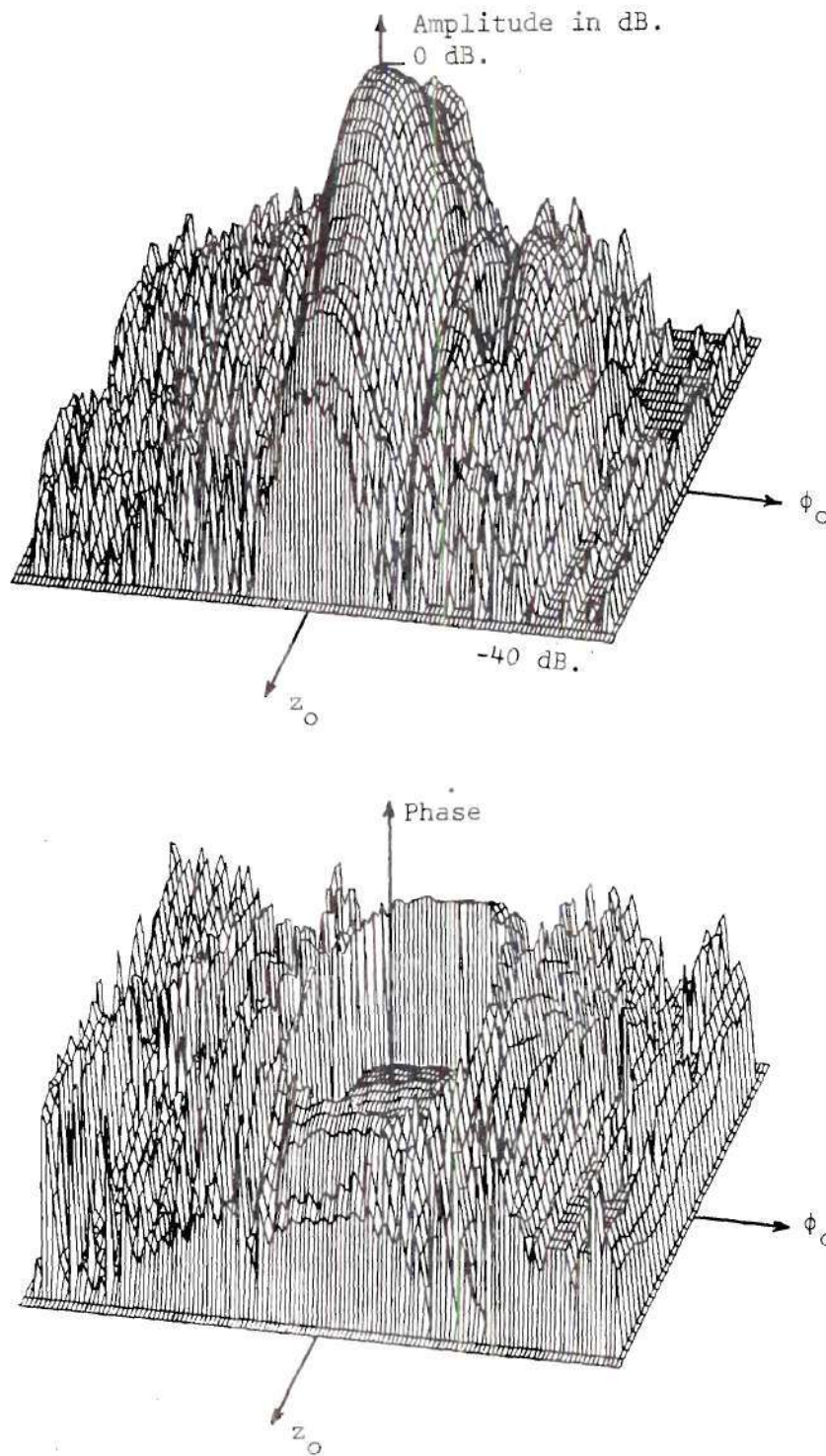
Figure 13.   Near-Field Amplitude and Phase Patterns of $E_\phi$ for Measurement Case One, Measured with the Open-End Waveguide Probe with the Antenna Mounted Vertically in the Cylinder
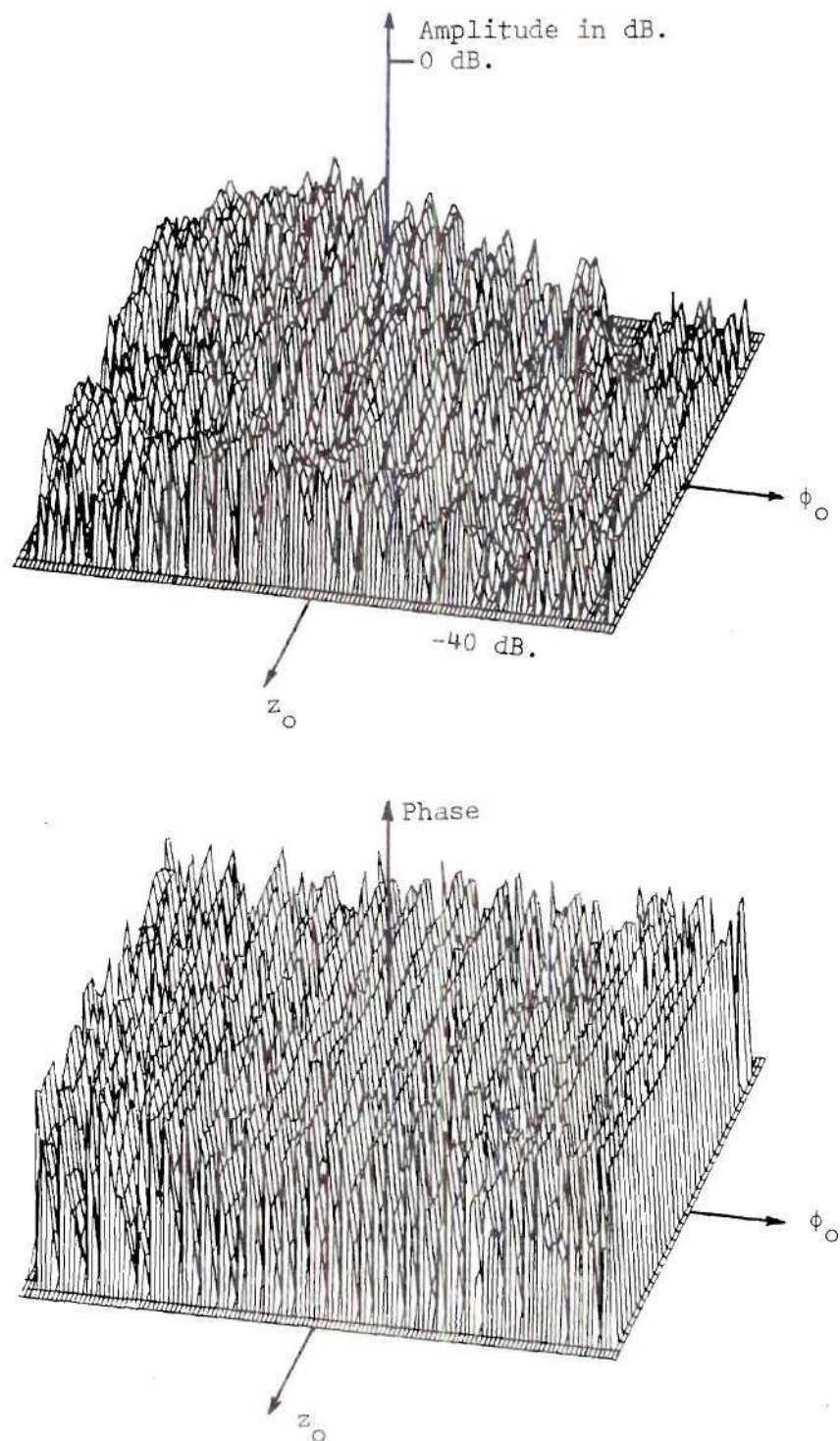
Figure 14. Near-Field Amplitude and Phase Patterns of $E_z$ for Measurement Case One, Measured with the Open-End Waveguide Probe with the Antenna Mounted Vertically in the Cylinder
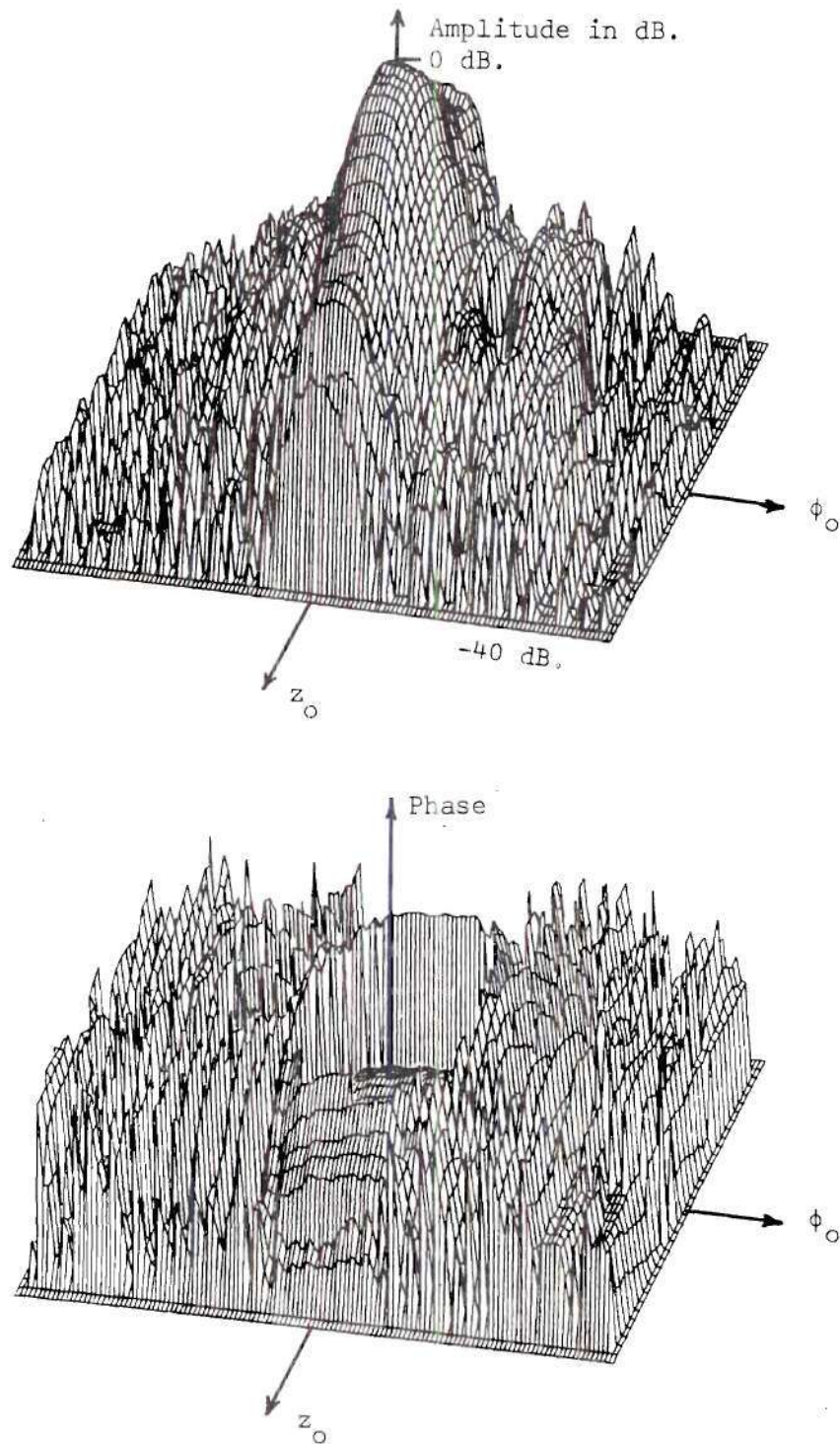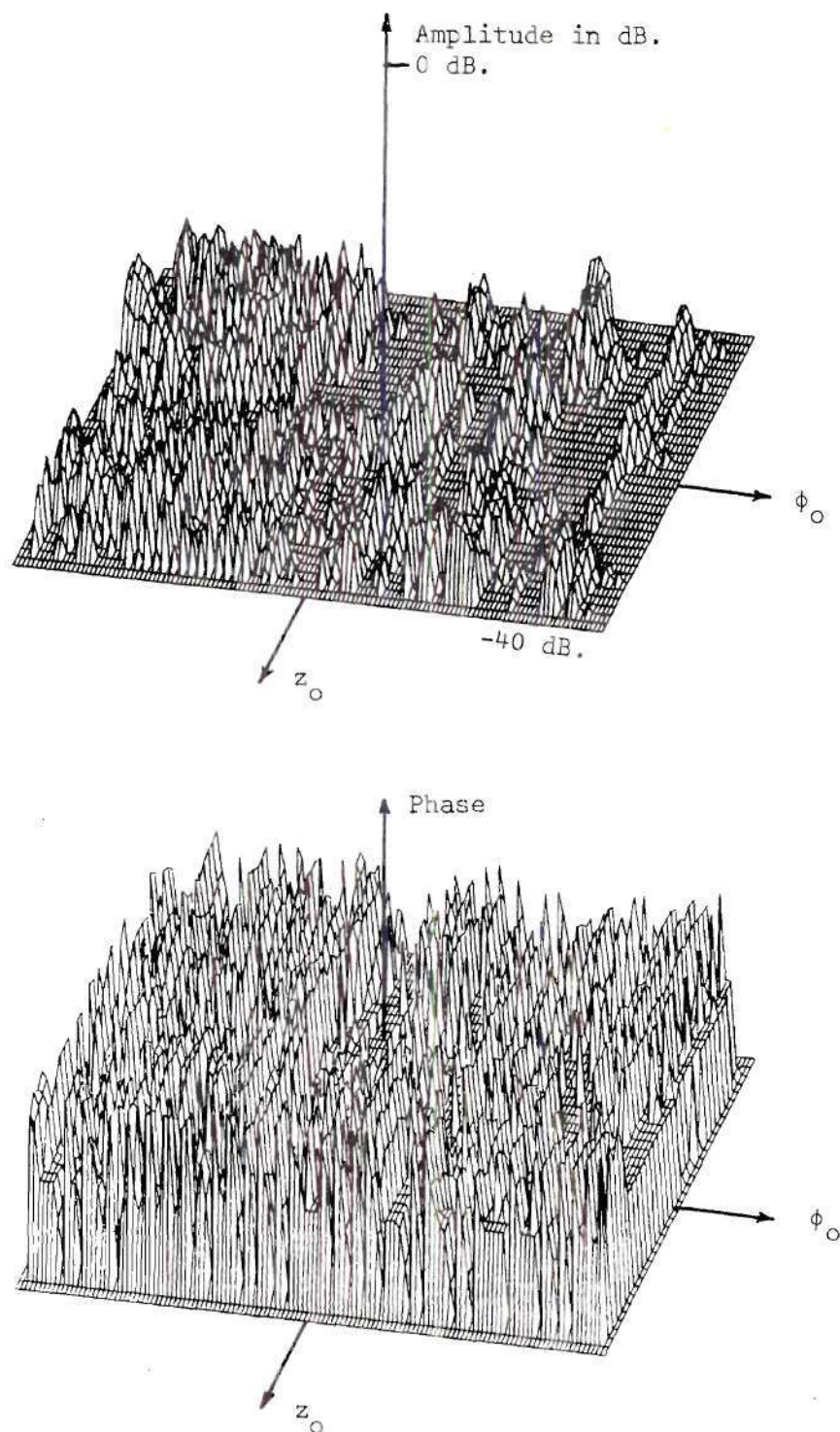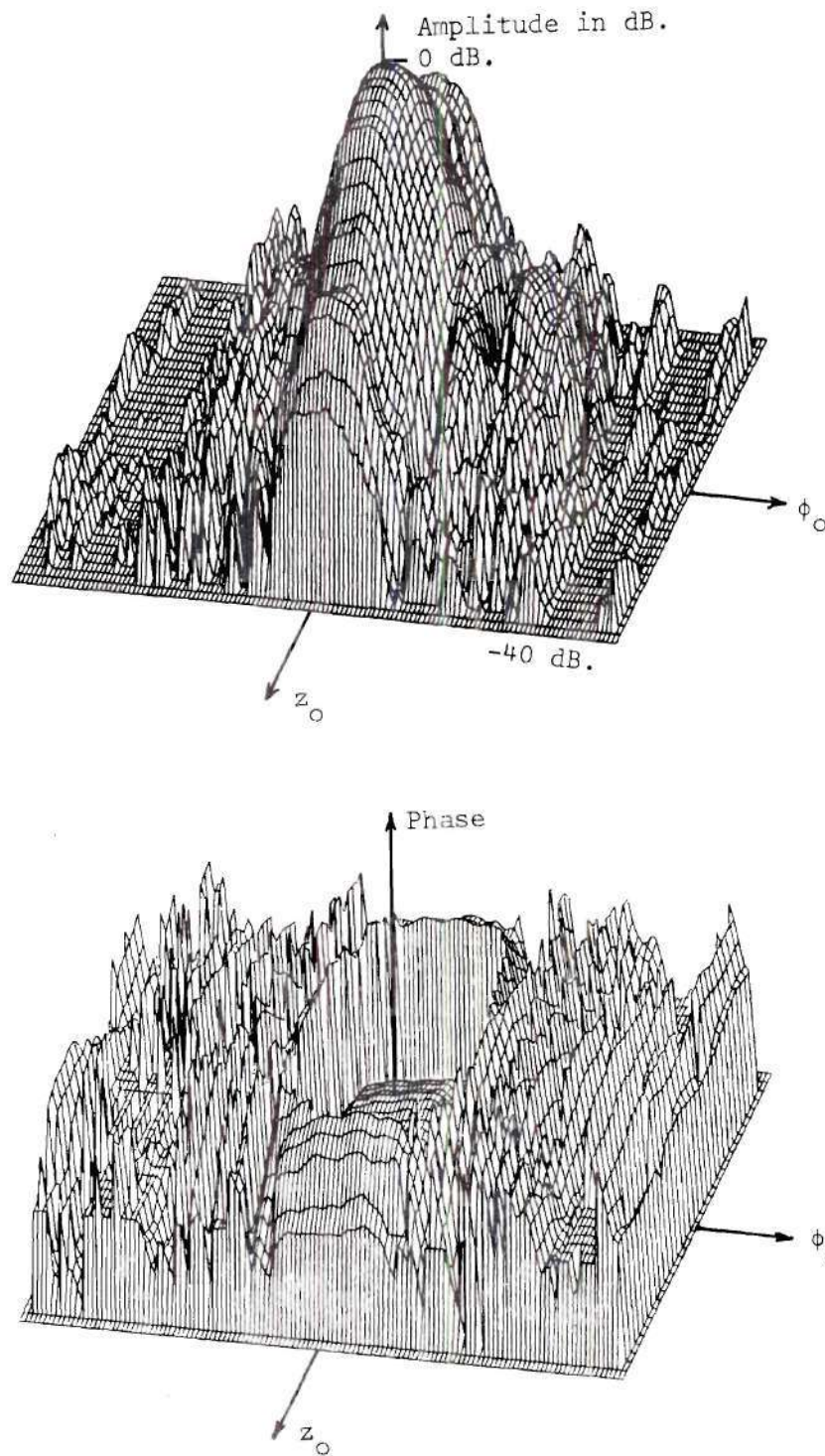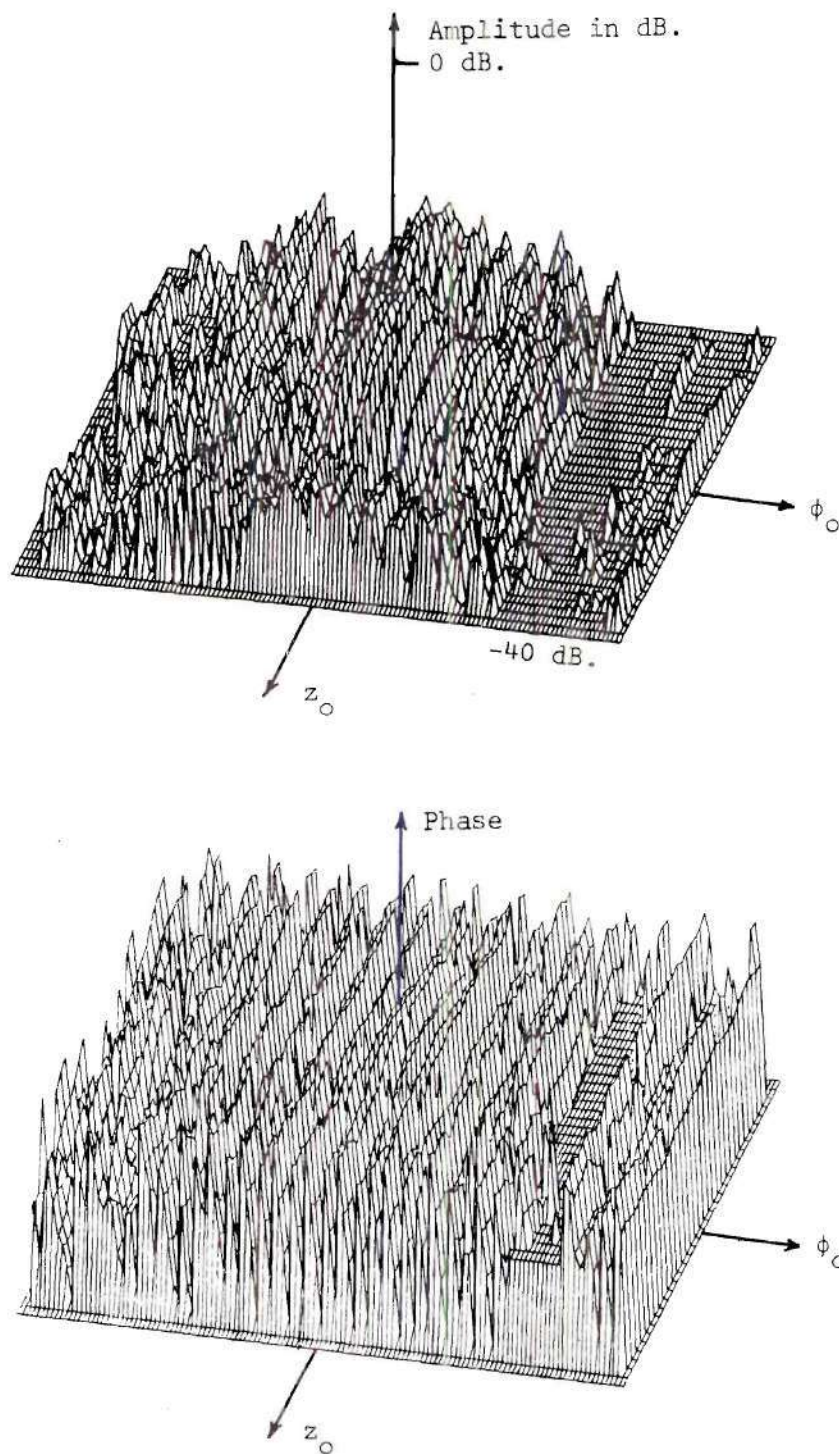
Figure 15. Near-Field Amplitude and Phase Patterns of $E_\phi$ for Measurement Case Two, Measured with the Open-End Waveguide Probe with the Antenna Mounted Vertically in the Cylinder

Figure 16.  Near-Field Amplitude and Phase Patterns of $E_z$
for Measurement Case Two, Measured with the
Open-End Waveguide Probe with the Test Antenna
Mounted Vertically in the Cylinder

Figure 17.  Near-Field Amplitude and Phase Patterns of $E_\phi$ for Measurement Case Three, Measured with the Small Horn Probe with the Test Antenna Mounted Vertically in the Cylinder

Figure 18. Near-Field Amplitude and Phase Patterns of $E_z$ for Measurement Case Three, Measured with the Small Horn Probe with the Test Antenna Mounted Vertically in the Cylinder

The near-field data for measurement case four are displayed in the plots of Figures 19 and 20. The antenna was mounted horizontally in this case, and the near field on the circle was measured with the open-end waveguide probe.

## 5.3   The Far-Field Measurements

The far-field patterns of the test antenna were measured on the phase center range described in Section 4.4. The antenna was mounted on a styrofoam support on top of the linear motion platform shown in Figure 12. For each pattern the platform was adjusted to reasonably center the antenna over the center of rotation of the rotating boom which supported the receiving horn. Absorbing material was placed over the klystron source and its associated hardware to minimize the effects of stray radiation.

To obtain the elevation pattern, the test antenna was mounted horizontally on the linear motion platform. The boom on which the receiving antenna was mounted was then rotated over a 180° arc to record the far-field vertical elevation pattern for $0 \leq \theta \leq 180°$. This measured pattern is displayed in Figure 21 over the interval $30° \leq \theta \leq 150°$. This pattern represents the elevation pattern of the far-field $\phi$-component of the electric field intensity radiated by the test antenna when it is mounted vertically. The small irregularities in this pattern were caused by reflections and stray radiation in the room. The cross polarization component radiated by the antenna was so low in amplitude that it was not measured.
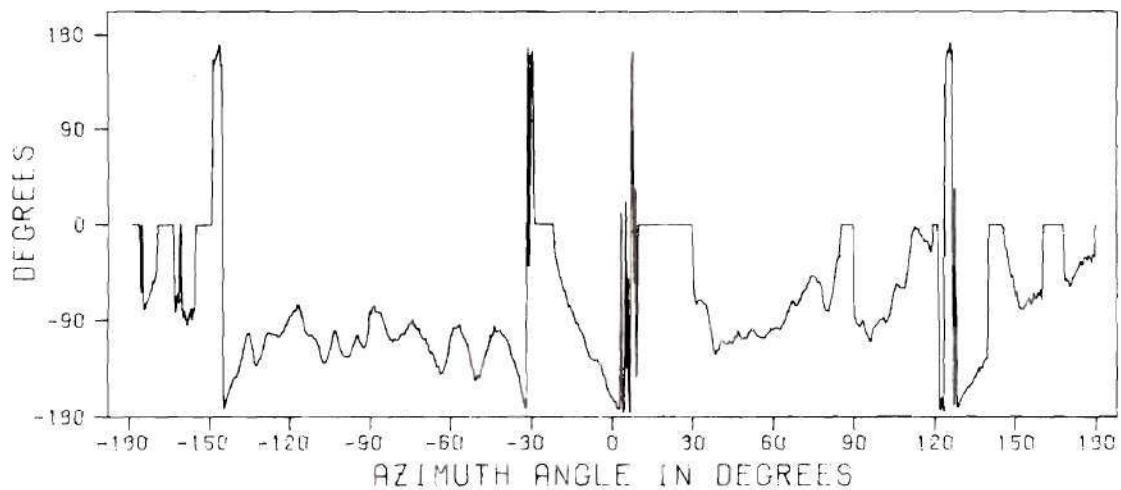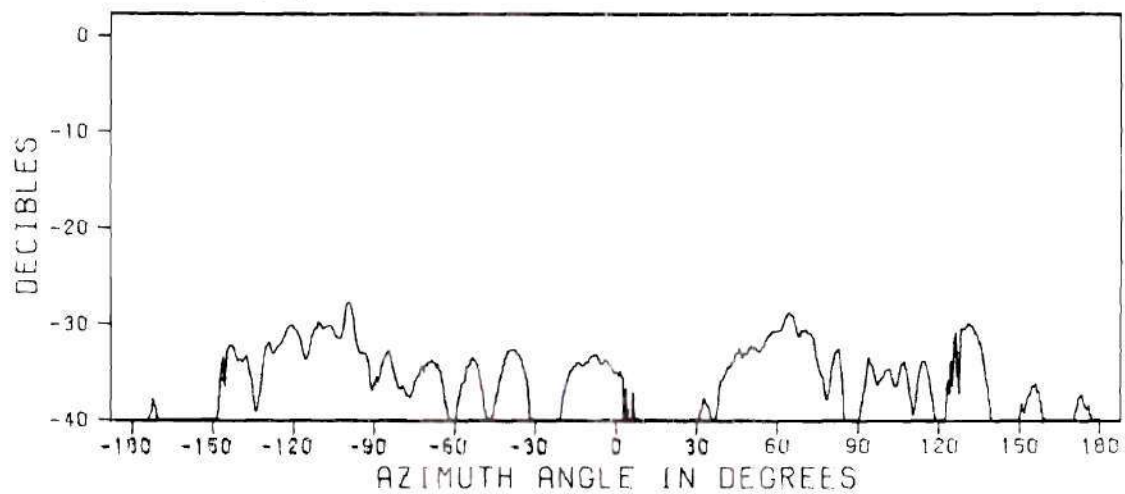
Figure 19. Near-Field Amplitude and Phase Patterns of $E_\phi$ for Measurement Case Four, Measured with the Open-End Waveguide Probe with the Antenna Mounted Horizontally in the Cylinder
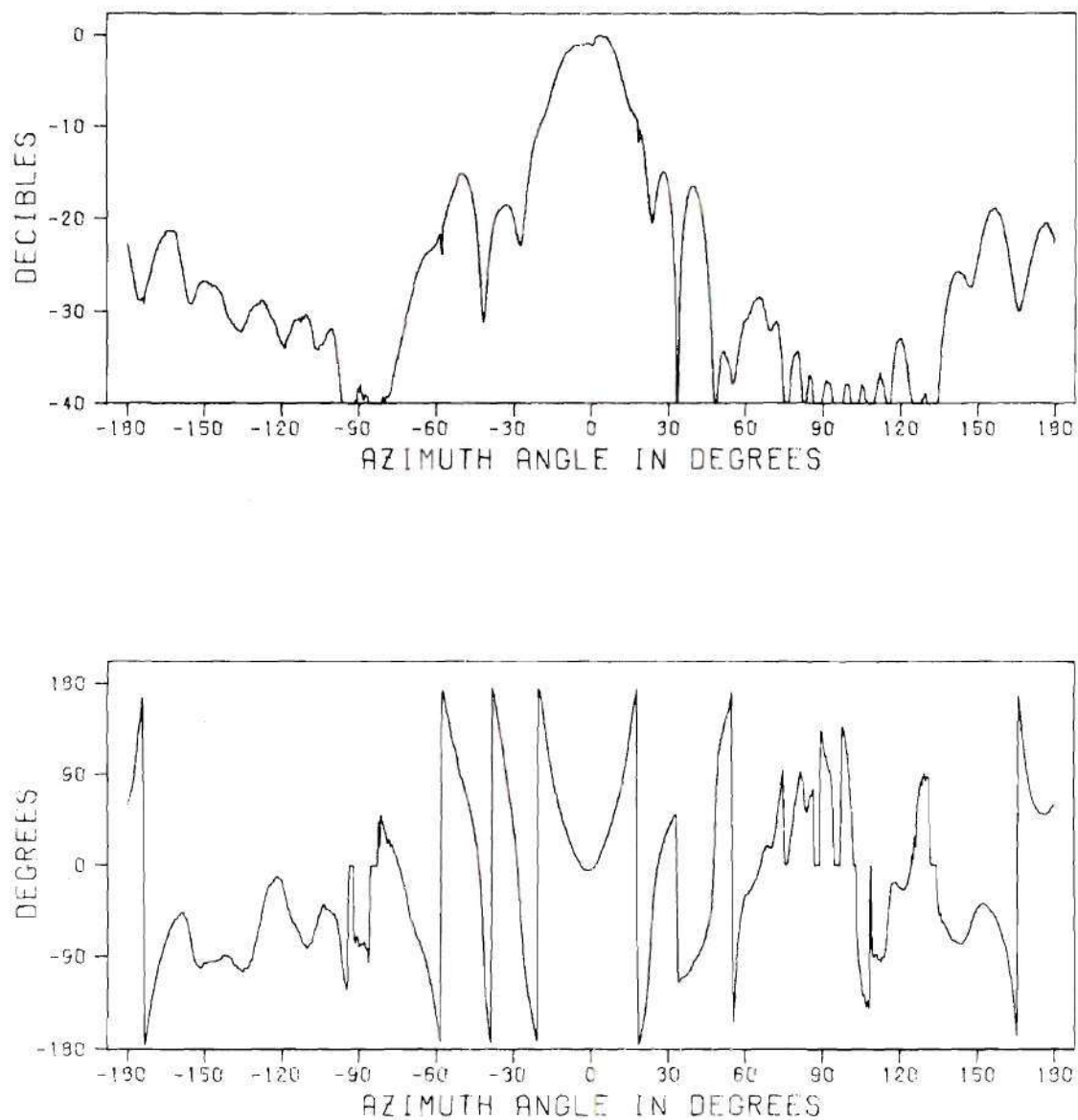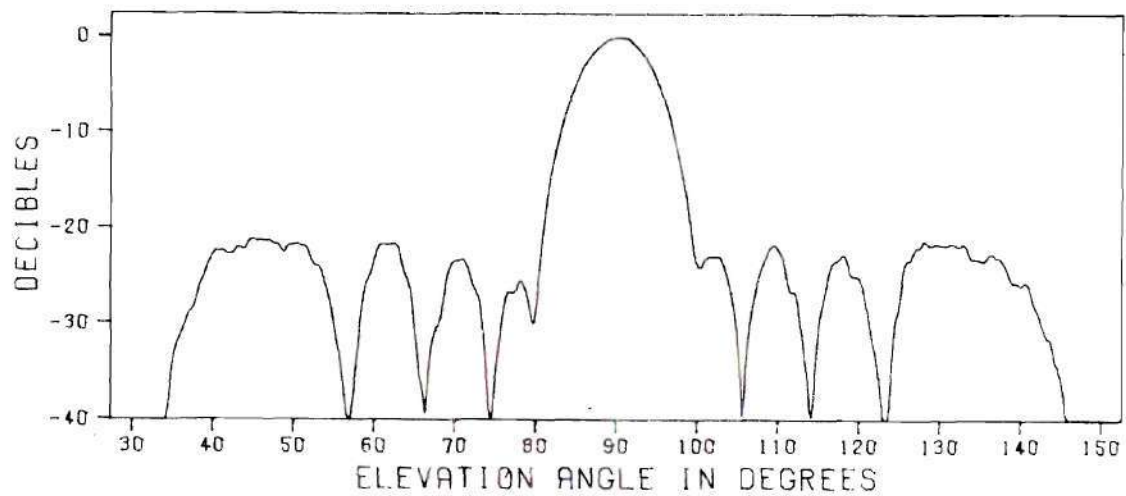
Figure 20.  Near-Field Amplitude and Phase Patterns of $E_z$
for Measurement Case Four, Measured with the
Open-End Waveguide Probe with the Antenna
Mounted Horizontally in the Cylinder

Figure 21.   The Measured Principal Plane Far-Field
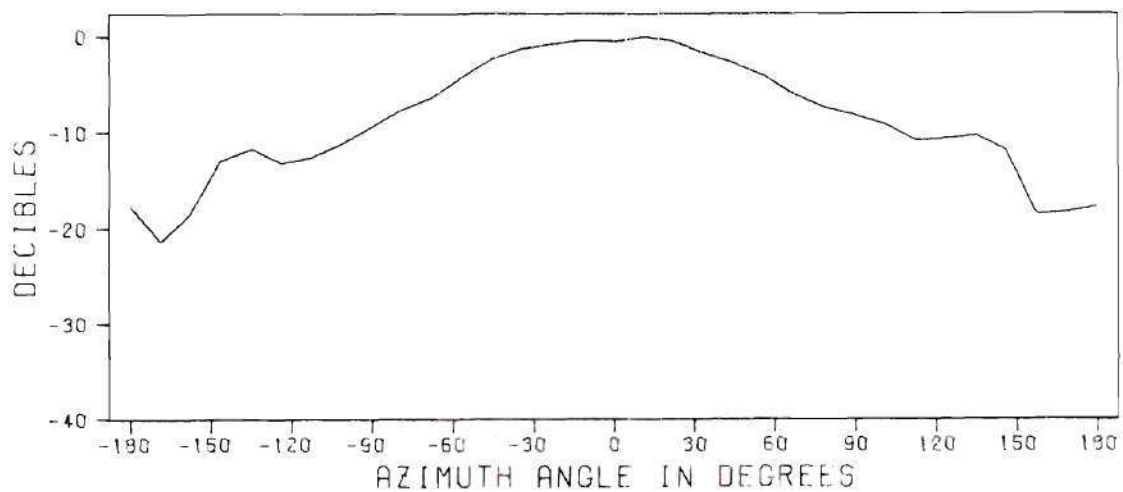Elevation Pattern of the Test Antenna



Figure 22.   The Measured Principal Plane Far-Field
Azimuth Pattern of the Test Antenna

To obtain the azimuth pattern, the antenna was mounted vertically on the linear motion platform. The boom on which the receiving antenna was mounted was then rotated to record the vertical azimuth pattern for $-90° \leq \phi \leq 90°$. To obtain the full $360°$ pattern, the antenna had to be rotated $\pm 90°$ about its longitudinal axis to separately record the pattern for $-180° \leq \phi \leq -90°$ and $90° \leq \phi \leq 180°$. The measured azimuth pattern is displayed in Figure 22. This pattern represents the azimuth pattern of the far-field $\phi$-component of the electric field intensity radiated by the antenna when it is mounted vertically.

## 5.4   The Calculated Far-Field Patterns

The far-field patterns of the test antenna have been computed for each of the four near-field measurement cases using the numerical methods developed in Section 3.2. These patterns are displayed in this section and are compared to the measured far-field patterns. Although they were calculated, the cross polarization patterns have been omitted since they were so low in amplitude that they could not be interpreted meaningfully.

The three-dimensional far-field patterns calculated for measurement cases one through three are displayed in Figures 23 through 25. The patterns represent the amplitude of the $\phi$-component of the far-field electric field intensity radiated by the antenna when it is mounted vertically. The base coordinates in these figures are the spherical azimuth angle $\phi$, where $-180° \leq \phi < 180°$, and wavenumber $h = k\cos\theta$, where $\theta$ is the spherical elevation angle and $30° < \theta \leq 150°$. The amplitudes of the patterns are normalized so that they lie in the range from 0 to

Figure 23. The Calculated Far-Field Amplitude Pattern of $E_\phi$ for Measurement Case One

Amplitude in dB.
0 dB.

$\phi$
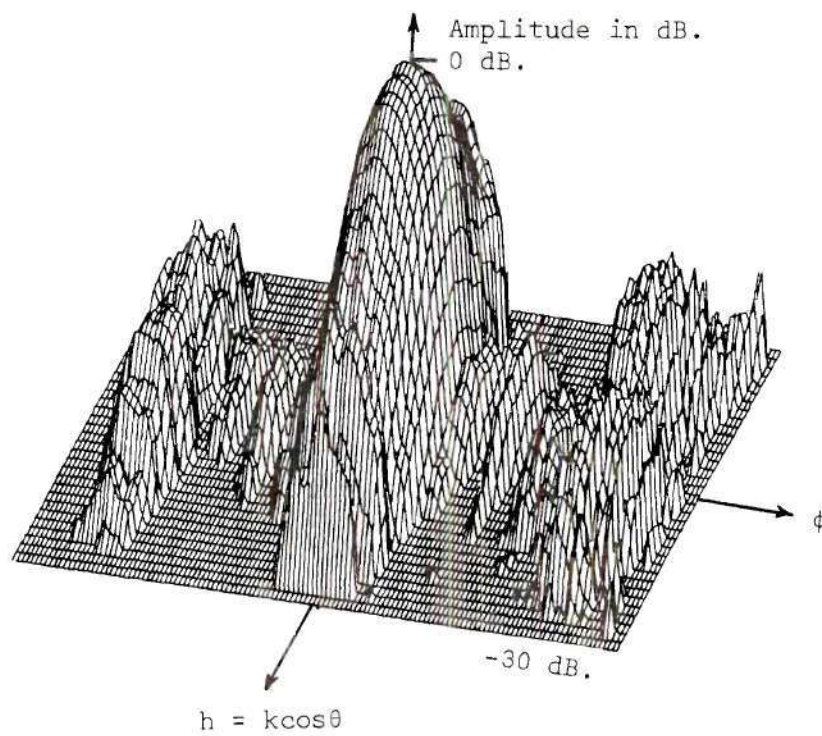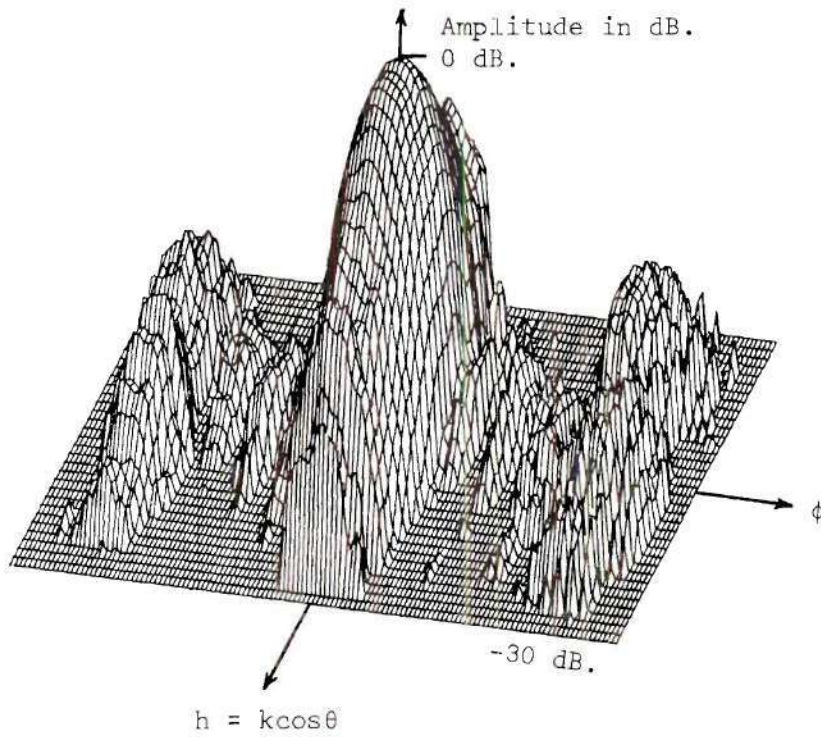
−30 dB.

h = kcos$\theta$

Figure 24.   The Calculated Far-Field Amplitude Pattern
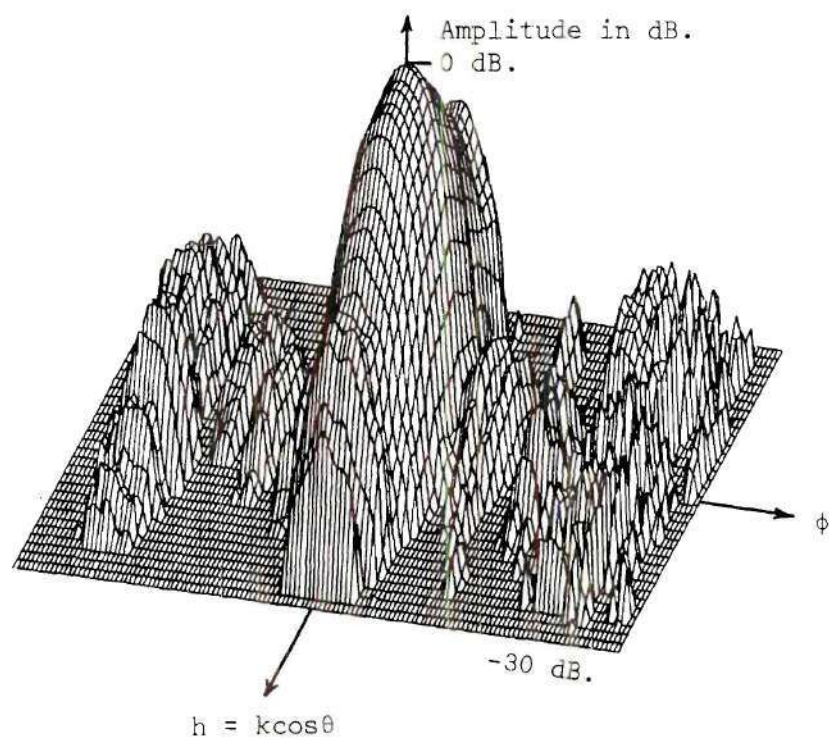of $E_\phi$ for Measurement Case Two

Figure 25. The Calculated Far-Field Amplitude Pattern of $E_\phi$ for Measurement Case Three

-30 dB. It was found that if the patterns were displayed over any wider range, they were difficult to interpret in the three-dimensional format.

The far-field pattern calculated for measurement case four is displayed in Figure 26. This pattern represents the amplitude of the $\theta$-component of the far-field electric field intensity radiated by the antenna when it is mounted horizontally. Since the near field in this case was measured only on a circle around the antenna, the elevation angle in Figure 26 is $\theta = 90°$. Thus this pattern is to be compared to the measured elevation pattern of the antenna.

The measured far-field patterns and the principal plane elevation and azimuth patterns calculated for measurement cases one through three have been plotted together for comparison in Figures 27 through 29. It is felt that Figures 27, 28(b) and 29(b) represent outstanding agreement between the measured and calculated data. The agreement in Figures 28(a) and 29(a) is not so good in the elevation angle range of $110° \leq \theta \leq 150°$. It is felt that this could have been due to stray radiation or reflections in the vicinity of the near-field range, since each measurement was performed on different days under possibly different sets of conditions.

A problem which was not anticipated was "drop outs" on the playback tape deck when the near-field data were being converted to digital form. When a "drop out" occurred, it caused an "impulse spike" in the data with an average level of 50 to 60 dB above the data amplitude. The "impulse spikes" of this level were easily located and eliminated from the data. An average of one to two were found in each near-field data
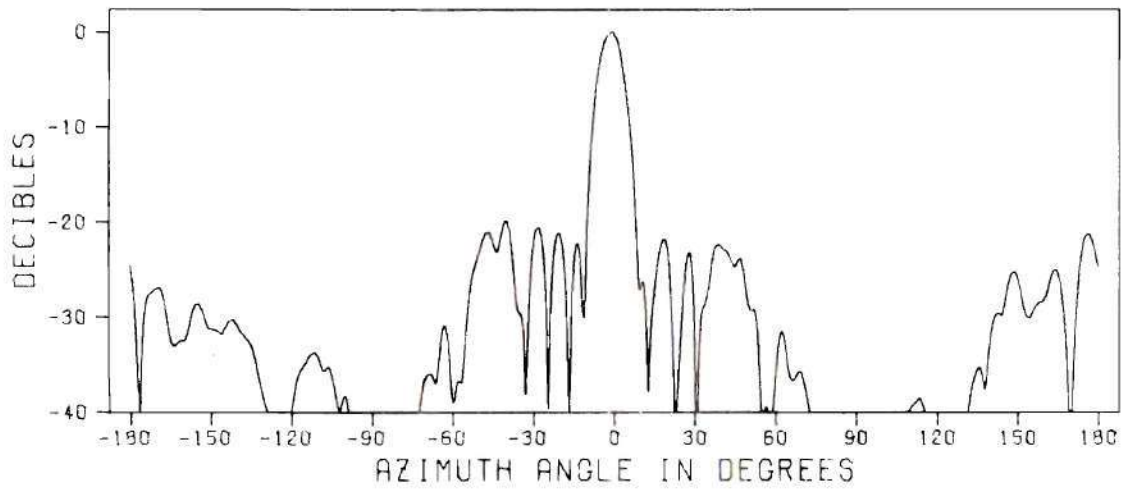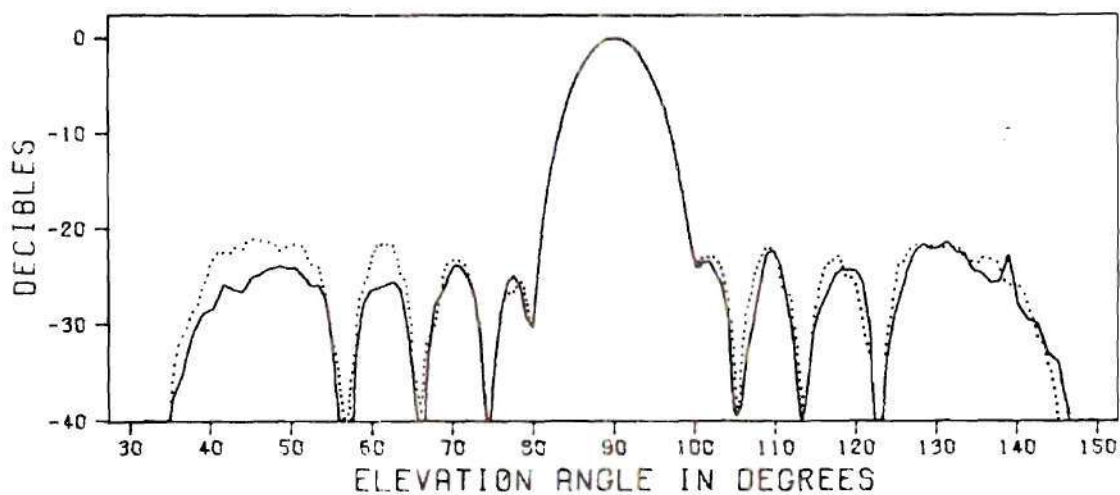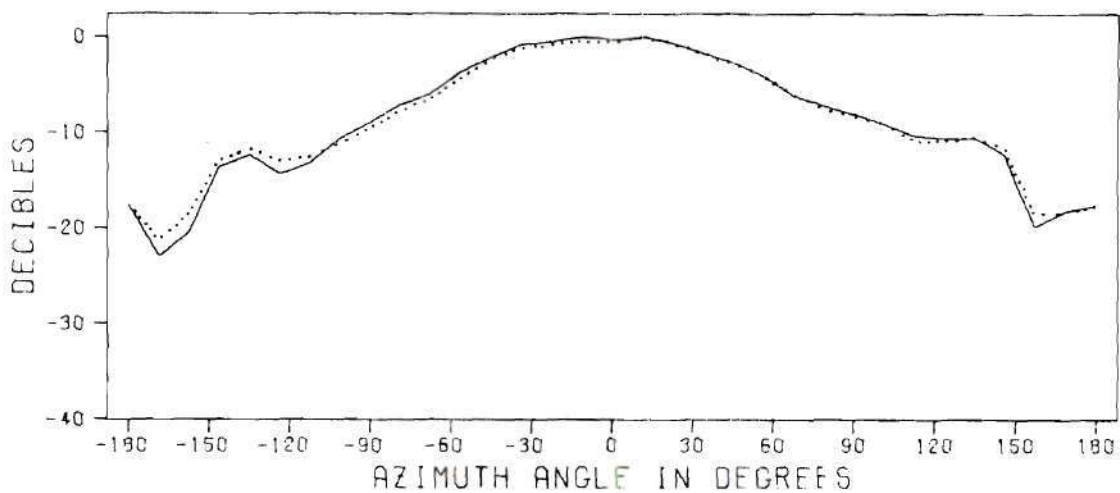
Figure 26. The Calculated Far-Field Amplitude Pattern of $E_\theta$ for Measurement Case Four

(a) Elevation Pattern of $E_\phi$
—— Calculated, •••• Measured



(b) Azimuth Pattern of $E_\phi$
—— Calculated, •••• Measured

Figure 27. Comparison of the Principal Plane Amplitude
Patterns Calculated for Measurement Case
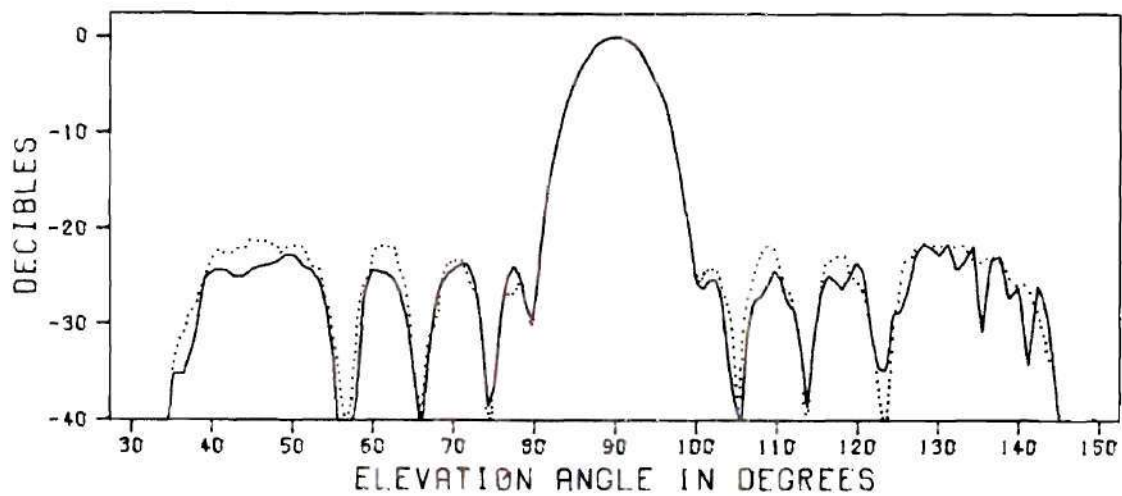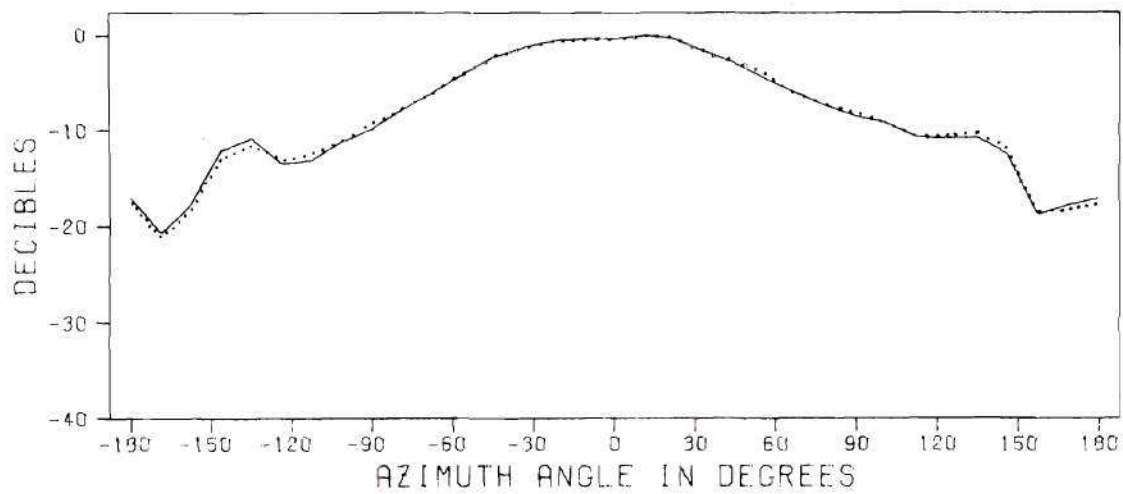One to the Measured Amplitude Patterns

(a) Elevation Pattern of $E_\phi$
——— Calculated, •••• Measured



(b) Azimuth Pattern of $E_\phi$
——— Calculated, •••• Measured

Figure 28. Comparison of the Principal Plane Amplitude
Patterns Calculated for Measurement Case
Two to the Measured Amplitude Patterns

(a)  Elevation Pattern of $E_\phi$
——— Calculated, •••• Measured



(b)  Azimuth Pattern of $E_\phi$
——— Calculated, •••• Measured

Figure 29.  Comparison of the Principal Plane Amplitude
Patterns Calculated for Measurement Case
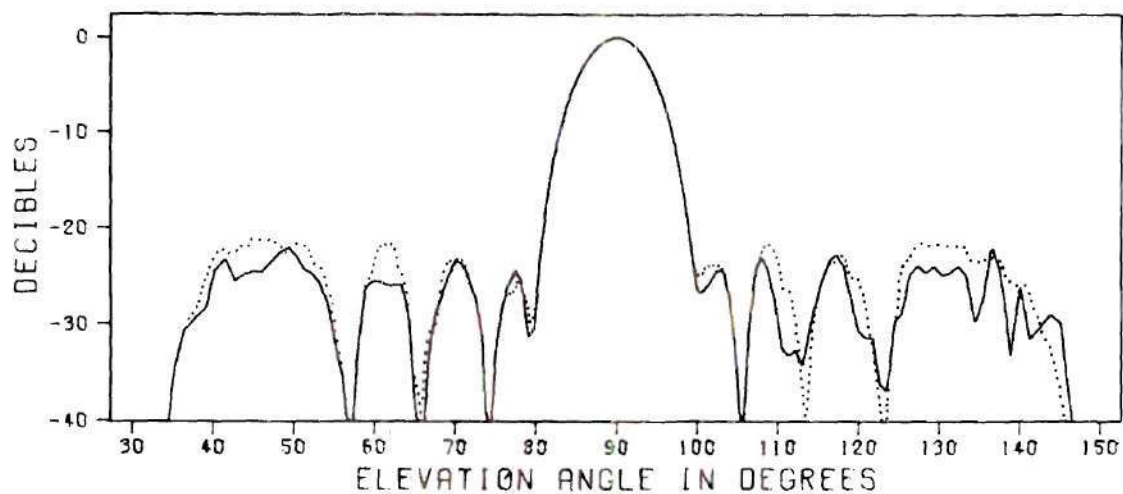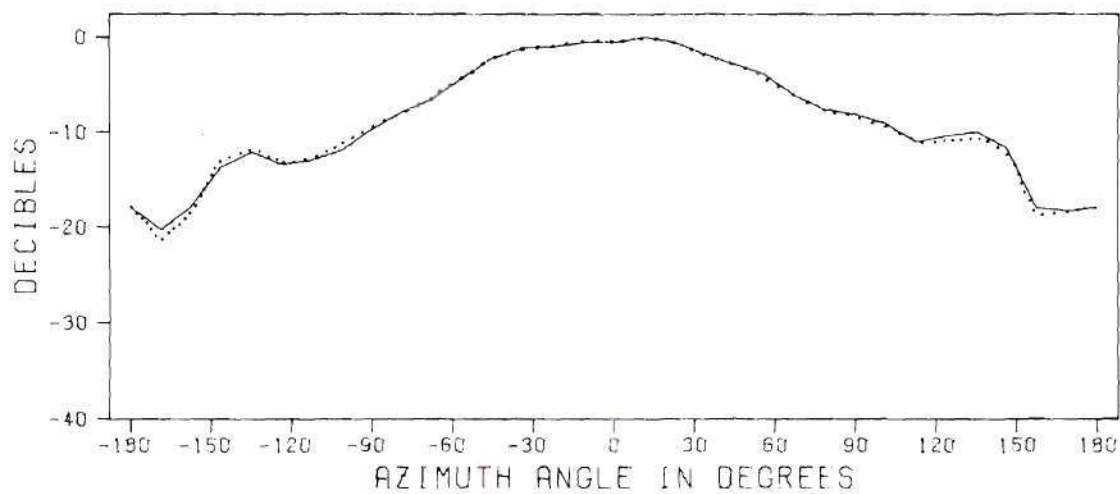Three to the Measured Amplitude Patterns

array.  It is not known if the discrepancies observed in Figures 28(a) and 29(a) could have been caused by smaller "impulse spikes" which could not be differentiated from the data or "drop outs" in the phase channel of the tape deck.  The phase signal was of a level such that a "drop out" in that channel would cause the analog to digital converter to saturate at the +180° output level.  Thus it was impossible to locate any "drop outs" in the phase channel since the phase data were so erratic to begin with.

A comparison of the far-field pattern calculated for measurement case four to the measured far-field pattern reveals outstanding agreement over the range of angles for which the far-field pattern was measured.  The calculated pattern for this case was computed by summing harmonics in the azimuth angle $\phi$ for orders from 0 to 120.

# CHAPTER VI

## CONCLUSIONS AND RECOMMENDATIONS

It is concluded that the method which has been described to obtain the far-field pattern of an antenna from probe compensated near-field measurements on a cylinder is valid. Although the measurement phase of the research was undertaken to experimentally verify the theory, it is felt that it has been demonstrated that the method is practical from both a measurement and computational viewpoint.

It is recommended that the problem of near-field sampling be studied to determine methods of reducing the amount of data which must be measured to calculate accurately the far-field pattern of an antenna. This could include measuring the near field only over selected portions of the measurement cylinder (such as the circle around the antenna in measurement case four), using increased sample spacings, or both. Also, it is recommended that the theory be extended to arbitrary near-field measurement surfaces, particularly those which lend practicality in an experimental implementation. It is felt that the sphere is very attractive in this respect, and that some of the problems which Jensen (6) encountered could be overcome if two independent measurements are made on the sphere.

From a measurement viewpoint, it is not recommended that analog magnetic tape be used as the recording medium for any near-field

measurements. The problems which were encountered with the analog tape were many. These could have been avoided by recording the data in digital format, a form which easily lends itself to automating the data-taking process.

# APPENDIX A

## EVALUATION OF EQUATION (2-40)

Each scalar component of the integral in Equation (2-40) is of the form

$$I = \int_C f(\alpha)e^{Rg(\alpha)} \, d\alpha \qquad (A-1)$$

This integral can be evaluated for large R using the method of steepest descent. This method consists of first finding the point $\alpha_o$ on C at which $g'(\alpha) = 0$. The contour C is then deformed into the path S which passes through $\alpha_o$ and on which $Re[g(\alpha)] \leq Re[g(\alpha_o)]$ and $Im[g(\alpha)] = Im[g(\alpha_o)]$. The point $\alpha_o$ is called the saddle point of the integral and S the steepest descent path. If this path exists, the change in variables

$$g(\alpha) = g(\alpha_o) - w^2 \qquad (A-2)$$

can be made where w is real and $\alpha$ lies on S. Thus the integral can be transformed into

$$I = e^{Rg(\alpha_o)} \int_{-\infty}^{\infty} f(\alpha) \, e^{-Rw^2} \frac{d\alpha}{dw} \, dw \qquad (A-3)$$

where $\alpha$ is a function of w defined implicitly by Equation (A-2).

The method of steepest descent refers to the first term in the asymptotic expansion about $R = \infty$ of the integral in Equation (A-3). This is shown by Clemmow (36) to be

$$I = \pm \sqrt{\frac{-2\pi}{Rg''(\alpha_o)}} \; e^{Rg(\alpha_o)} \; f(\alpha_o) \qquad \text{(A-4)}$$

where the ambiguity in sign must be resolved by examining

$$\left[\frac{d\alpha}{dw}\right]_{\alpha=\alpha_o} = \pm \sqrt{\frac{-2}{g''(\alpha_o)}} \qquad \text{(A-5)}$$

at the saddle point. The sign in Equation (A-5) must be chosen to make $d\alpha$ tangent to S at $\alpha = \alpha_o$. The corresponding sign is then used in Equation (A-4).

The function $g(\alpha)$ in the integral to be evaluated is

$$g(\alpha) = -jk\sin(\alpha+\theta) \qquad \text{(A-6)}$$

The saddle point is found by setting $g'(\alpha_o) = 0$.

$$g'(\alpha_o) = -jk\cos(\alpha_o+\theta) = 0 \qquad \text{(A-7)}$$

The only solution to this equation which lies on C is

$$\alpha_o = \frac{\pi}{2} - \theta \qquad \text{(A-8)}$$

At $\alpha_o$, it follows that $g(\alpha_o) = -jk$.

The region of the complex $\alpha$-plane for which $Re[g(\alpha)] \leq Re[g(\alpha_o)]$ is defined by the equation

$$\cos(\alpha_r+\theta)\sinh \alpha_i \leq 0 \qquad \text{(A-9)}$$

where $\alpha = \alpha_r + j\alpha_i$. This region is the shaded region in Figure 30. The steepest descent path must lie in this region to insure convergence of the integral. On this path $Im[g(\alpha)] = Im[g(\alpha_o)]$. Thus the equation for the path is

$$\sin(\alpha_r+\theta)\cosh \alpha_i = 1 \qquad \text{(A-10)}$$

This path is sketched in Figure 30.

To resolve the sign ambiguity in Equation (A-5), $d\alpha/dw$ must be calculated at the saddle point. At this point $g''(\alpha_o) = jk$. Thus, using Equation (A-5), $d\alpha/dw$ is given by

$$[d\alpha/dw]_{\alpha=\alpha_o} = \pm \sqrt{\frac{-2}{jk}} \qquad \text{(A-11)}$$

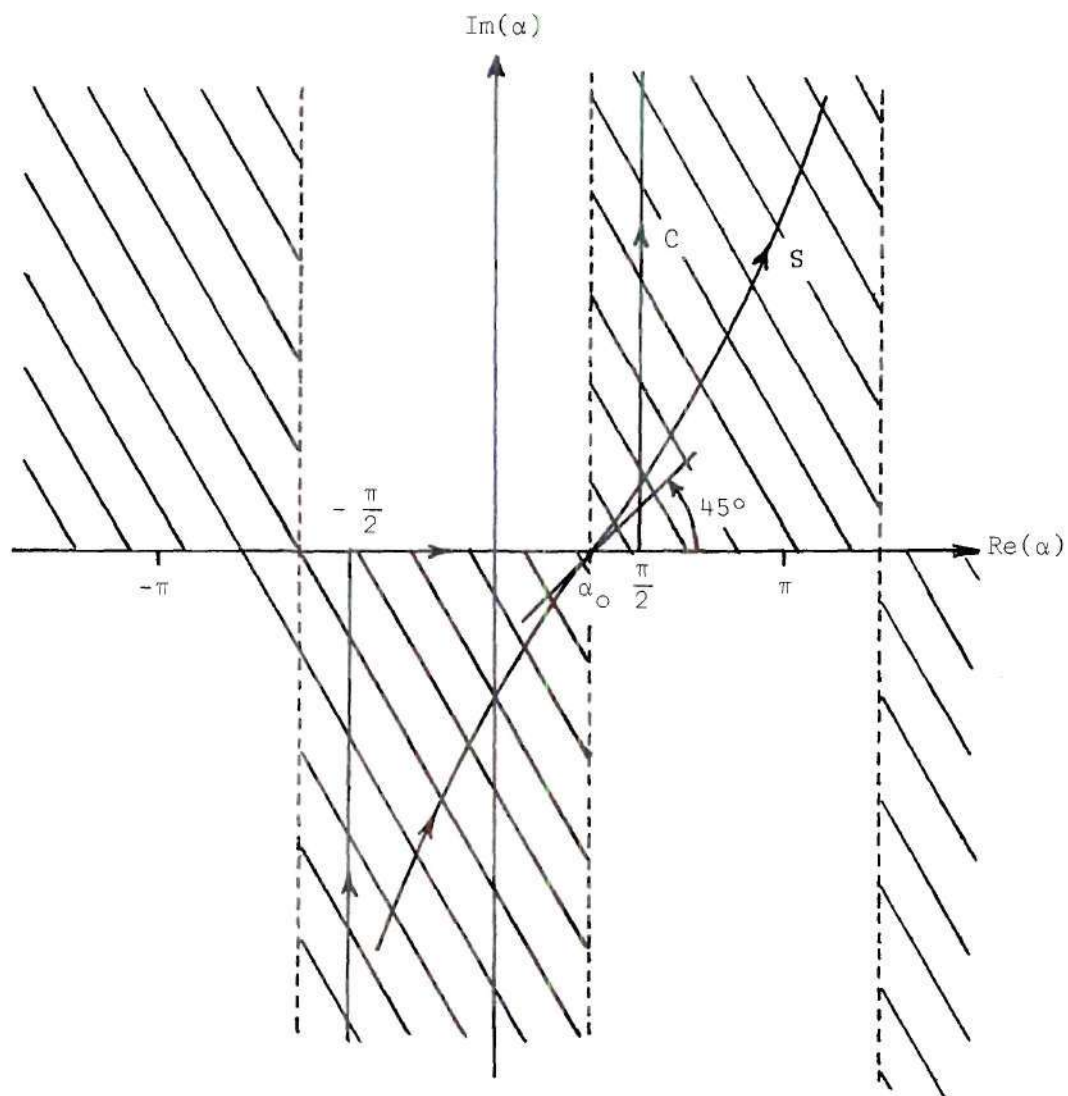$$= \pm (1+j) \sqrt{1/k}$$

Examination of Figure 30 at $\alpha = \alpha_o$ shows that

Figure 30.  The Path of Steepest Descent

$$\frac{d\alpha}{dw} = (1 + j\frac{\partial \alpha_i}{\partial \alpha_r}) \frac{d\alpha_r}{dw} \tag{A-12}$$

$$= (1 + j) \frac{d\alpha_r}{dw}$$

Since a positive increment in w corresponds to moving along S in the positive direction, it follows from Figure 30 that $d\alpha_r/dw > 0$ at every point on S. Therefore, the positive sign in Equation (A-11) must be chosen in order for this equation to agree with Equation (A-12). Thus, for the problem at hand, Equation (A-4) becomes

$$I = + \sqrt{\frac{-2\pi}{g''(\alpha_o)}} \ e^{Rg(\alpha_o)} \ f(\alpha_o) \tag{A-13}$$

With the substitution of the above result into Equation (2-40), the far-field electric field intensity becomes

$$\vec{E} = \frac{-2ks\sin\theta}{R} e^{-jkR} \sum_{n=-\infty}^{\infty} j^n e^{jn\phi}[\hat{\phi}a_n(k\cos\theta) \tag{A-14}$$

$$-j(\hat{r}\cos\theta - \hat{z}\sin\theta)b_n(k\cos\theta)]$$

This is the desired expression.

APPENDIX B

VECTOR TRANSLATION THEOREMS FOR

CYLINDRICAL VECTOR WAVE FUNCTIONS

In the derivation of the response of a probe used to measure the near field of an antenna on a cylinder, it is necessary to be able to translate the reference coordinate of the probe to that of the antenna being tested. The following is a derivation of the necessary theorems.

Let the coordinates $(r_o, \phi_o, z_o)$ be the location of the origin of the coordinate system $(r', \phi', z')$ in the coordinate system $(r, \phi, z)$ as shown in Figure 31. It is desired to express the cylindrical vector wave functions $\vec{M}_{nh}^4(r', \phi', z')$ and $\vec{N}_{nh}^4(r', \phi', z')$ as functions of the coordinates $(r, \phi, z)$. These vectors have been defined previously in Section 2.2.

In the system $(r', \phi', z')$ the generating function $\psi$ is given by

$$\psi(r', \phi', z') = H_n^{(2)}(\Lambda r') e^{jn\phi'} e^{-jhz'} \qquad (B-1)$$

This can be expressed as a function of $(r, \phi, z)$ by using Graf's addition theorem (37) for the Hankel function, which states

$$H_n^{(2)}(\Lambda r') = e^{-jn\phi'} \sum_{m=-\infty}^{\infty} H_{n+m}^{(2)}(\Lambda r_o) J_m(\Lambda r) e^{jm(\phi-\phi_o)} \qquad (B-2)$$

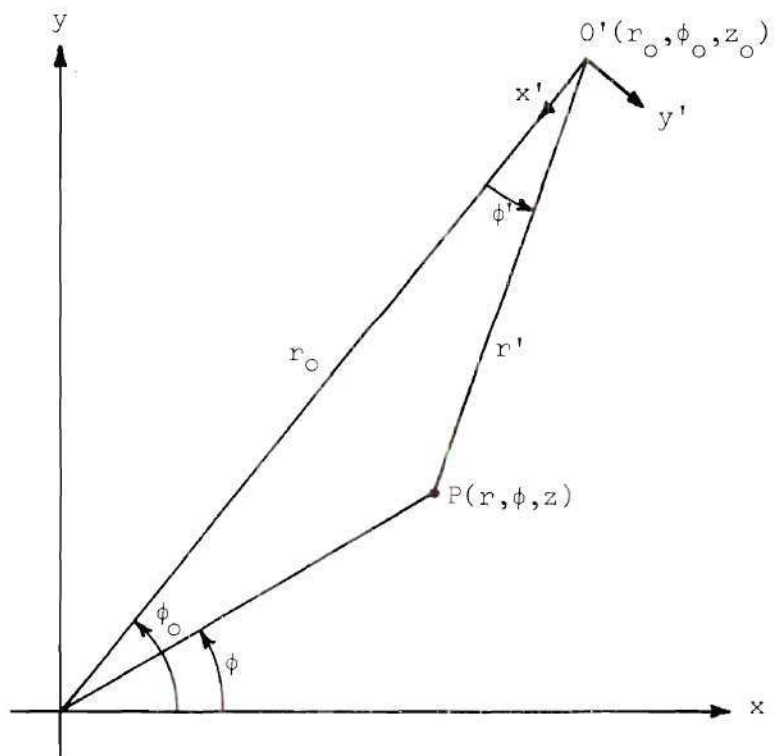When this is substituted into Equation (B-1), the generating function

Figure 31.  Coordinate System for the Cylindrical
Wave Translation Theorems

is transformed into

$$\psi = \sum_{m=-\infty}^{\infty} \left[ H_{n+m}^{(2)}(\Lambda r_o)e^{jm\phi_o} e^{jhz_o} \right] J_m(\Lambda r)e^{-jm\phi} e^{-jhz} \qquad (B\text{-}3)$$

The vectors $\vec{M}_{nh}^4$ and $\vec{N}_{nh}^4$ are obtained by the following operations on $\psi$:

$$\vec{M}_{nh}^4 = \nabla' \times \hat{z}\psi \qquad (B\text{-}4)$$

$$\vec{N}_{nh}^4 = \frac{1}{k_o} \nabla' \times \vec{M}_{nh}^4 \qquad (B\text{-}5)$$

where the primes denote operations on the primed coordinates $(r',\phi',z')$. Since the gradient operation is invariant to a coordinate transformation, these become

$$\vec{M}_{nh}^4 = \sum_{m=-\infty}^{\infty} \left[ H_{n+m}^{(2)}(\Lambda r_o)e^{jm\phi_o} e^{jhz_o} \right] \nabla \times \left[ \hat{z}J_m(\Lambda r)e^{-jm\phi} e^{-jhz} \right] \qquad (B\text{-}6)$$

$$\vec{N}_{nh}^4 = \frac{1}{k_o} \sum_{m=-\infty}^{\infty} \left[ H_{n+m}^{(2)}(\Lambda r_o)e^{jm\phi_o} e^{jhz_o} \right] \nabla \times \nabla \times \left[ \hat{z}J_m(\Lambda r)e^{-jm\phi} e^{-jhz} \right] \qquad (B\text{-}7)$$

With the definitions of $\vec{M}_{nh}^1$ and $\vec{N}_{nh}^1$ from Section 2.2, these expressions reduce to

$$\vec{M}_{nh}^4(r',\phi',z') = \sum_{m=-\infty}^{\infty} (-1)^m H_{n+m}^{(2)}(\Lambda r_o)e^{jm\phi_o} e^{jhz_o} \vec{M}_{-mh}^1(r,\phi,z) \qquad (B\text{-}8)$$

$$\vec{N}_{nh}^4(r',\phi',z') = \sum_{m=-\infty}^{\infty} (-1)^m H_{n+m}^{(2)}(\Lambda r_o) e^{jm\phi_o} e^{jhz_o} \vec{N}_{-mh}^1(r,\phi,z) \qquad (B-9)$$

These are the desired translation theorems. They are valid for all

$r \le r_o$.

APPENDIX C

ORTHOGONALITY PROPERTIES OF THE

CYLINDRICAL WAVE VECTORS

There are four orthogonality properties of the cylindrical wave vectors $\vec{M}$ and $\vec{N}$ over a cylinder of constant radius which are useful in the evaluation of the Lorentz reciprocity integral in Section 2.4. These properties are developed below.

### Property A

$$\int_{-\infty}^{\infty} \int_{-\pi}^{\pi} \vec{M}_{nh}^{i} \times \vec{M}_{m\eta}^{j} \cdot \hat{r} d\phi dz = 0 \qquad \text{for all } m, n, \eta, \text{ and } h \qquad (C-1)$$

This property follows from the fact that the vector $\vec{M}$ contains no z-component. Thus the product $\vec{M}_{nh}^{i} \times \vec{M}_{m\eta}^{j}$ has only a z-component which is zero when scalar-multiplied by the unit vector $\hat{r}$.

### Property B

$$\int_{-\infty}^{\infty} \int_{-\pi}^{\pi} \vec{N}_{nh}^{i} \times \vec{N}_{m\eta}^{j} \cdot \hat{r} d\phi dz = 0 \qquad \text{for all } m, n, \eta \text{ and } h \qquad (C-2)$$

The integrand in Equation (C-2) can be simplified as follows:

$$\vec{N}_{nh}^{i} \times \vec{N}_{m\eta}^{j} \cdot \hat{r} = \vec{N}_{m\eta}^{j} \cdot (\hat{r} \times \vec{N}_{nh}^{i})$$

$$= \left( \frac{nh\lambda^2}{k^2 r} Z_n^i(\Lambda r) Z_m^j(\lambda r) - \frac{mn\Lambda^2}{k^2 r} Z_n^i(\Lambda r) Z_m^j(\lambda r) \right) e^{j(m+n)\phi} e^{-j(\eta+h)z}$$

This is identically zero when integrated with respect to $\phi$ and $z$ unless $m = -n$ and $\eta = -h$. However, under these conditions, the term in brackets is identically zero since $\lambda = \Lambda$ when $\eta = -h$. Thus property B follows immediately.

<center>Property C</center>

$$\int_{-\infty}^{\infty} \int_{-\pi}^{\pi} \vec{N}_{nh}^i \times \vec{M}_{m\eta}^j \cdot \hat{r} d\phi dz = \frac{4\pi^2 \Lambda^3}{k} Z_n^i(\Lambda r) Z_{-n}'^j(\Lambda r)\delta(\eta+h) \quad \text{for } m = -n \quad (C-3)$$

$$= 0 \quad \text{otherwise}$$

The integrand of the above integral can be simplified as follows:

$$\vec{N}_{nh}^i \times \vec{M}_{m\eta}^j \cdot \hat{r} = -\vec{N}_{nh}^i \cdot (\hat{r} \times \vec{M}_{m\eta}^j)$$

$$= \frac{\lambda \Lambda^2}{k} Z_n^i(\Lambda r) Z_m'^j(\lambda r) e^{j(m+n)\phi} e^{j(\eta+h)z}$$

This is zero when integrated with respect to $\phi$ unless $m = -n$. In this case the integral of the exponential term involving $\phi$ is $2\pi$. The integral of the exponential term involving $z$ results in the factor $2\pi\delta(\eta+h)$. Since this is zero for $\eta + h \neq 0$, it follows that the substitution $\eta = -h$ can be made in the rest of the expression. Thus property C follows immediately.

## Property D

$$\int_{-\infty}^{\infty} \int_{-\pi}^{\pi} \vec{M}_{nh}^{i} \times \vec{N}_{m\eta}^{j} \cdot \hat{r} \, d\phi \, dz = - \frac{4\pi^2 \Lambda^3}{k} Z_n^{'i}(\Lambda r) Z_{-n}^{j}(\Lambda r) \delta(\eta+h) \quad \text{for } m = -n \qquad \text{(C-4)}$$

$$= 0 \qquad \text{otherwise}$$

This property follows immediately from property C.

BIBLIOGRAPHY

1. D. M. Kerns, "Antenna measurements with arbitrary antennas at arbitrary distances," *High Frequency and Microwave Field Strength Precision Measurements Seminar*, National Bureau of Standards, Boulder, Colorado, Session 3, Lecture 1, 1966.

2. E. B. Joy and D. T. Paris, "Spatial sampling and filtering in near-field measurements," *IEEE Transactions on Antennas and Propagation*, Vol. AP-20, pp. 253-261, May 1972.

3. M. A. K. Hamid, "The radiation pattern of an antenna from near-zone correlation measurements," *IEEE Transactions on Antennas and Propagation*, Vol. AP-16, pp. 351-353, May 1968.

4. J. Brown and E. V. Jull, "The prediction of aerial radiation patterns from near-field measurements," *Proceedings IEE*, Vol. 108B, pp. 635-644, November 1961.

5. E. V. Jull, "The prediction of aerial radiation patterns from limited near-field measurements," *Proceedings IEE*, Vol. 110, pp. 501-506, March 1963.

6. F. Jensen, "Electromagnetic near-field far-field correlations," *Doctoral Thesis*, The Technical University of Denmark, Lyngby, July 1970.

7. J. R. James and L. W. Longdon, "Prediction of arbitrary electromagnetic fields from measured data," *Alta Frequenza*, Vol. 38, Numero Speciale, pp. 286-290, May 1969.

8. J. J. Gamara, "Pattern predictability on the basis of aperture phase and amplitude distribution measurements," *Tech. Report EDL-M247*, Contract DA 36-039 SC-58402 (DDC No. AD 236298), Electronic Defense Lab., Mountainview, California, March 25, 1960.

9. H. Hu, "Study of near-zone fields of large aperture antennas," *Final Report*, Contract No. AF30(602)-928, Syracuse University Research Institute, April 1957.

10. R. H. T. Bates and J. Elliott, "The determination of the true side-lobe level of long broadside arrays from radiation pattern measurements made in the Fresnal region," *Proceedings IEE*, Vol. 103C, pp. 307-312, March 1956.

11.  R. W. Bickmore, "Fraunhofer pattern measurements in the Fresnel region," *Canadian Journal of Physics,* Vol. 35, pp. 1299-1308, 1957.

12.  S. Silver, *Microwave Antenna Theory and Design,* New York:  McGraw Hill, 1949, pp. 169-199.

13.  P. C. Clemmow, *The Plane Wave Spectrum Representation of Electro-magnetic Fields,* Oxford:  Pergamon Press, 1966.

14.  A. Wood, *Acoustics,* London:  Blackie and Sons, 1950.

15.  D. A. Murphy, "Far-field prediction of submarine radiated noise from near-field measurements," *Final Report 69-11-662,* Contract N00014-69-0-0034, Hughes Aircraft Co., Fullerton, California, June 20, 1969.

16.  A. A. Hudimac and E. M. Fitzgerald, "Near-field measurements using a plane array," *Tech. Note 34,* Hydrospace Research Corp., Rockville, Md., February 5, 1964.

17.  A. C. Ludwig, "Computation of radiation patterns involving numerical double integration," *IEEE Transactions on Antennas and Propagation,* Vol. AP-16, pp. 767-769, November, 1968.

18.  S. A. Brunstein, R. E. Cormack and A. C. Ludwig, "Accuracy of numerically computed electromagnetic scattered problems," *JPL Space Programs Summary 37-52,* Vol. 3, Jet Propulsion Lab., Pasadena, California, pp. 233-238, 1967.

19.  W. V. T. Rusch, "Scattering of a spherical wave by an arbitrary truncated surface of revolution," *JPL Technical Report No. 32-434,* Jet Propulsion Lab., Pasadena, Calif., May 25, 1963.

20.  D. T. Paris, "Digital computer analysis of aperture antennas," *IEEE Transactions on Antennas and Propagation,* Vol. AP-16, pp. 262-264, March, 1968.

21.  J. A. Stratton, *Electromagnetic Theory,* New York:  McGraw-Hill, 1941, pp. 392-395.

22.  Stratton, pp. 355-356.

23.  Stratton, p. 359.

24.  R. E. Collin, *Foundations for Microwave Engineering,* New York: McGraw Hill, 1966, pp. 56-59.

25. R. F. Harrington, "Effect of antenna size on gain, bandwidth, and efficiency," *Journal of Research of the National Bureau of Standards--D. Radio Propagation*, Vol. 64D, pp. 1-12, January-February, 1960.

26. R. E. Collin and S. Rothschild, "Evaluation of antenna Q," *IEEE Transactions on Antennas and Propagation*, Vol. AP-12, pp. 23-27, January, 1964.

27. L. J. Chu, "Physical limitations of omni-directional antennas," *Journal of Applied Physics*, Vol. 19, pp. 1163-1175, December, 1948.

28. A. C. Ludwig, "Near-field far-field transformations using spherical-wave expansions," *IEEE Transactions on Antennas and Propagation*, Vol. AP-19, pp. 214-220, March 1971.

29. R. E. Collin and F. J. Zucker, *Antenna Theory Part I*, New York: McGraw-Hill, 1969, p. 578.

30. W. T. Cochran, et al., "What is the Fast Fourier Transform?," *Proceedings IEEE*, Vol. 55, pp. 1664-1667, October 1967.

31. M. Goldstein and R. M. Thaler, "Bessel functions of large arguments," *Mathematical Tables and Computations*, 1958.

32. M. Goldstein and R. M. Thaler, "Recurrence techniques for the calculation of Bessel functions," *Mathematical Tables and Computations*, 1959.

33. L. L. Bailin, "The radiation field produced by a slot in a large circular cylinder," *IRE Transactions on Antennas and Propagation*, Vol. AP-3, pp. 128-137, July 1955.

34. Collin and Zucker, pp. 588-590.

35. H. Jasik, *Antenna Engineering Handbook*, New York: McGraw-Hill, 1961, pp. 9-5 - 9-8.

36. Clemmow, p. 49.

37. M. Abramowitz and I. A. Stegun, *Handbook of Mathematical Functions*, New York: Dover Publications, 1965, p. 363.

VITA

William Marshall Leach, Jr. was born in Abbeville, South Carolina, on February 23, 1940. He is the son of William Marshall Leach and Sara Harkness Leach.

He attended elementary and secondary schools in Abbeville, South Carolina, and graduated from Abbeville High School in June, 1958. In September, 1959, he entered the University of South Carolina and in June, 1962, he was awarded the Bachelor of Science, Magna Cum Laude, in Electrical Engineering. He was commissioned a Second Lieutenant in the United States Air Force at graduation.

In September, 1962, he entered the Graduate School at the University of South Carolina and received the Master of Science degree in June, 1964. While at the University of South Carolina, he was elected to membership in Phi Beta Kappa, Omicron Delta Kappa, Tau Beta Pi, Eta Kappa Nu, and was listed in *Who's Who in American Colleges and Universities, 1963-64*.

From June to December of 1964 he worked as a Communication Research Engineer at the NASA Hampton Research Center in Hampton, Virginia. He entered active duty in the United States Air Force in January, 1965. He served three years as an Electronics Research and Development Officer with the 1155th Technical Operations Squadron at McClellan AFB, California.

In January, 1968, he entered the Graduate Division of the Georgia Institute of Technology. He held a Schlumberger Fellowship from September, 1968, to June, 1969, and a Lockheed Research Grant from September, 1969, to September, 1970. He has served as a graduate teaching assistant in Electrical Engineering from January, 1968, to September, 1968, and from June, 1969, to September, 1972. He has worked as a graduate research intern at the Systems and Techniques Department of the Georgia Tech Engineering Experiment Station from March, 1971, to September, 1972.